Photophysics of Cadmium Selenide Quantum Dot Solids

by

Catherine A. Leatherdale

B. Sc. Physics/Chemistry
University of British Columbia, Vancouver, 1995

Submitted to the Department of Chemistry
in partial fulfillment of the requirements for
the Degree of

DOCTOR OF PHILOSOPHY

at the

MASSACHUSETTS INSTITUTE OF TECHNOLOGY

September 2000

Signature of Author _____
Department of Chemistry
August 7, 2000

Certified by _____
Moungi G. Bawendi
Professor of Chemistry
Thesis Supervisor

Accepted by _____
Robert W. Field
Chairman, Departmental Committee on Graduate Students

This doctoral thesis has been examined by a committee of the Department of Chemistry as follows:

Professor Robert Silbey _____ Chairman

Professor Moungi Bawendi _____ Thesis Supervisor

Professor Marc Kastner _____

Photophysics of Cadmium Selenide Quantum Dot Solids

by

Catherine A. Leatherdale

Submitted to the Department of Chemistry on August 7, 2000 in partial fulfillment of the requirements for the degree of Doctor of Philosophy in Chemistry

ABSTRACT

Semiconductor quantum dots or nanocrystals have size dependent optical and electronic properties that arise from quantum confinement. While the quantum size effect is reasonably well understood, the effect of abrupt interface between the nanocrystal and its dielectric environment is not. In this thesis we study how the dielectric environment affects the quantum dot electronic structure, the optical absorption cross-section, charge separation, and transport in cadmium selenide colloidal quantum dots. The electronic states and optical absorption cross-section are found to be less sensitive to changes in the dielectric environment than predicted from theory unless screening from the ligand shell is taken into account. The absolute absorption cross-section is measured as a function of quantum dot size; excellent agreement with theory is obtained for absorption far above the band edge.

Three-dimensional close packed solids of quantum dots are predicted to act as model artificial solids. Optical absorption measurements indicate that the electronic states of CdSe quantum dots separated by 11 angstroms or more are essentially uncoupled. Photoconductivity measurements suggest that photoexcited quantum confined excitons are ionized by the applied field with a rate that depends on both the size and surface passivation of the quantum dots. The charge generation efficiency decreases with increasing temperature as non-radiative and radiative recombination pathways increasingly compete with charge separation. A simple tunneling model for the initial charge separation step is presented that qualitatively reproduces both the size and surface dependence of the photoconductivity as a function of applied electric field. Finally, we report observations of amplified spontaneous emission from quantum dot solids. The stimulated emission is tunable with quantum dot size and does not sensitively depend upon surface passivation. These measurements demonstrate the feasibility of nanocrystal quantum dot lasers and amplifiers.

Thesis supervisor: Moungi G. Bawendi, Ph.D.
Professor of Chemistry

For my family

Table of Contents

List of Figures

Chapter 1

Introduction

1.1 Two kinds of confinement

At the heart of materials science is the desire to understand and control structure-property relations in order to prepare scientifically and technologically interesting materials. In the past, properties of solid-state materials were primarily controlled by chemical composition and crystal structure. Recently, dimensionality and physical size were discovered to be powerful knobs by which to tune the electronic, optical, and magnetic properties of materials. Every physical property has a characteristic length scale associated with it and when the physical dimensions of the material are reduced to that scale, the property becomes size dependent. Figure 1.1 summarizes some of the important length scales for phenomena described in this thesis.

In bulk semiconductors and metals, the allowed energy and momentum states of an electron* moving through the solid are determined by the periodic potential of the lattice. However, when the electron is restricted in one or more dimensions to a region comparable to its de Broglie wavelength, it experiences quantum confinement. The energy of the electron must be described using quantum mechanics and only certain quantized energy and momentum states that satisfy the boundary conditions are permitted. For quantum wells and quantum wires, the electron motion is restricted in one and two directions respectively. In quantum dots (QDs), the electron experiences

* The same discussion may be applied to a hole in the valence band of a semiconductor.

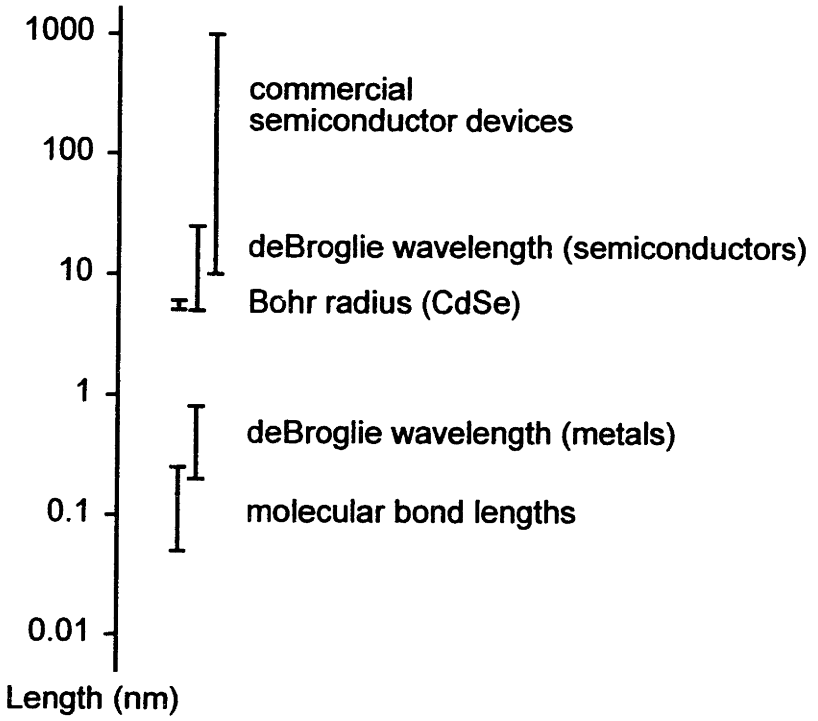

Figure 1.1 Illustration of important physical length scales for metals and semiconductors. For commercial semiconductor devices, the lower end of the scale bar indicates the thickness of the gate oxide in a MOS transistor

complete three-dimensional quantum confinement such that it can only exist in discrete, atomic-like electronic states. This phenomenon has earned QDs the nickname "artificial atoms" [1] and it has a profound effect on the optical and electrical properties.

Quantum confinement has been studied extensively and quantum wells are already used in commercial devices including the laser in your CD player. The implications of classical dielectric confinement at the same length scale, however, are much less well understood. Dielectric confinement arises when there is a change in dielectric constant between the region of interest and the surrounding medium. In the presence of an electric field, be it externally applied, from a point charge, or from an electromagnetic wave, both materials polarize and bound charge appears at the interface. Polarization and the bound image charge can affect everything from the energy required to charge the region, to how it interacts with the electric field of light.

In this thesis, I study the inter-play between quantum and dielectric confinement for semiconductor QDs as they interact with light, externally applied electric fields, charges, and each other. Periodic arrays of QDs offer the opportunity to build a periodic potential from the ground up and with it a new tunable material based on the electronic structure of our "artificial atoms". The optical and electrical properties of semiconductor QD solids are studied to evaluate the potential of such a system.

The phenomena I have described are not only interesting from a pure science perspective but are also clearly technologically relevant given the ever shrinking dimensions of transistors and integrated circuits. The range of typical dimensions found

in commercial semiconductor devices is indicated in Figure 1.1. The quantum world and the commercial world will soon overlap, like it or not.

1.1.1 Quantum confinement

1.1.1.1 Particle in the sphere

The QDs we study are spherical and in the calculations throughout this thesis we use the particle-in-the-sphere wave functions as our basis. It is helpful to know where these wave functions come from. Consider particle of mass m in a spherically symmetric potential of radius a where,

$$V(r)=0 \qquad r<a \qquad (1.1a)$$

$$V(r)=\infty \qquad r>a \qquad (1.1\,b)$$

Solving the Schrödinger equation, $H\Psi = E\Psi$, with $H=\frac{-\hbar^2}{2m}\nabla^2$, in spherical coordinates one obtains solutions of the form,

$$\Psi_{n,l,m}(r,\theta,\phi)=j_l(k_{n,l},r)Y_{l\,m}(\theta,\phi) \qquad (1.2)$$

where $j_l(k_{n,l},r)$ is the lth order spherical Bessel function, $k_{n,l}$ is equal to $\alpha_{n,l}/a$ where $\alpha_{n,l}$ is the nth zero of j_l, and $Y_{l,m}(\theta,\phi)$ are the spherical harmonics. The energies of a carrier confined to this region are given by,

$$E=\frac{\hbar^2\alpha_{n,l}^2}{2ma^2} \qquad (1.3)$$

Equation (1.3) shows that the energy of the carrier increases with decreasing particle size. The lowest energy wave function is given by,

$$\Psi_{1,0,0}=\frac{1}{\sqrt{4\pi}}\frac{1}{r}\sin\left(\frac{\pi r}{a}\right) \qquad (1.4)$$

Because of its spherical symmetry, the lowest energy wave function is given the designation 1S. Higher angular momentum states have P and D like symmetry respectively, reinforcing the idea that spherical QDs act like artificial atoms.

In reality of course, the potential inside the well is not zero and a carrier confined in the QD feels the periodic potential of the underlying lattice. From Bloch's theorem a carrier with wavevector k, moving in a periodic potential $u_k(r)$ has wavefunction,

$$\Psi(r) = u_k(r)e^{ik\,r} \tag{1.5}$$

Within the effective mass approximation, the spherical "envelope" functions described before replace the plane wave envelope functions of (1.5) and the mass of the carrier is replaced by the effective mass of an electron or hole moving in the conduction or valence band. For example, the total wavefunction for an electron in the conduction band is given by,

$$\Psi_e(r,\theta,\phi) = u_c(r)j_l(k_{n,l},r)Y_{l\,m}(\theta,\phi) \tag{1.6}$$

where $u_c(r)$ is the unit cell function. The optical band gap becomes,

$$E = E_g + \frac{\hbar^2 \alpha_{n,l}^{\;2}}{2m_e a^2} + \frac{\hbar^2 \alpha_{n,l}^{\;2}}{2m_h a^2} \tag{1.7}$$

While almost naively simple, equation (1.7) encapsulates some of the most well known manifestations of the quantum size effect in semiconductors; the electronic states become discrete and the band gap increases with decreasing QD radius. It also shows that the quantum size effect is material dependent.

1.1.1.2 Perturbations

When a QD interacts with a photon that has energy greater than the band gap, an electron-hole pair or exciton is created. In this two-body problem it is necessary to

account for the Coulomb interaction in order to describe the "optical" band gap correctly. In the strong confinement regime where the radius of the QD is much less than the bulk Bohr exciton radius, the kinetic energy gained from quantum confinement is greater than the electron-hole Coulomb interaction. It is at this length scale where the quantum size effect becomes obvious in optical measurements. As a first approximation, the energy associated with the Coulomb interaction may be calculated using the spherical envelope wavefunctions as the basis and applying perturbation theory. This approach will also be used to model the effect of image charge.

There are many properties of semiconductor QDs that cannot be modeled using such a simplistic approach and it is necessary to take into account the full band structure of the semiconductor. In particular the luminescence properties of CdSe QDs depend strongly on degeneracies in the valence band and the electron-hole exchange interaction. We will not discuss these effects here but instead refer the interested reader to the following excellent references.[2,3]

For analysis of charge transport properties, the most important flaw in the preceding discussion is that with an infinite potential barrier, carriers cannot leave the QD! Applying a piecewise linear potential in the radial direction and including a finite potential barrier, the envelope wavefunctions exponentially decay outside the QD. For the nanocrystals we study, the height of the potential barrier and the leakage of the wavefunction outside of the particle are not well known parameters.* We will return to this problem in Chapter 4.

* Though it is safe to say that the leakage is small.

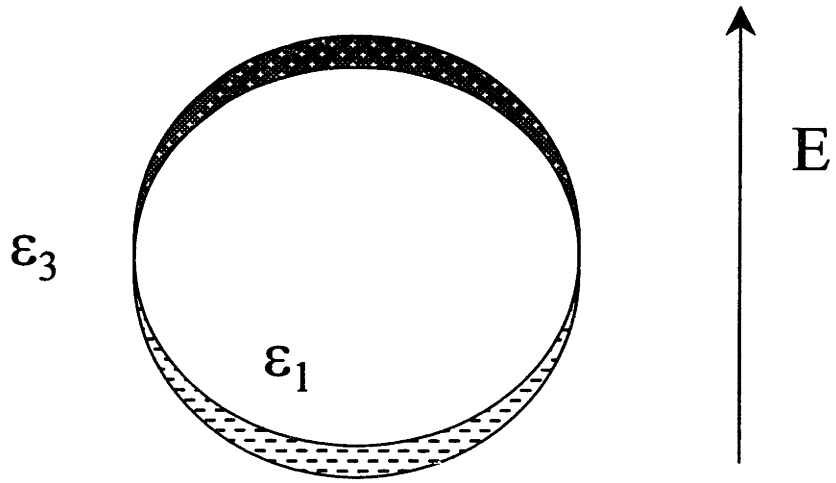

A: Polarization in a uniform electric field

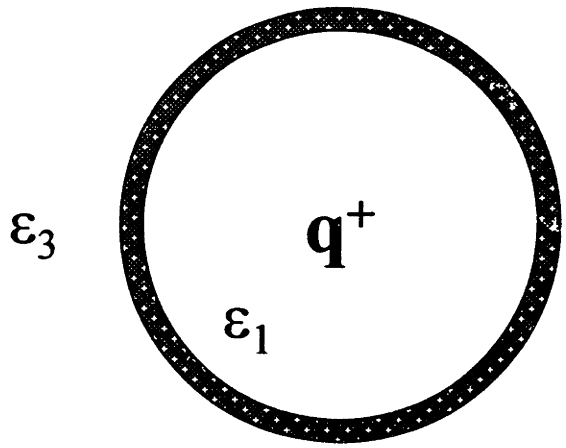

B: Polarization from a point charge

Figure 1.2 Cartoon of the bound charge on a dielectric sphere in (A) the presence of an external applied electric field and (B) with an internal point charge. In this case, if $\varepsilon_3 < \varepsilon_1$ then the sign of the bound charge is positive. The reverse is true if $\varepsilon_3 > \varepsilon_1$.

1.1.2 Dielectric confinement

In this section we address the implications of small particle size from the point of view of classical electrostatics. Treating the material as a continuum, Maxwell's equations for electric fields in matter in CGS units may be stated as, [4]

$$\nabla \times \vec{E} = 0$$
$$\nabla \cdot \vec{D} = 4\pi\rho_f \tag{1.8}$$

where E is the electric field, D is the electric displacement and ρ_f is the free charge density. D is proportional to the electric field plus the polarization (P) of the material.

$$\vec{D} = \vec{E} + 4\pi\vec{P} = (1 + 4\pi\chi)\vec{E} = \varepsilon\vec{E} \tag{1.9}$$

The normal components of D are continuous across a boundary between media with different dielectric constants (ε) unless *free* surface charge (σ) is present. In this case difference between the normal components is equal to the surface charge.

$$(D_N)_2 - (D_N)_1 = 4\pi\sigma \tag{1.10}$$

1.1.2.1 Implications for QDs

In the presence of an external electric field (either externally applied or from charges inside the QD), there will be a bound surface polarization charge at the interface between the QD and the medium (Figure 1.2). The Coulomb interaction between the surface polarization charge and carriers confined to the QDs affects the energy of the carriers and how much energy is required to add or remove a carrier from the QD. Two cases that were first described by Brus[5,6] are especially relevant to the discussion in this thesis:

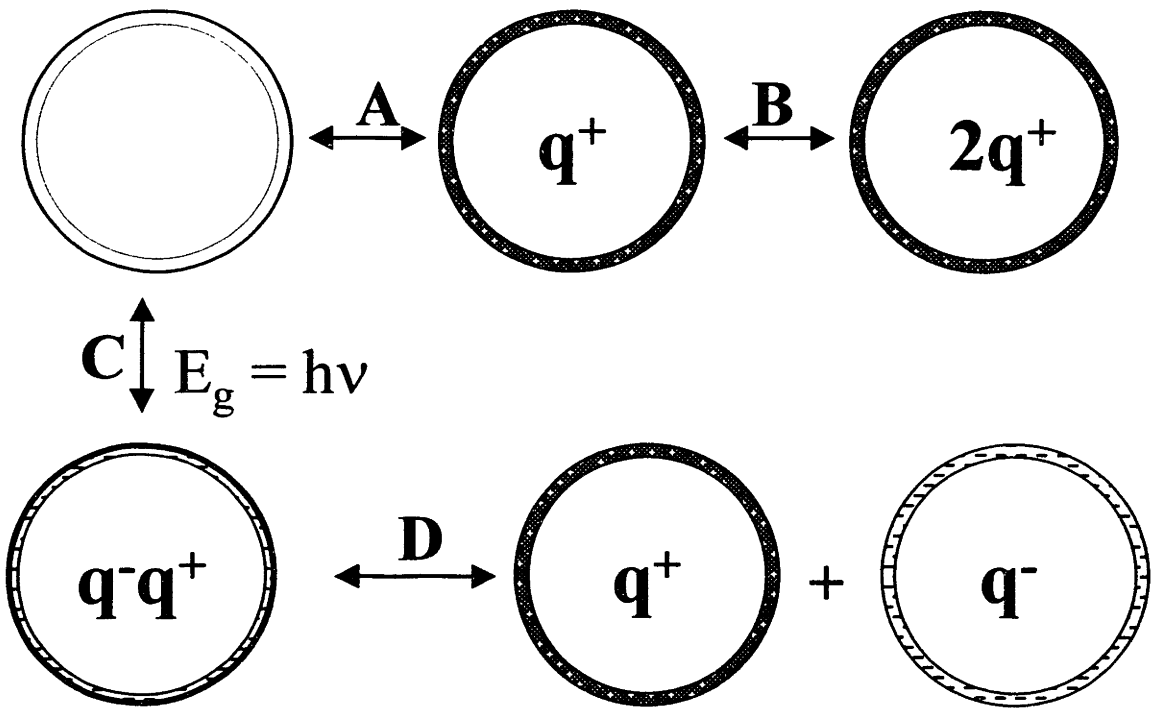

Figure 1.3 Cartoon of each of the processes affected by the bound image charge for a small dielectric sphere. Process **A** illustrates the self-charging energy, **B** illustrates the Coulomb charging energy, **C** illustrates absorption of photon to create an excited electron-hole pair, and **D** indicates ionization of the electron-hole pair to create two charged QDs. In all four processes, the sign of the bound charge is indicated for the case where the external dielectric constant less than the internal dielectric constant.

(1) The self-charging energy

(2) The polarization energy

The self-charging energy is the energy required to add a single electron or hole to a neutral QD (Fig 1.3-A). The polarization energy arises when there are two oppositely charged carriers in the QD and comes from Coulomb interaction of one charge with the image charge of the other carrier.* While the QD is formally charge neutral and it would appear that there is no net electric field, fluctuations in the positions of the two carriers lead to a fluctuating electric field and a net energy cost.[6]

In addition to the interaction with the image charge, changing the number of charges on the QD also costs energy. The Coulomb charging energy is defined as the energy difference between E_{N+1} and E_N charges (of the same sign) in the QD (Figure 1.3-B). It incorporates both the direct Coulomb interactions between the carriers confined to the QD and the electrostatic interaction of these carriers with the bound surface charge. When the Coulomb charging energy is greater than the available thermal energy (k_BT), the number of electrons on the QD will stay constant until sufficient electric field is applied that another one can be added. This is the origin of single electron tunneling effects.[1,7,8] For CdSe QDs with radius less than 5 nm, the Coulomb charging energy is greater than 100 meV. Ionization of an excited semiconductor QD requires overcoming the exciton binding energy that includes both the direct electron-hole Coulomb interaction and the polarization energy. In Chapter 4 we show energy required to ionize a photoexcited electron-hole pair is also much greater than k_BT at room temperature.

Several recent publications [9,10] have pointed out that in principle it is possible to physically separate the effects of dielectric and quantum confinement. In quantum confinement, the wavefunction decays exponentially into the potential barrier where as in dielectric confinement the Coulomb potential decays more slowly (proportional to 1/r). Thus the dielectric boundary can be quite far away from the QD but still influence its properties. An interesting example to think about is a semiconductor QD surrounded by a shell of another higher band gap semiconductor, which is then embedded in some organic medium. The main dielectric boundary is physically moved away from where the core wavefunctions are concentrated reducing the interaction with the image charge.

1.2 How to make quantum dots

QDs may be synthesized by both "top-down" and "bottom-up" approaches.† From the physics community, elegant low temperature experiments have been performed on one or two dot systems prepared using a transistor-like structure with electron-beam lithography defined gate electrodes to control the height of the potential barriers around the QD.[1,11] Although the experiments are very well controlled, scaling up to an array of just 100 QDs, is prohibitively difficult. Large arrays of QDs with lateral dimensions as small as ~ 10 nm can be produced by the Stranski-Krastanow growth mechanism.[12,13] Molecular beam epitaxy of a semiconductor on a substrate with a high degree of lattice mismatch results in a highly strained layer that collapses to form pyramid-like islands. By tuning both the lattice mismatch and the growth conditions, pyramids of different

---

* For an excellent discussion of the effect of the surface polarization charge, the interested reader is directed to the recent publication by Franceshetti and Zunger.[9]

† Unfortunately, the method chosen to synthesize the QDs often divides the subsequent literature as well, to the detriment of both scientific communities.

sizes and aspect ratios can be produced. Small nanocrystals may also be formed through controlled annealing of semiconductor doped glasses[14] and sol-gel processes.[15]

Wet chemical approaches to QD synthesis have the advantage that it is possible to produce macroscopic quantities with good control over QD size and shape. In addition, further surface chemistry on the nanocrystals following the synthesis allows the QDs to be put into a variety of different environments and more complex structures to be built up from individual QDs. The organometallic synthesis described below has proven to be quite general; nanocrystals of nearly all the group II-VI, and III-V semiconductors as well as some metals may be prepared with only minor variations.

1.2.1 The Murray et al. synthesis

In the methodology developed by Murray *et al.*[16], the organometallic precursers, dimethyl cadmium and tri-octylphosphine selenide, are dissolved in tri-octylphosphine (TOP) and rapidly injected into hot tri-octylphosphine oxide (TOPO) at 350 °C and under inert atmosphere. Small CdSe nanocrystals approximately 1 nm radius nucleate immediately and may be isolated by cooling the reaction flask. Larger nanocrystals may be grown through continued heating at ~ 290 °C. The TOPO/TOP surface ligands moderate the growth rate of the QDs, electronically passivate the surface of the QD, and sterically stabilize the QDs in solution, preventing irreversible aggregation. QDs with 1-5 nm radius and typical size distribution ~ 10% may be routinely produced using this synthetic method. The size distribution may be further narrowed to atomic layer precision using size selective precipitation.

Figure 1.4 shows a cartoon, a transmission electron micrograph (TEM) image, and a series of absorption spectra of the nanocrystals we study. The effects of quantum

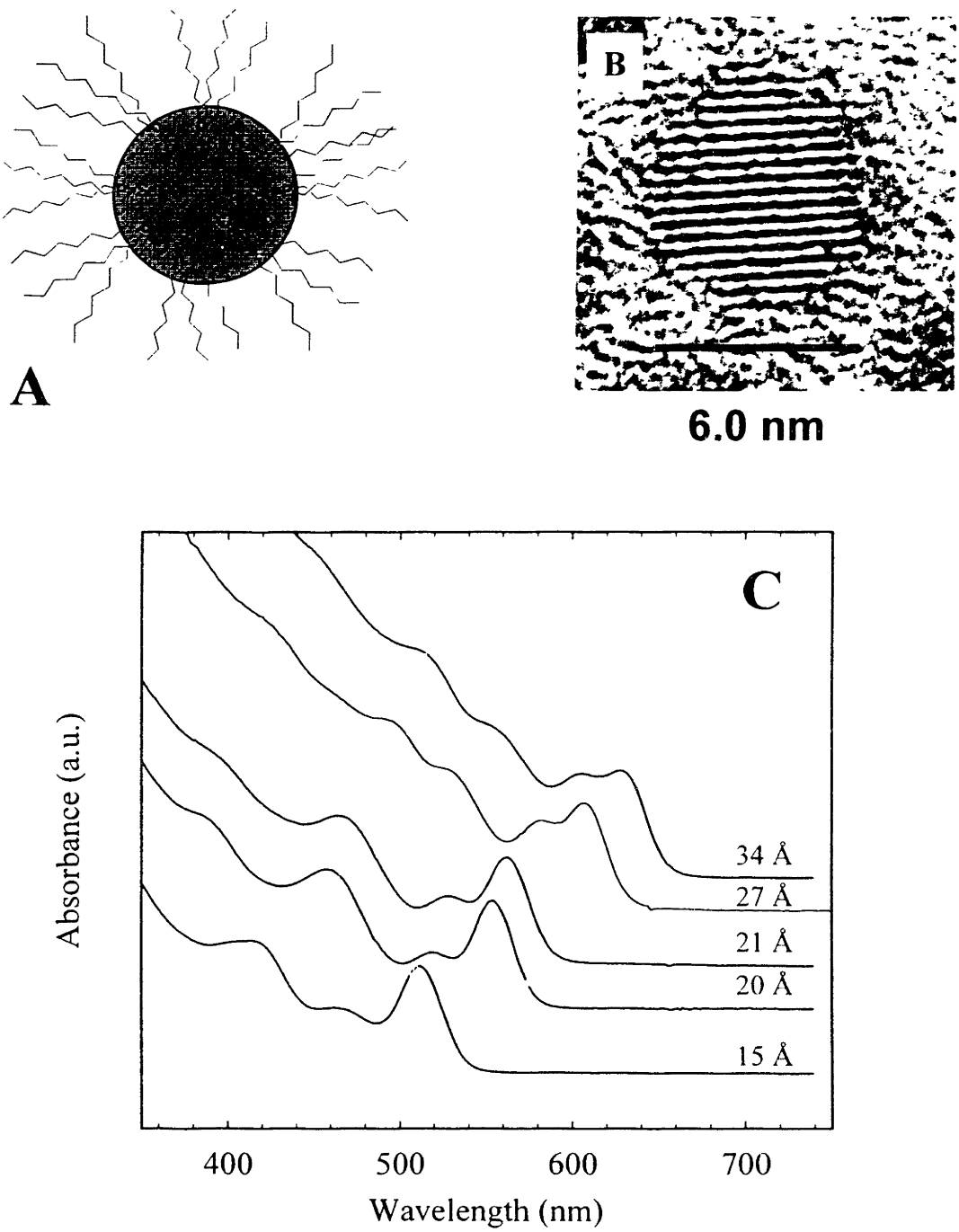

Figure 1.4 **(A)** Cartoon of a semiconductor nanocrystal QD with TOPO and TOP ligands coordinated to the surface. **(B)** High resolution TEM image of a CdTe QD. The alternating light and dark lines are the atomic lattice planes (microscopy by F.V. Mikulec) **(C)** Size series of CdSe QDs showing the room temperature solution absorption spectra with radii as indicated.

confinement and the narrow size distribution are evident in the shift of the band edge to higher energies with decreasing QD radius and the discrete electronic transitions. Strong band edge photoluminescence (PL) is observed from these nanocrystals even with only the organic TOPO/TOP capping ligands. The luminescence properties may be further enhanced by overcoating with a shell of a second, higher band gap semiconductor.[17,18]

1.2.2 Why colloidal QDs are different than epitaxially grown QDs

The dielectric discontinuity represents a fundamental difference between colloidal QDs or nanocrystals and QDs embedded in semiconductors. For example, InAs QDs can be prepared either by the Stranski-Krastanow mechanism[12] or using organometallic synthesis.[19] As a result of the large dielectric contrast, the Coulomb charging energy of a spherical 21 Å radius InAs QD (ε_s = 14.6) is almost an order of magnitude larger in a typical organic solvent or polymer (ε_s~ 2) versus the same nanocrystal embedded in GaAs (ε_s = 13.2).[9] This difference should dramatically change the room temperature electrical properties.

In addition to changing the energy of the electronic states, the sharp potential boundary and the presence of image charge affects the rate of carrier relaxation processes thereby changing the QD optical properties. Auger-like scattering processes mediated by the electron-hole Coulomb interaction are much more efficient for semiconductor nanostructures than in bulk crystalline material.[20,21] The Auger rates are increased both by the presence of the heteroboundary and the enhanced Coulomb interaction. Thus despite the widely separated electronic states that are many optical phonon energies apart, single excitons in nanocrystal QDs rapidly relax to the lowest excited state through energy transfer from the electron to the hole.[22,23] The same enhanced Coulomb

interaction also leads to rapid non-radiative recombination of multiple electron-hole pairs.[24] These processes put a fundamental limitation on the gain that can be achieved from the nanocrystal QD laser (see Chapter 6).[25] Auger ionization is also more likely,[26] possibly explaining why fluorescence intermittency is observed for single nanocrystal QDs[27] but only rarely for QDs embedded in other semiconductors.

1.3 The Art and Science of Quantum Dot Solids

More than 30 years ago, it was suggested that one could build an artificial superlattice to study the basic principles of solid state physics.[28] By tuning the density of states of the artificial atoms and the coupling between them, one could rationally design the periodic potential and thus the band structure of the artificial solid. From a tight-binding perspective, the degree of coupling is controlled by the overlap integral of single particle wavefunctions on adjacent sites in the lattice:

$$\gamma = \langle \Psi_i(r) | U(r) | \Psi_j(r+R) \rangle \qquad (1.11)$$

Thus, the coupling and bandwidth (γ) depends on the distance between the sites and the shape of the intervening potential. Colloidal QDs are excellent candidates for such a structure as they readily self assemble into close-packed arrays (see below) and the surface ligands can be easily exchanged to tune the distance between the particles and in principle, the electronic couplings.

1.3.1 Transport in metallic vs. semiconductor nanoparticle arrays

Transport in 2-D arrays of metallic dots has already been the subject of a number of experimental [29-32] and theoretical investigations.[33] In DC conductivity, reducing the length of the ligand chains increased the conductance of arrays of gold nanocrystals.[30]

Increased conductance was also observed when the native alkanethiol capping groups were replaced with molecular wire-like linker molecules.[31] In the Coulomb blockade regime, threshold type DC conductivity is predicted[33] but to our knowledge has only been observed in metal arrays prepared by electron beam lithography.[34] The most significant result to date has been the demonstration of a reversible metal-Mott insulator transition as a monolayer of Ag nanocrystals was compressed on a Langmuir trough. [35] The metal-insulator transition was indicated both by a change in the optical properties and in AC conductivity. It is important to note that metal nanocrystals are generally too large to exhibit quantum confinement; the discrete density of states arises instead from Coulomb charging states.

The behavior of semiconductor QDs arrays is expected to be significantly different from the metallic arrays. The spacing of the electronic states in the conduction band exceeds k_BT and is comparable to the Coulomb charging energy. Since the lowest energy electron and hole wavefunctions are concentrated in the center of the QD, semiconductor QDs need to be nearly in direct contact to have strong quantum mechanical coupling. In addition to these quantum mechanical effects, Coulomb interactions between charges in the semiconductor QD array are much stronger. The Coulomb interaction between charges on adjacent QDs is comparable to the Coulomb charging energy of a single QD. As a result, long range interactions between charges in the array are important. Finally, for intrinsic wide band gap semiconductors such as CdSe, the electron density in the conduction band is negligible at low temperatures. Mobile charge must be injected by doping, injection from the contacts, or in the case of this thesis, photogenerated using light.

1.3.2 The effects of disorder

Seldom mentioned in any of the metallic or semiconductor array studies to date are the effects of disorder.[32,36] Since the site charging energy and the electronic structure of the QD depend sensitively on the radius, the energy "bandwidth" associated with the intrinsic size distribution of the QDs must be less than available thermal energy in order to avoid creating traps in the QD solid. Thus, high quality samples are required. Small QDs are more sensitive to disorder than large QDs. Semiconductor QDs are also more sensitive to the size distribution than the metals since the quantum confined electronic states are proportional to $1/a^2$; the charge states of metal nanocrystals are proportional $1/a$. Even if the size distribution could be eliminated, varying degrees of ligand inter-penetration mean that some positional disorder will remain. Only when the QDs are strongly coupled does the lattice symmetry and domain size become important.

1.3.3 Preparation of QD solids

Nanometer size hard spheres with low polydispersity readily self-assemble into close-packed arrays. Experimental studies[37-39] and Monte Carlo simulations[40] suggest that crystallization of nanometer size spheres is driven by primarily inter-particle and particle-substrate van der Waals interactions. The van der Waals interactions can be tuned by changing the surface passivation, ligand chain length, substrate surface energy, and solvent polarity to optimize formation of the equilibrium structure.

The majority of the QD solids studied in this thesis are prepared by drop casting from nonpolar solvents onto hydrophobic substrates.[41,42] Figure 1.5A shows a cross-section TEM image of a typical thick film. The individual dark spots in the image are

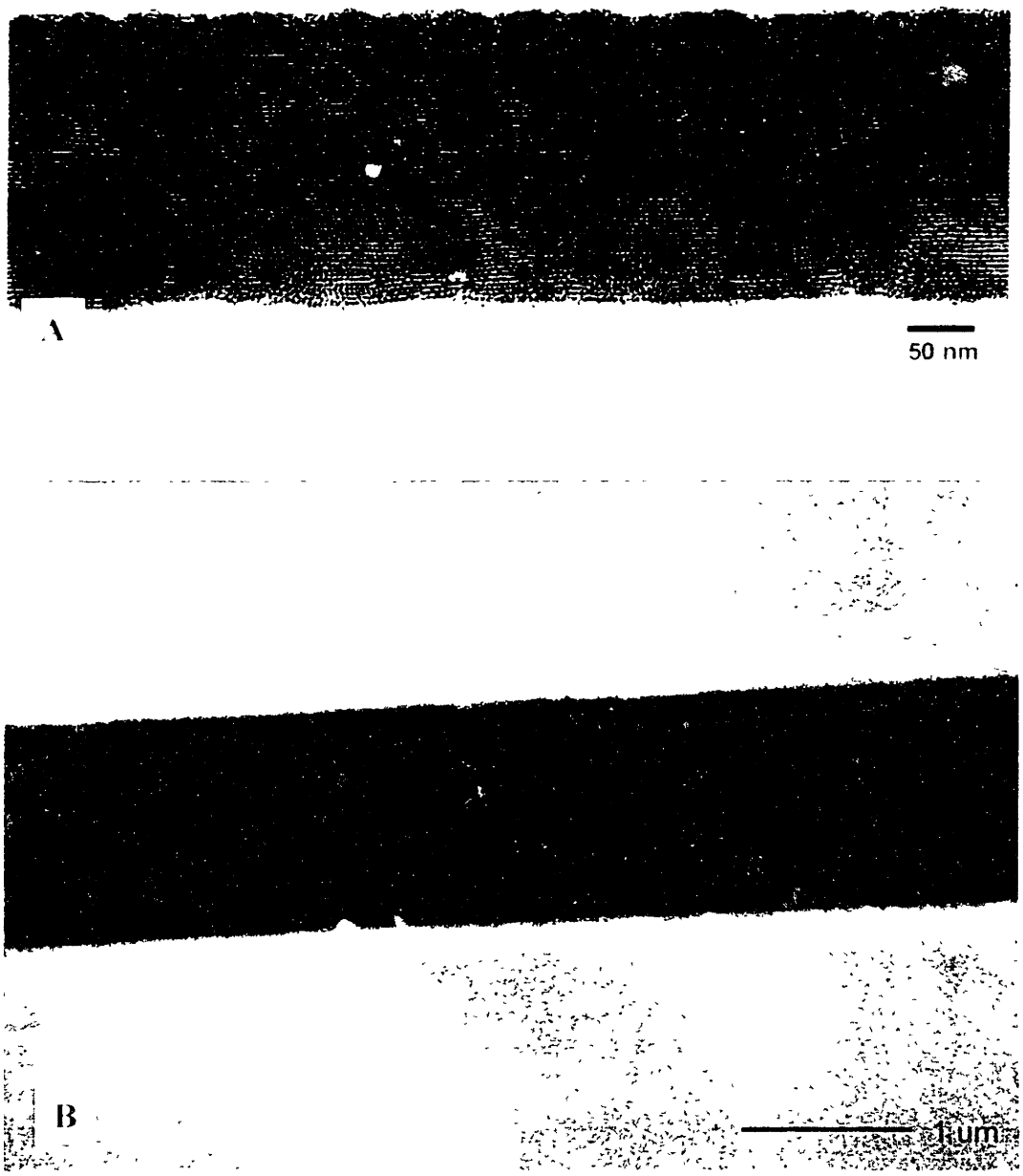

Figure 1.5: **(A)** Low resolution cross-section TEM image of a CdSe QD solid consisting of 3.5 nm QDs capped with TOPO/TOP ligands (microscopy by E. Radilowski) **(B)** High resolution SEM image of a thin CdSe QD solid on a silicon substrate. The bright areas are the gold electrodes. The QD solid is both on top of, and in between the electrodes (microscopy by N.Y. Morgan)

individual nanocrystals. Close examination shows that the QD solid is polycrystalline with intervening amorphous regions. Few defects are seen in cross-section. However, thick films are prone to lateral cracking and vent holes attributed to solvent evaporation. All of these defects are most easily remedied by preparing thin (sub 100 nm) films, increasing the boiling point of the solvent mixture to slow evaporation, limiting exposure to vacuum until the film has thoroughly dried, and avoiding rapid thermal cycling. QD solids that are free of aggregates (Figure 1.5B) and excess capping ligands are optically clear with striking thin film interference colors when prepared on silicon substrates.

1.4 Thesis overview

This thesis describes a series of experiments designed to probe the effect of dielectric confinement on the optical, electronic and transport properties of CdSe QDs. In Chapters 2 and 3, the effect of the dielectric environment on the energy of the quantum confined electronic states and on the absorption coefficient is discussed. In both cases we find that the surface ligands that surround each QD significantly reduce the sensitivity of the core to the external dielectric environment. We then tackle the problem of photoconductivity in CdSe QD solids. We find that field ionization of the photo-excited electron-hole pair controls the photoconductivity; we develop a simple tunneling model to describe the ionization process. The effect of charge separation on the photoluminescence quantum efficiency is explored further in Chapter 5. Finally, in Chapter 6 we head in a new direction with the first demonstration of amplified spontaneous emission from strongly confined, nanocrystal QDs. While seemingly unrelated, recent detailed studies of electron-hole dynamics in colloidal QDs are strongly

influenced by both the Coulomb interaction and the dielectric boundary and may limit the gain that can be achieved.[24,25]

1.5 References

[1]M.A. Kastner, "Artificial Atoms," Physics Today, 24 (1993) and references therein.

[2]M. Nirmal, D.J. Norris, M. Kuno *et al.*, "Observation of the Dark Exciton in Cdse Quantum Dots," Phys. Rev. Lett. **75**, 3728-3731 (1995).

[3]M.K. Kuno, "Band Edge Spectroscopy of CdSe Quantum Dots," Ph.D. Thesis, Massachusetts Institute of Technology, 1998.

[4]C.J.F. Bottcher, *Theory of Electric Polarization*, 2nd ed. (Elsevier, Amsterdam, 1973).

[5]L.E. Brus, "A simple model for the ionization potential, electron affinity and aqueous redox potentials of small semiconductor crystallites," J. Chem. Phys. **79**, 5566-5571 (1983).

[6]L.E. Brus, "Electron-electron and electron-hole interactions in small semiconductor crystallites: The size dependence of the lowest excited state," J. Chem. Phys. **80**, 4001 (1984).

[7]H. Grabert and M.H. Devoret, "Single Charge Tunneling: Coulomb Blockade in Nanostructures," (Plenum, New York, 1991).

[8]H. Koch and H. Lubbig, "Single-Electron Tunneling and Mesoscopic Devices," (Spring-Verlag, New York, 1991).

[9]A. Franceschetti and A. Zunger, "Pseudopotential calculations of electron and hole addition spectra of InAs, InP, and Si quantum dots," Phys. Rev. B **62**, 2614 (2000).

[10]G. Goldoni, F. Rossi, A. Orlandi *et al.*, "Enhancement of Coulomb interactions in semiconductor nanostructures by dielectric confinement," Physica E **6**, 482 (2000).

[11]R.C. Ashoori, H.L. Stormer, J.S. Weiner *et al.*, "Single-electron capacitance spectroscopy of discrete quantum levels," Phys. Rev. Lett. **68**, 3088 (1992).

[12]D. Leonard, M. Krishnamurthy, C.M. Reaves *et al.*, "Direct formation of quantum-sized dots from uniform coherent islands of InGaAs on GaAs surfaces.," Appl. Phys. Lett. **63**, 3203 (1993).

[13]P.M. Petroff and G. Medeiros-Ribeiro, "Three-Dimensional Carrier Confinement in Strain-Induced Self-Assembled Quantum Dots," Materials Research Society Bulletin, 50 (1996) and references therein.

[14]A.I. Ekimov, A.L. Efros, and A.A. Onushchenko, "Quantum-Size Effect in Semiconductor Microcrystals (Reprinted From Solid-State Commun, Vol 56, Pg 921-924, 1985)," Solid State Commun. **88**, 947-950 (1993).

[15]K. Kang, A.D. Kepner, Y.Z. Hu *et al.*, "Room-Temperature Spectral Hole-Burning and Elimination of Photodarkening in Sol-Gel Derived Cds Quantum Dots," Appl. Phys. Lett. **64**, 1487-1489 (1994).

[16]C.B. Murray, D.J. Norris, and M.G. Bawendi, "Synthesis and Characterization of Nearly Monodisperse CdSe (E = S, Se, Te) Semiconductor Nanocrystallites," J. Amer. Chem. Soc. **115**, 8706-8715 (1993).

[17]M.A. Hines and P. Guyot-Sionnest, "Synthesis and characterization of strongly luminescing ZnS- Capped CdSe nanocrystals," J. Phys. Chem. **100**, 468-471 (1996).

[18]B.O. Dabbousi, J. RodriguezViejo, F.V. Mikulec *et al.*, "(CdSe)ZnS core-shell quantum dots: Synthesis and characterization of a size series of highly luminescent nanocrystallites," J. Phys. Chem. B **101**, 9463-9475 (1997).

[19]A.A. Guzelian, U.Banin, A.V. Kadavanich *et al.*, "Colloidal chemical synthesis and characterization of InAs nanocrystal quantum dots," Appl. Phys. Lett. **69**, 1432-1434 (1996).

[20]A.L. Efros, V.A. Kharchenko, and M. Rosen, "Breaking the Phonon Bottleneck in Nanometer Quantum Dots - Role of Auger-Like Processes," Solid State Commun. **93**, 281-284 (1995).

[21]V.A. Kharchenko and M. Rosen, "Auger relaxation processes in semiconductor nanocrystals and quantum wells," J. Lumines. **70**, 158-169 (1996).

[22]V. Klimov, P.H. Bolivar, and H. Kurz, "Ultrafast carrier dynamics in semiconductor quantum dots," Phys. Rev. B **53**, 1463-1467 (1996).

[23]V.I. Klimov, A.A. Mikhailovsky, D.W. McBranch *et al.*, "Mechanisms for intra-band energy relaxation in semiconductor quantum dots: The role of electron-hole interactions," Phys. Rev. B **61**, R13349-R13352 (2000).

[24]V.I. Klimov, A.A. Mikhailovsky, D.W. McBranch *et al.*, "Quantization of multiparticle Auger rates in semiconductor quantum dots," Science **287**, 1011-1013 (2000).

[25]V.I. Klimov, A.A. Mikkhailovsky, S. Xu *et al.*, "Optical gain and stimulated emission in nanocrystal quantum dot solids," submitted (2000).

[26]D.I. Chepic, A.L. Efros, A.I. Ekimov *et al.*, "Auger Ionization of Semiconductor Quantum Drops in a Glass Matrix," J. Lumines. **47**, 113-127 (1990).

[27]M. Nirmal, B.O. Dabbousi, M.G. Bawendi *et al.*, "Fluorescence intermittency in single cadmium selenide nanocrystals," Nature **383**, 802-804 (1996).

[28]L. Esaki and R. Tsu, IBM J. Res. Dev. **14**, 61 (1970).

[29]D.B. Janes, V.R. Kolagunta, R.G. Osifchin *et al.*, "Electronic conduction through 2D arrays of nanometer diameter metal clusters," Superlattices Microstruct. **18**, 275-282 (1995).

[30]R.H. Terrill, T.A. Postlethwaite, C.H. Chen *et al.*, "Monolayers in three dimensions: NMR, SAXS, thermal, and electron hopping studies of alkanethiol stabilized gold clusters," J. Amer. Chem. Soc. **117**, 12537-12548 (1995).

[31]R.P. Andres, J.D. Bielefeld, J.I. Henderson *et al.*, "Self-assembly of a two-dimensional superlattice of molecularly linked metal clusters," Science **273**, 1690-1693 (1996).

[32]S.-H. Kim, G. Medeiros-Ribeiro, D.A.A. Ohlberg *et al.*, "Individual and Collective Electronic Properties of Ag Nanocrystals," J. Phys. Chem. B **103**, 10341 (1999).

[33]A.A. Middleton and N.S. Wingreen, "Collective Transport in Arrays of Small Metallic Dots," Phys. Rev. Lett. **71**, 3198-3201 (1993).

[34]A.J. Rimberg, T.R. Ho, and J. Clarke, "Scaling behavior in the current-voltage characteristic of one and two dimensional arrays of small metallic islands," Phys. Rev. Lett. **74**, 4714 (1995).

[35]C.P. Collier, R.J. Saykally, J.J. Shiang *et al.*, "Reversible tuning of silver quantum dot monolayers through the metal-insulator transition," Science **277**, 1978-1981 (1997).

[36]H.-O. Muller, K. Katayama, and H. Mizuta, "Effects of disorder on the blockade voltage of two-dimensional quantum dot arrays," J. Appl. Phys. **84**, 5603 (1998).

[37]J.R. Heath, C.M. Knobler, and D.V. Leff, "Pressure/temperature phase diagrams and superlattices of organically functionalized metal nanocrystal monolayers: The influence of particle size, size distribution, and surface passivant," J. Phys. Chem. B **101**, 189-197 (1997).

[38]B.A. Korgel and D. Fitzmaurice, "Condensation of ordered nanocrystal thin films," Phys. Rev. Lett. **80**, 3531-3534 (1998).

[39]B.A. Korgel, S. Fullam, S. Connolly *et al.*, "Assembly and self-organization of silver nanocrystal superlattices: ordered "soft spheres"," J. Phys. Chem. B **102**, 8379 (1998).

[40]P.C. Ohara, D.V. Leff, J.R. Heath *et al.*, "Crystallization of Opals from Polydisperse Nanoparticles," Phys. Rev. Lett. **75**, 3466 (1995).

[41]C.R. Kagan, "The Electronic and Optical Properties of Close Packed Cadmium Selenide Quantum Dot Solids," Ph.D. Thesis, Massachusetts Institute of Technology, 1996.

[42]C.B. Murray, C.R. Kagan, and M.G. Bawendi, "Self-Organization of CdSe Nanocrystallites Into 3-Dimensional Quantum-Dot Superlattices," Science **270**, 1335-1338 (1995).

Chapter 2

Observation of solvatochromism

2.1 Introduction

Solvatochromism refers to a change in the energy of an optical transition when a chromophore is dispersed in different solvents. In molecular systems, solvatochromism arises from dipole- (induced) dipole or dispersion interactions with the solvent molecules.[1] This effect is commonly used to advantage in modern studies of solvation dynamics. For example, by monitoring the emission energy of the chromophore as a function of time, one can make inferences about the dynamics of the solvent cage around the chromophore.[2]

Similar interactions with the dielectric environment influence the electronic states of semiconductor QDs. Dielectric mismatch in the presence of an electric field results in a surface polarization charge at the interface of the two materials. As was outlined in Chapter 1, the bound charge may interact with charges confined within the QD thereby affecting the energy of the exciton and the optical band gap.[3,4] Numerous theoretical papers have presented calculations of the predicted polarization energy as a function of external dielectric environment, [5-10] QD size, and shape.[11] In addition, the dielectric environment may be important in the presence or absence of surface states.[12,13]

Since they may be easily dispersed in a variety of solvents with different dielectric constants, colloidal semiconductor QDs are a convenient system in which to test models of the polarization energy for QD systems. In this chapter, we show that the

optical band gap of CdSe QDs decreases slightly as the solvent dielectric constant is increased. Simple analytical models of the polarization energy appear to overestimate the effect of the dielectric environment. Satisfactory agreement with the data can be found by accounting for the screening provided by the ligand shell around the QDs.

Solvatochromism measurements also allow us to address the important question of inter-dot coupling in close-packed arrays of semiconductor QDs. Linear absorption spectroscopy is commonly used as a probe of inter-particle coupling. In practice, changes in the absorption spectrum may be due to the dielectric environment, classical electromagnetic dipole or multipole coupling, or quantum mechanical coupling (i.e. the wavefunction is delocalized over more than one QD to form extended states). For example when gold nanoparticles aggregate, electromagnetic coupling of the plasmon resonances on nearby particles results in a dramatic color change[14] that can be used in colorimetric based detection schemes for nanoparticle tagged biomolecules.[15] Several authors have observed red shifts of the absorption edge when close-packed films of colloidal semiconductor QDs are prepared.[16,17] For very small clusters, it has been suggested that the red shift is due to quantum mechanical coupling of adjacent QDs.[18] We examine this hypothesis by comparing the absorption shifts of monodisperse and mixed size QD solids. Our analysis suggests that for larger clusters (2-6 nm diameter) the absorption shift is dominated by the effect of the external dielectric environment.

2.2 Experiment

CdSe QDs passivated by tri-octylphosphine/tri-octylphosphine oxide (TOP/TOPO) ligands are prepared following the method of Murray *et al.* [19] QDs are isolated from the excess TOPO/TOP by repeated (3X) size selection from *n*-

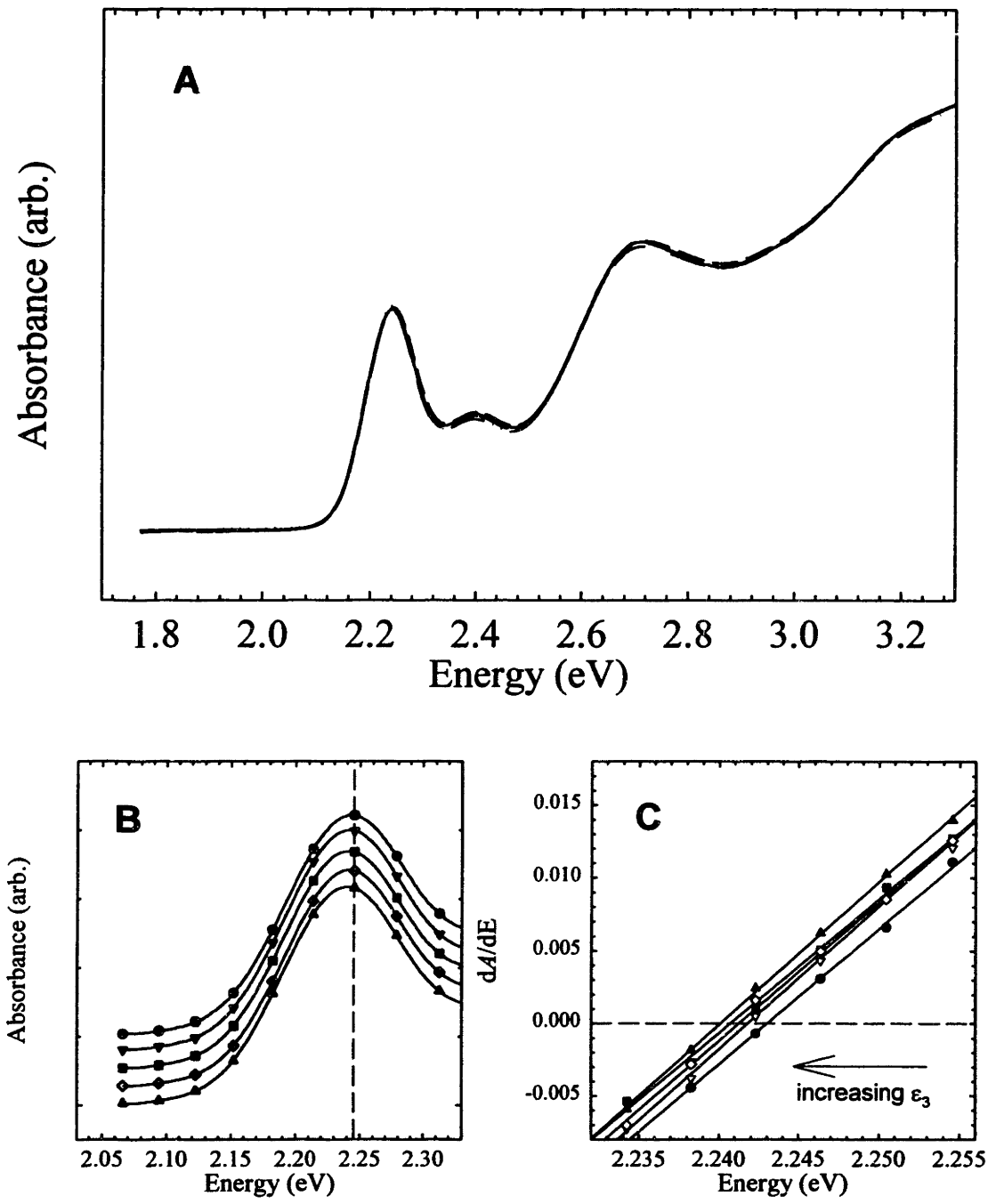

Figure 2.1 **(A)** Room temperature absorption spectra for 20 Å TBPO/TBP capped CdSe QDs dispersed in various solvents. **(B)** Blow-up of the region near the $1S_e1S_{3/2h}$ feature for QDs in hexane (●), chloroform (▽), toluene(■), 3-bromotoluene (◇), and 3-iodotoluene (▲). Spectra have been offset for clarity. **(C)** The inset shows the first derivative spectra in the region of the lowest energy absorption feature. Symbols refer to the same samples as in (B). The zero-crossing moves to lower energies with increasing solvent dielectric constant.

butanol/methanol dispersions followed by drying under vacuum. To form close-packed QD solids, concentrated dispersions (~ 100 mg/mL) of QDs in 90% hexane/10% octane are drop cast on clean microscope slides to form optically clear and thin solid films. Tri-butylphosphine/tri-butylphosphine oxide (TBPO/TBP) passivated QDs are prepared by repeated dissolution in neat TBPO/TBP and stirring overnight at 60°C. QD radii[19] and inter-particle separation[20] in QD solids are quoted from previously published results.

Linear absorption spectra are obtained using a Cary 5E UV-Vis-NIR spectrophotometer operating in dual beam mode with 2 nm spectral bandwidth and sampling every 0.1 nm. Solution spectra are obtained using the same quartz cuvette for both reference and sample. For each sample, an aliquot of the stock dispersion is vaacuum dried to a powder and then re-dispersed in the new solvent taking care to ensure that the QDs re-disperse fully. Spectra of close-packed films are obtained using pre-cleaned microscope slides as substrates. Error from the fluorescence of the QDs is minimized by washing the QDs with methanol several times to reduce the photoluminescence quantum yield (QY) to ~ 1%. Photoluminescence QY measurements are made using a SPEX Fluorolog spectrophotometer.

2.3 Results

Figure 2.1 shows linear absorption spectra for 20 Å radius CdSe QDs with TBPO/TBP surface ligands dispersed in hexane, chloroform, toluene, 3-bromotoluene, and 3-iodotoluene (all solvents from Aldrich, > 98% purity). Each dispersion has identical nominal concentration of QDs and is optically clear. A slight red shift of the absorption edge is observed with increasing solvent refractive index. The shift in the first

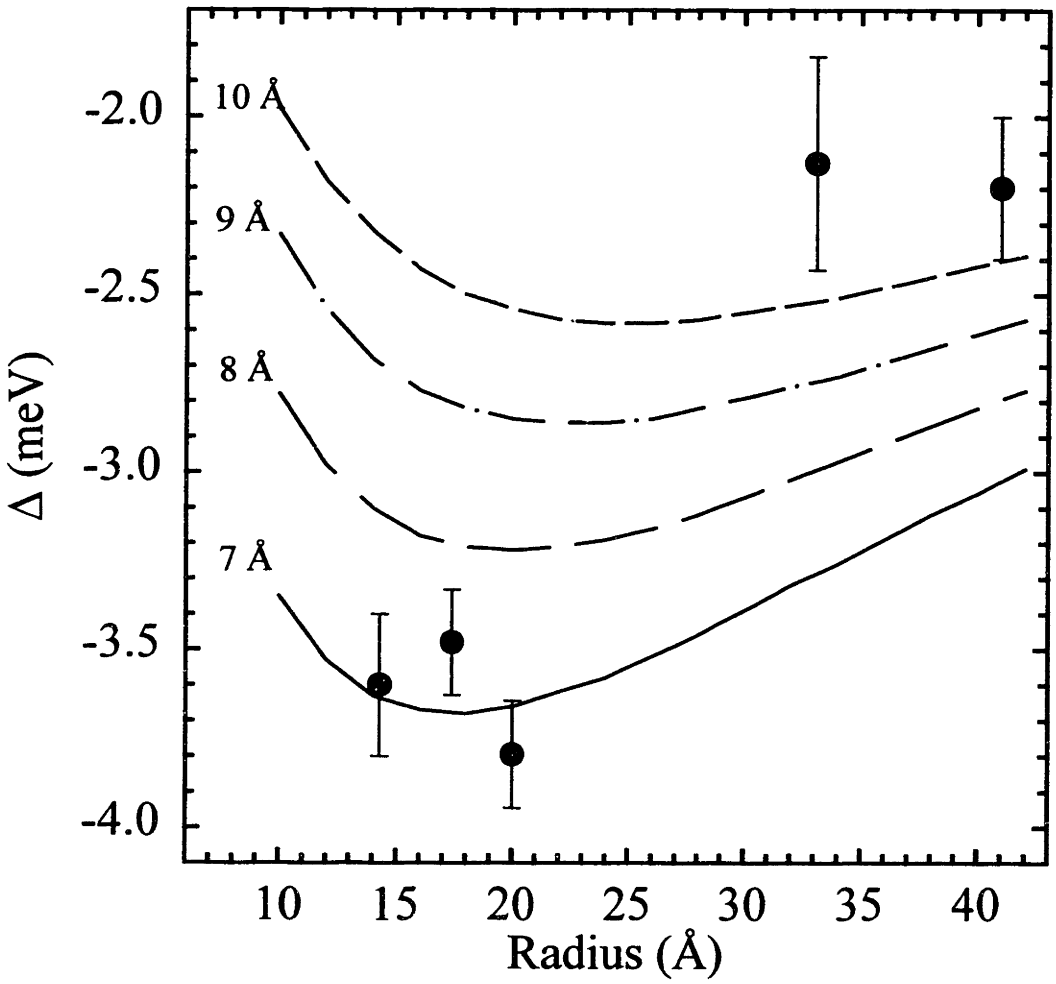

Figure 2.2 Observed and predicted solvatochromatic shifts as a function of QD size. Symbols are the observed solvatochromatic shift between hexane and 3-iodotoluene dispersion. Theoretical predictions based on the inorganic core-organic shell model are shown for various shell thicknesses with dielectric constant $\varepsilon_2 = 2.1$. See text.

absorption feature ($1S_e1S_{3/2h}$ transition) is more easily observed by plotting the derivative spectra (Figure 2.1C) and fitting a straight line to the data near the zero-crossing (peak maxima). The higher energy optical transitions and the band edge PL also red shift by approximately the same amount as the $1S_e1S_{3/2h}$ transition. However since perturbation theory limits our quantitative analysis of the polarization energy to the lowest excited state, from this point forward we concentrate on the $1S_e1S_{3/2h}$ transition.

In Figure 2.2, we plot the energy difference between QDs dispersed in 3-iodotoluene and QDs in hexane for a size series of TOPO/TOP capped QDs. The shift in the $1S_e1S_{3/2h}$ transition is larger for small QDs (15-20 Å) than for large QDs (30-40 Å). This is expected as the quantum-confined exciton of smaller QDs is on average closer to the surface polarization charge and the solvent molecules. We observe that changing the alkane chain length (and effectively the distance of closest approach of the solvent molecules to the QD surface) does not change the solvatochromatic shift significantly. Figure 2.3 shows data for 20 Å TOPO/TOP and TBPO/TBP capped QDs dispersed in the same solvent series as above (C8 and C4 alkane chains respectively). The theoretical fits in Figure 2.3 will be discussed in Sec. 2.4.3.

By preparing close-packed solids of QDs one can further increase the external dielectric constant around the QDs. Figure 2.4 shows the reversible absorption shift between hexane dispersion and close-packed film for 20 Å QDs with TOPO/TOP ligands. Each quantum-confined exciton is now effectively embedded in a matrix of CdSe and the organic ligands. To determine the contribution of inter-dot coupling to the absorption shift, we prepare 1:10 mixtures of large (23.8 Å) QDs and small (13.2 Å) QDs

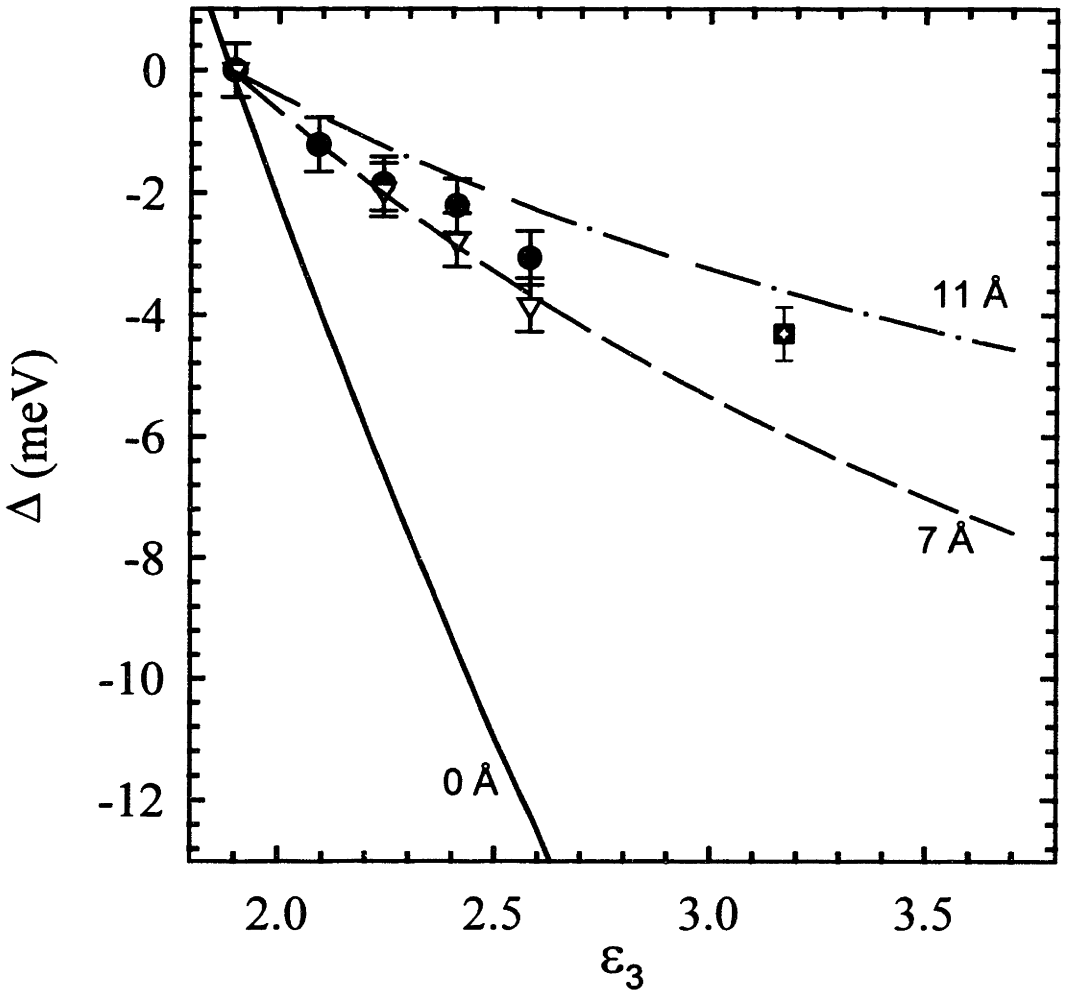

Figure 2.3: Observed and predicted solvatochromatic shifts with respect to hexane dispersion for the $1S_e1S_{3/2h}$ electronic transition. Symbols are the observed shifts for 20 Å QDs capped with (▽) TOPO/TOP ligands and (●) TBPO/TBP ligands. The observed shift for a close-packed solid of approximately the same size QDs is shown by the square (■). The solid line is the theoretical shift for this core radius based on equations (2.3)-(2.5). The predicted solvatochromatic shift using the core-shell model (equations 2.5, 2.6) is shown for 7 Å (dashed) and 11 Å (dash-dot) dielectric shells (ε_2 =2.1) surrounding each QD.

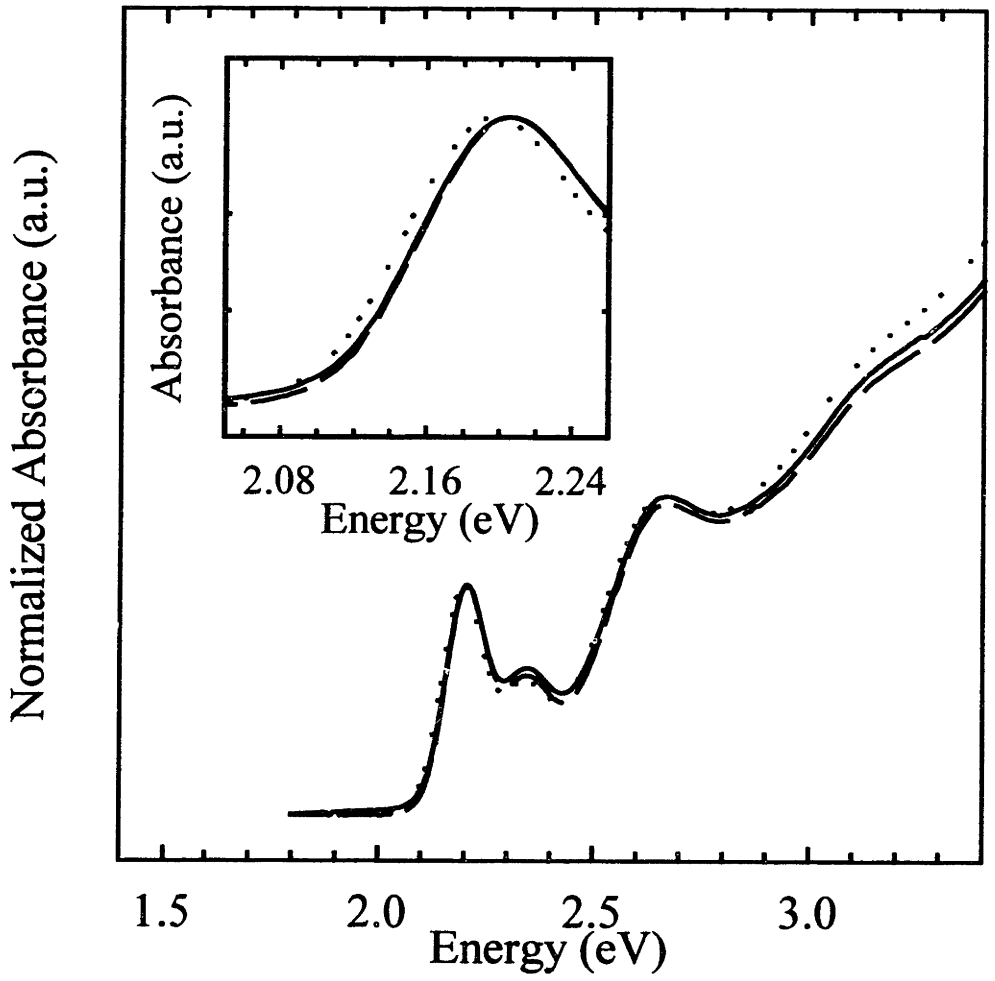

Figure 2.4: Room temperature absorption spectra for 20 Å TOPO/TOP capped QDs as a dispersion in hexane (solid lines), a close-packed QD solid on glass (dotted line), and the same QDs re-dispersed in hexane (dashed line).

TABLE 2.1: Observed and predicted position of the first absorption feature for 23.8 Å QDs as pure dispersions and close-packed solids, and when mixed with 13.2 Å QDs.

Sample	Observed (nm)	Predicted (nm)
Large QD dispersion	584.25	*
Large QD solid	585.44	585.3 ± 0.1[a]
Mixed QD dispersion	584.01	584.1 ± 0.1[b]
Mixed QD solid	585.84	585.7 ± 0.1[c]
		584.9[d]
		586.2[e]

[a] core-shell model (b-a = 9Å, $\varepsilon_{ave} = 2.84$).
[b] predicted position for spectra = 10x (small QD dispersion) + 1x (large QD dispersion)
[c] mixed dispersion position + shift based on the core shell model, $\varepsilon_{ave} = 2.58$, b-a = 9Å
[d] predicted position for spectra = A x (small QD solid) + B x (large QD dispersion)
[e] predicted position for spectra = A x (small QD solid) + B x (large QD solid)

and measure the absorption shift with respect to a pure dispersion of the large QDs. If coupling of adjacent QD electronic states is the dominant contribution to the observed shift, then the $1S_e1S_{3/2h}$ transition of the large QDs should not shift in the mixed QD system. *

The results of this experiment are shown in Figure 2.5 and Table 2.1. The predicted peak position is determined by measuring the absorption spectra for the pure QD solids or dispersions and then adding these spectra in the appropriate ratio to best match the observed, mixed, spectrum. For the mixed dispersions of QDs (case b), good agreement between the observed and predicted peak position is found. For the mixed QD

* Kagan showed that the different sizes of QDs remain well mixed and do not phase separate when deposited from hexane/octane mixtures. See C. R. Kagan, Ph. D. thesis, Massachusetts Institute of Technology, 2000. Page 68.

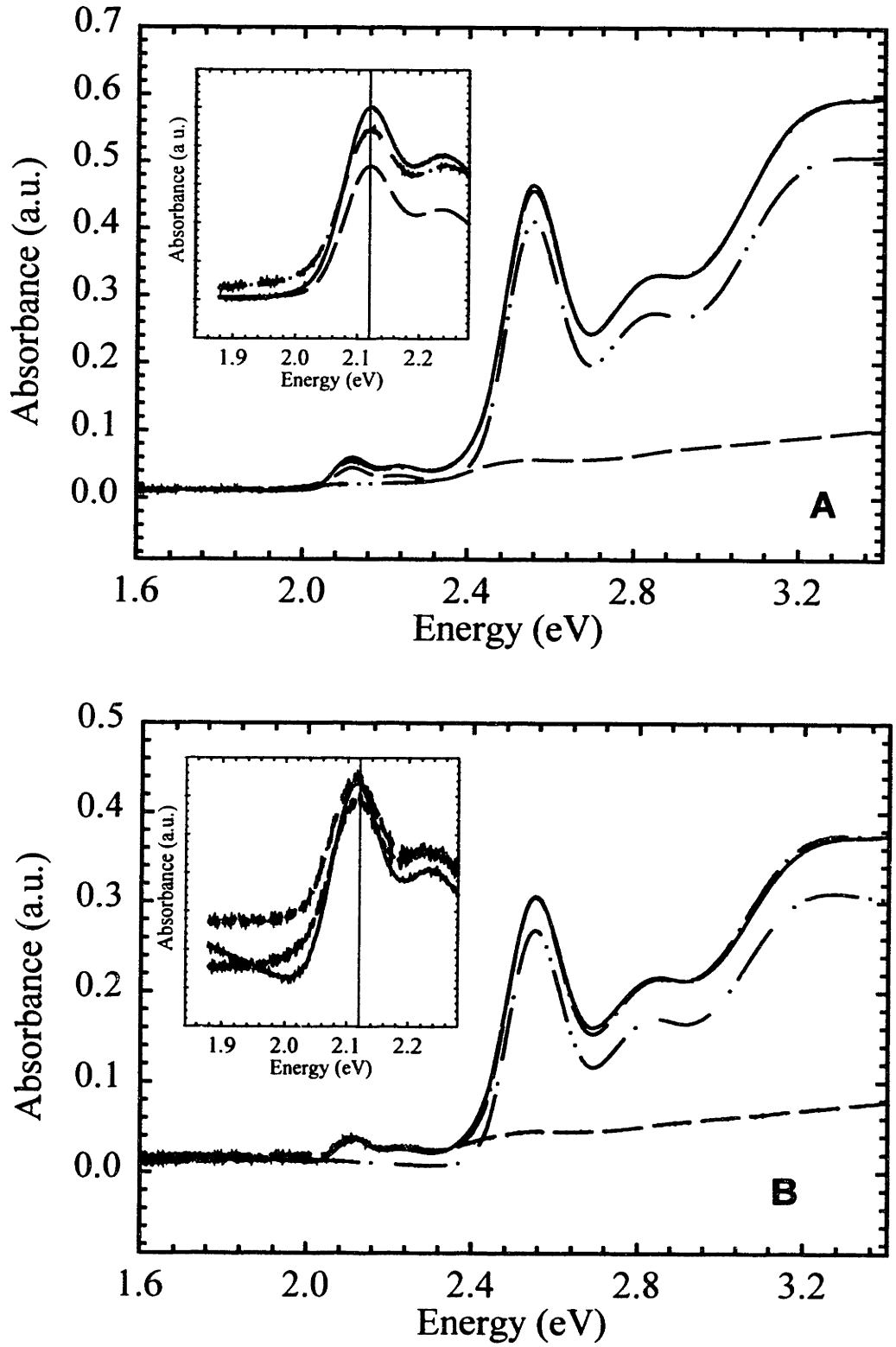

Figure 2.5: Linear absorption spectra of pure and mixed QDs **(A)** as dilute dispersions and **(B)** as close-packed QDs. The experimental data for mixed QDs (solid line), large QDs (dashed) and small QDs (dash-dot-dot). The dash-dot line indicates the best fit to the experimental mixed spectrum found by taking a linear combination of the large and small QD spectra. The insets show band edge absorbance for the large QDs in all cases.

solid, we calculate the predicted peak position for three different scenarios. In case (d) we assume that there is no absorption shift of the large QDs; thus, the total absorption spectrum is the sum of the small QD solid spectrum plus the large QD dispersion spectrum. In case (e) we assume that the spectra of both the small and large QDs shift and thus the total absorption spectrum is the sum of the two QD solids. Table 2.1 shows that the observed peak position is in between these two extremes. The predicted peak positions based on cases (a) and (c) are discussed in the following section.

2.4 Discussion

In the previous section we demonstrated that absorption spectrum of CdSe QDs shifts to lower energies with increasing solvent dielectric constant. Before proceeding to a detailed analysis of the effect of the dielectric environment, it is important to eliminate other factors that could cause spurious shifts of the spectra. Even for nearly monodisperse QDs, as used in this experiment, the remnant size distribution still affects the shape and energy of the absorption spectrum. If varying solubility of the QDs was causing the absorption shifts, we would expect that with increasing solvent polarity, the largest particles would flocculate first (strongest van der Waals interactions) leading to a blue shift of the absorption spectrum. This is not observed. Furthermore, all the dispersions were optically clear (optical density < 0.01 below band gap) suggesting that aggregation does not make a significant contribution. Thus, we assign the red shift of the absorption spectrum to changes in the dielectric environment that perturb the energy of the quantum-confined exciton.

2.4.1 Theoretical models of the polarization energy

The total energy of an exciton confined to a spherical semiconductor QD can be expressed as the sum of the bulk band gap, the kinetic energy of each carrier due to quantum confinement, the energy from the direct Coulomb interaction of the electron-hole pair, the self charging energy for each carrier ($\Sigma_{e(h)}^{pol}$), and the polarization energy from the interaction of each carrier with the image charge of the opposite carrier ($J_{e,h}^{pol}$).

$$E_{gap}^{opt} = E_g^{bulk} + E_e^{kin} + E_h^{kin} + E_{coul}^{dir} + \Sigma_h^{pol} + \Sigma_e^{pol} + J_{e,h}^{pol} \qquad (2.1)$$

The first four terms depend only on the dielectric constant inside the QD (ε_1). The last three polarization terms depend strongly on the contrast between the internal and external dielectric environment ($\varepsilon_1/\varepsilon_3$).

Calculations of $\Sigma_{e(h)}^{pol}$ and $J_{e,h}^{pol}$ are generally addressed using perturbation theory. Using the effective-mass approximation and assuming an infinite potential barrier at the interface, the lowest energy conduction band electron in a QD of radius a has envelope wavefunction $\Psi(r) \sim \sin(\pi r / a)/ r$. The self energy $\Sigma_{e(h)}^{pol}$ due to the image charge distribution on the surface when a hole(electron) is added to the highest valence (lowest conduction) band state is given by $\Sigma_{h(e)}^{pol} = \frac{1}{2}\langle \Psi_0 | V_{in}(r,r') | \Psi_0 \rangle$ where V_{in} is the polarization potential created by the image charge. For the case treated theoretically by Brus[4] and others[5,7], the indirect polarization potential at point r, created by a point charge q at position r' within a spherical region is given by,

$$V_{in}(r,r') = \frac{q}{4\pi\varepsilon_0\varepsilon_1}\sum_{l=0}^{\infty} A_l r^l r'^l P_l(\cos\theta) \qquad (2.2)$$

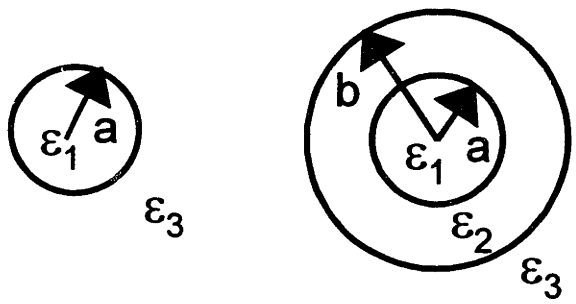

Figure 2.6 Cartoon of the core and core-shell models used for the polarization energy. "a" is the radius of the QD. "a+b" is the radius of the core plus the inorganic shell. In both cases, spherically symmetric wavefunctions, restricted to the area r< a, are used.

where P_l is the Legendre polynomial and θ is the angle between r and r'. For the case where the image charge is at the interface between regions I and III (see cartoon in Figure 2.5), the coefficient A_l is given by,

$$A_l = \frac{l+1}{a^{2l+1}} \frac{\varepsilon_1 - \varepsilon_3}{\varepsilon_3 + l(\varepsilon_1 + \varepsilon_3)} \tag{2.3}$$

From reference [5], $J_{e,h}^{pol}$ is given by,

$$\begin{aligned} J_{e,h}^{pol} &= \iint \Psi_e(r')\Psi_h(r')V_{in}(r,r')\Psi_e(r)\Psi_h(r)dr'dr \\ &= \frac{-q^2}{4\pi\varepsilon_0\varepsilon_1 a}\left(\frac{1}{\varepsilon_3} - \frac{1}{\varepsilon_1}\right) \end{aligned} \tag{2.4}$$

The $l=0$ terms in Σ_e^{pol} and Σ_h^{pol} exactly cancel $J_{e,h}^{pol}$ so that the net correction to the $1S_e1S_h$ exciton energy from the interaction with the image charge is given by,

$$\delta = \frac{\pi q^2}{2\varepsilon_0\varepsilon_1 a}\sum_{l=1}^{\infty} a^{2l+1} A_l \int_0^1 j_0{}^2(\pi x) x^{2l+2} dx \tag{2.5}$$

where j_0 is the spherical Bessel function.

Iwamatsu *et al.* considered the effect of a dielectric discontinuity for the case of a spherical QD surrounded by a shell of a second material with dielectric constant ε_2 and thickness (b-a) (see Figure 2.5) and then embedded in a dielectric medium (ε_3).[8] In this case A_l is given by

$$A_l = \frac{(l+1)}{a^{2l+1}} \frac{a^{2l+1}(\varepsilon_2-\varepsilon_3)(\varepsilon_1+l(\varepsilon_1+\varepsilon_2))+b^{2l+1}(\varepsilon_1-\varepsilon_2)(\varepsilon_3+l(\varepsilon_2+\varepsilon_3))}{a^{2l+1}(\varepsilon_1-\varepsilon_2)(\varepsilon_2-\varepsilon_3)l(l+1)+b^{2l+1}(\varepsilon_2+l(\varepsilon_1+\varepsilon_2))(\varepsilon_3+l(\varepsilon_2+\varepsilon_3))} \qquad (2.6)$$

The rest of the derivation of the polarization energy follows as before including the cancellation of the $l=0$ terms so that the correction to the exciton energy is given by (2.5) and substituting equation (2.6) for A_l.

2.4.2 Comparison to experiment: dilute dispersions

In Figure 2.3, we plot the energy of the first absorption feature from the data in Figure 2.1 with respect to the value for the same QDs dispersed in hexane (Δ) versus the square of the solvent refractive index.[21] The dashed line shows the predicted energy shift based on equations (2.3)-(2.5) where the image charge is considered to be exactly at the surface of the QD. The bulk high-frequency dielectric constant for CdSe (ε_1= 6.2) is assumed. The predicted energy shift is much larger than the observed energy shift. Using this model, it is not possible to match the data without assuming an unphysically large radius (~ 4a). The solid line in Figure 2.3 is the theoretically predicted energy shift with respect to hexane dispersion using the core-shell model (Equations 2.5 and 2.6) and again using ε_1= 6.2. Although there is no unique fit based on both shell thickness and ε_2, we can choose a physical solution by setting ε_2 equal to the dielectric constant of the ligand shell that surrounds each QD. Satisfactory agreement with the data is found setting the shell dielectric constant ε_2 = 2.1 and using the shell thickness *b* as the only fit

parameter.* For the best fit, we find that the shell thickness is ~ 8 Å, in reasonable agreement with the extended chain length for TBPO (~ 6.7 Å).

2.4.3 Comparison to experiment: QD solids

In Figure 2.3 we also include the observed absorption shift for a QD solid (shown by the square) of similar size as used for the solvent series. Here ε_3 is calculated for randomly close-packed spheres (fill factor = 0.64) of semiconductor (ε^{∞} =6.2 for bulk CdSe) with an organic shell of width (d) and dielectric constant $\varepsilon \sim 2$. The interstices are filled with the same organic material. The observed absorption shift is in near quantitative agreement with what would be expected from the average external dielectric environment using the inorganic core-organic shell model. The data in Table 2.1 also shows remarkably good agreement with this model. The $1S_e1S_{3/2h}$ transition for the large QDs shifts to the red with respect to hexane dispersion both for the monodisperse QD solid and when the QDs are "diluted" in a solid of small QDs. In the latter case, there should be little coupling between electronic states on adjacent QDs. Case (a) in Table 2.1 is the predicted $1S_e1S_{3/2h}$ peak position in the QD solid for monodisperse 23.8 Å QDs given the volume weighted dielectric constant of the composite and b-a = 9 Å. When the large QDs are diluted in the small QDs, the volume fraction of semiconductor material is smaller leading to a reduced average dielectric constant and correspondingly smaller absorption shift (case c).

* Note that in the fits of Figures 2.2 and 2.3, we plot the change in energy (Δ) of the exciton with respect to the value in hexane dispersion, not the absolute value of the polarization energy. As a result, the theoretical curves for different shell thicknesses only cross for ε_3 = 1.89 (hexane) and not when $\varepsilon_2 = \varepsilon_3$ as one would intuitively expect.

2.4.4 Effect of the thickness of the ligand shell

The inorganic core-organic shell model is physically consistent with the monolayer of phospho-alkane ligands that surround each QD and provide a barrier to solvent molecules approaching the surface. In solvatochromism of molecular species, it is found that 90% of the solute-solvent interaction is with the first solvent shell. [1] Thus it is reasonable that the QD-ligand shell interaction dominates. An important test of theory is to change the shell thickness. Although TOPO/TOP ligands have twice the nominal chain length of TBPO/TBP ligands, the predicted difference is small and close to our measurement uncertainty in this experiment. We observe that QDs capped with the two different ligands exhibit the same solvatochromatic shifts within experimental error.

The degree of penetration of solvent molecules into the ligand shell may be expected to depend on QD core size and ligand chain length as well as chemical and steric interactions with the solvent molecules. Measurements of the hydrodynamic radii of gold nanoclusters with alkanethiolate (C10 and C12 alkanes) ligands suggest that for larger clusters with radius > 20 Å, the outer part of the ligand shell is relatively fluid.[22] As a result the hydrodynamic radius is less than would be expected from calculations of the core radius plus extended alkane chain length. Thus for a given size QD, the portion of the ligand shell that is impenetrable to the solvent molecules may be similar for both TBPO/TBP and TOPO/TOP capped QDs resulting in a similar absorption shift. When the radius of curvature of the particle is lower (larger QDs), the capping ligands may pack more tightly and be more impenetrable to the solvent. We observe that the absorption shifts for the large radius particles (30-40 Å) are more consistent with a 10-11 Å shell than for the 15-20 Å particles which appeared to have an 8 Å dielectric shell (see fits in Figure 2.2).

The core-shell model for the polarization energy only modifies the image charge potential felt by charges confined to the QD. Further improvements in the theoretical models should be possible using more realistic wavefunctions for the electron and hole* and accounting for correlation in the positions of the two charges. Qualitatively, electron-hole pairs in small QDs should exhibit little correlation since the quantum confinement effects are much larger than the Coulomb interaction (strong confinement regime). As the radius is increased, the Coulomb interaction becomes more important and electron-hole correlation should increase thereby affecting the polarization energy.

Finally, we note that within our experimental error, there is no change in the extinction coefficient of the QDs. Theory predicts that the absorption coefficient of a composite containing spherical nanoparticles embedded in a dielectric medium (ε_0) is proportional to f^2, where f is a local field factor approximately equal to the ratio of the electric field inside and outside the nanoparticles, $f(\omega)=3\varepsilon_0/(\varepsilon(\omega)+2\varepsilon_0)$.[23] From this mechanism, one would predict that the absorption coefficient for QDs in 3-iodotoluene could be as much as 40% larger than the absorption coefficient for the same QDs in hexane. Such strong dependence on the solvent dielectric constant is not observed. As with the polarization energy, the calculations of the local field may have to account for the effect of the ligand shell in order to correctly predict the absorption coefficient. We address this problem in the next chapter.

2.5 Conclusions

Solvatochromatic shifts observed for CdSe QDs are consistent with the change in polarization energy of the exciton if the effect of the ligand shell is included. The

* Pseudopotential calculations for 19.2 Å CdSe QDs (no ligand shell) predict an ~ 25 meV shift of the

observation of an absorption shift in the mixed QD system and the excellent agreement with the core-shell model make a convincing argument that for QDs in this size range, the absorption shifts are dominated by the dielectric environment.

2.6 References

[1]P. Suppan and N. Ghoneim, *Solvatochromism* (The Royal Society of Chemistry, Cambridge, 1997).

[2]J.D. Simon, "Time-Resolved Studies of Solvation in Polar Media," Accounts Chem. Res. **23** (3), 128-134 (1988).

[3]L.E. Brus, "A simple model for the ionization potential, electron affinity and aqueous redox potentials of small semiconductor crystallites," J. Chem. Phys. **79** (11), 5566-5571 (1983).

[4]L.E. Brus, "Electron-electron and electron-hole interactions in small semiconductor crystallites: The size dependence of the lowest excited state," J. Chem. Phys. **80** (9), 4001 (1984).

[5]D. Babic, R. Tsu, and R.F. Greene, "Ground state energies of one-and two-electron silicon dots in an amorphous silicon dioxide matrix," Phys. Rev. B **45** (24), 14150-14155 (1992).

[6]T. Takagahara, "Effects of dielectric confinement and electron-hole exchange interaction on excitonic states in semiconductor quantum dots," Phys. Rev. B: **47** (8), 4569-4584 (1993).

[7]G. Allan, C. Delerue, M. Lannoo *et al.*, "Hydrogenic impurity levels, dielectric constant, and Coulomb charging effects in silicon crystallites.," Phys. Rev. B: **52** (16), 11982-11988 (1995).

[8]M. Iwamatsu, M. Fujiwara, N. Happo *et al.*, "Effects of dielectric discontinuity on the ground-state energy of charged Si dots covered with a SiO2 layer.," J. Phys. Condes. Mat. **9**, 9881-9892 (1997).

[9]A. Franceschetti and A. Zunger, "Pseudopotential calculations of electron and hole addition spectra of InAs, InP, and Si quantum dots," Phys. Rev. B **62** (4), 2614 (2000).

[10]A. Franceschetti and A. Zunger, "Addition energies and quasiparticle gap of CdSe nanocrystals," Appl. Phys. Lett. **76** (13), 1731 (2000).

[11]P.G. Bolcatto and C.R. Proetto, "Shape and dielectric mismatch effects in semiconductor quantum dots," Phys. Rev. B **59** (19), 12487-12498 (1999).

[12]L. Banyai, P. Gilliot, Y.Z. Hu *et al.*, "Surface -polarization instabilities of electron-hole pairs in semiconductor quantum dots," Phys.Rev.B **5** (14136) (1992).

[13]E. Rabini, B. Hetenyi, and B.J. Berne, "Electronic properties of CdSe nanocrystals in the absence and presence of a dielectric medium," J. Chem. Phys. **110** (11), 5355-5369 (1999).

[14]M. Quinten, "Optical effects associated with a$_{gg}$egates of clusters," Journal of Cluster Science **10** (2), 319-358 (1999).

[15]R. Elghanian, J.J. Storhoff, R.C. Mucic *et al.*, "Selective colorimetric detection of polynucleotides based on the distance-dependent optical properties of gold nanoparticles," Science **277** (5329), 1078-1081 (1997).

---

optical band gap between ε_3=2 and ε_3 = 3. A. Franceschetti, private communication.

[16]T. Vossmeyer, L. Katsikas, M. Giersig *et al.*, "CdS Nanoclusters: Synthesis, Characterization, Size Dependent Oscillator Strength, Temperature Shift of the Excitonic Transition Energy, and Reversible Absorbance Shift," J. Phys. Chem. **98** (31), 7665-7673 (1994).

[17]C.R. Kagan, C.B. Murray, and M.G. Bawendi, "Synthesis, Structural Characterization, and Optical Spectroscopy of Close Packed CdSe Nanocrystallites,"in *Microcrystalline and Nanocrystalline Semiconductors*, edited by L.Brus, M. Hirose, R.W. Collins, F. Koch, and C.C. Tsai, MRS Symposia Proceedings No. 358 (Materials Research Society, Boston, 1995), p. 219.

[8]M.V. Artemyev, "Evolution from individual to collective electron states in a dense quantum dot ensemble," Phys. Rev. B: **60** (3), 1504-1506 (1999).

[19]C.B. Murray, D.J. Norris, and M.G. Bawendi, "Synthesis and Characterization of Nearly Monodisperse CdSe (E = S, Se, Te) Semiconductor Nanocrystallites," J. Amer. Chem. Soc. **115** (19), 8706-8715 (1993).

[20]C.B. Murray, C.R. Kagan, and M.G. Bawendi, "Self-Organization of Cdse Nanocrystallites Into 3-Dimensional Quantum-Dot Superlattices," Science **270** (5240), 1335-1338 (1995).

[21]D.R. Lide, "CRC Handbook of Chemistry and Physics," (CRC Press, New York, 1999).

[22]W.P. Wuelfing, A.C. Templeton, J.F. Hicks *et al.*, "Taylor Dispersion Measurements of Monolayer Protected Clusters: A Physicochemical Determination of Nanoparticle Size," Analytical Chemistry **71** (18), 4069-4074 (1999).

[23]D. Ricard, M. Ghanassi, and M.C. Schanne-Klein, "Dielectric confinement and the linear and nonlinear optical properties of semiconductor-doped glasses," Optics Communications **108**, 311-318 (1994).

Chapter 3

On the absorption cross-section

3.1 Introduction

There is great interest in using semiconductor quantum dots (QDs) in novel linear and nonlinear optical devices. [1] For the design of such devices, as well in detailed studies of the dynamics of electron and holes in the QDs, knowledge of the absorption-cross section per QD is essential. In order to deduce the average number of electron-hole pairs produced per incident photon one needs to know the absorption cross-section and the photon flux. Surprisingly, the absolute linear absorption cross-section for interband transitions in CdSe QDs is not well known. One reason for this absence of a key parameter is the difficulty of accurately counting particles rather than ions or molecules. To date all published determinations of the extinction coefficient for nanoparticle systems have relied either on decomposing the nanoparticle and analyzing for the concentration of one of the component ions, [2,3] or gravimetric analysis.[4] Both procedures require very narrow size distributions in order to avoid large uncertainties in the particle concentration and thus the extinction coefficient. In the latter method, the mass of the surface ligands adds further uncertainty. In this chapter we prepare nearly monodisperse dispersions of CdSe QDs and determine the absorption cross-section per particle to within 15% based on the yield of the reaction. We observe that the absorption coefficient far above the band edge scales approximately as the QD radius cubed. We fit the data using models for light scattering from small particles and find excellent agreement for colloidal dispersions in hexane.

In addition to obtaining a working value for the absorption cross-section, we also perform some simple experiments to test available theoretical models for this parameter.[5-7] Many recent calculations [8-12] are aimed at accounting for the self-reaction of the QD in the light field—the electric field of the electromagnetic wave causes the QD to polarize which in turn acts on the potential the QD feels. The degree of polarization depends on the contrast between the inside and outside refractive indices. We examine the solvent dependence of the extinction coefficient and observe that it is independent of solvent refractive index within the error of the measurement. We show that accounting for the effect of the capping layer reduces sensitivity of the absorption cross-section to the medium. However the absorption cross-section is still less sensitive to the dielectric constant of the medium than predicted from simple theory.

3.2 Experimental

CdSe colloidal QDs were prepared following the methods pioneered by Murray *et. al.* [13] QD radii are quoted from calibration curves based on the same authors TEM and small angle X-ray scattering work. The extinction coefficient as a function of size was determined as follows: A known number of moles of precursers (n_{Cd}) are used to prepare the QDs with dimethyl cadmium being the limiting reagent. A small fraction of QDs is isolated from the original known volume of growth solution. The typical size dispersion in this fractionated sample ~ 5%. Assuming 100% reaction yield, the concentration of particles is equal to the concentration of cadmium divided by the number of cadmium atoms per particle. Explicitly,

$$N_{Cd/QD} = \frac{4}{3}\pi a^3 \frac{2}{V_{unit}} \qquad (3.1)$$

where a is the radius of the QD and V_{unit} is the volume of the unit cell containing 2 CdSe units. The bulk CdSe wurtzite unit cell volume is 112 Å^3. Powder X-ray diffraction studies of CdSe QDs found less than 0.5% lattice contraction compared to the bulk parameters.[13]

The integrated area of the absorption spectra of the growth and fractionated solutions are compared to obtain the relative concentration of QDs. We will further examine the validity of this procedure below. For now, the concentration of CdSe QDs in the size selected fraction is given by,

$$[QD] = \frac{\int_{350}^{700} A_{cut}(\lambda)d\lambda}{\int_{350}^{700} A_{growth}(\lambda)d\lambda} \frac{n_{Cd}Y}{V_{growth}} \frac{1}{N_{Cd/QD}} \qquad (3.2)$$

where $A(\lambda)$ is the absorbance as a function wavelength, Y is the reaction yield, and V_{growth} is the volume of the growth solution. Dilute dispersions are used for optical measurements; typically both the growth and fraction spectra are obtained 100X dilute. Once the concentration of QDs is known, the extinction coefficient can be calculated from Beer's law $\varepsilon_\lambda = A_\lambda / cl$, where c is the concentration of chromophores (M) and l is the path length (cm). Finally, for some measurements it is more convenient to use the absorption cross-section given in cm^2 by,

$$C_{abs} = \frac{2303\varepsilon_\lambda}{N_A} \qquad (3.3)$$

where N_A is Avogadro's number.

All absorption spectra are obtained using a HP-UV-Vis Spectrometer with 1 nm resolution in a 1 cm path length quartz cell. For measurements of the absorption cross-

section as a function of solvent refractive index, a concentration series of well washed dispersions of QDs is prepared in 5 different solvents. Identical volumes of a concentrated dispersion of QDs in hexane are added to the new solvent (approximately 0.1% hexane by volume in the final solution) and from the slope of the optical density versus concentration plot, the extinction coefficient in each solvent is deduced. All dispersions were optically clear and non-scattering.

3.3 Results

Figure 3.1, shows the C_{abs} at 350 nm *per particle* as a function of QD radius determined by the above procedure. Also shown is a similar determination where instead of integrating the growth and fractionated solutions, one simply takes the ratio of the optical density at 350 nm to determine the relative concentration. These two methods give the same result within our uncertainty. C_{abs} grows proportional to a^3 as one would expect from the increased number of CdSe units in the dispersion for the same concentration of QDs. The details of the model used to fit the data will be discussed in the next section. The largest deviation from the a^3 fit is for small sizes where the reaction yield is known to be less than 100%. Table 3.1 shows the estimated reaction yield based on thermal gravimetric analysis.

There are two major sources of uncertainty in this determination of the extinction coefficient. The first and most important is the sizing of the QDs. The uncertainty in the radius (~ 5%) of the particles leads to a minimum 15% uncertainty in the determined

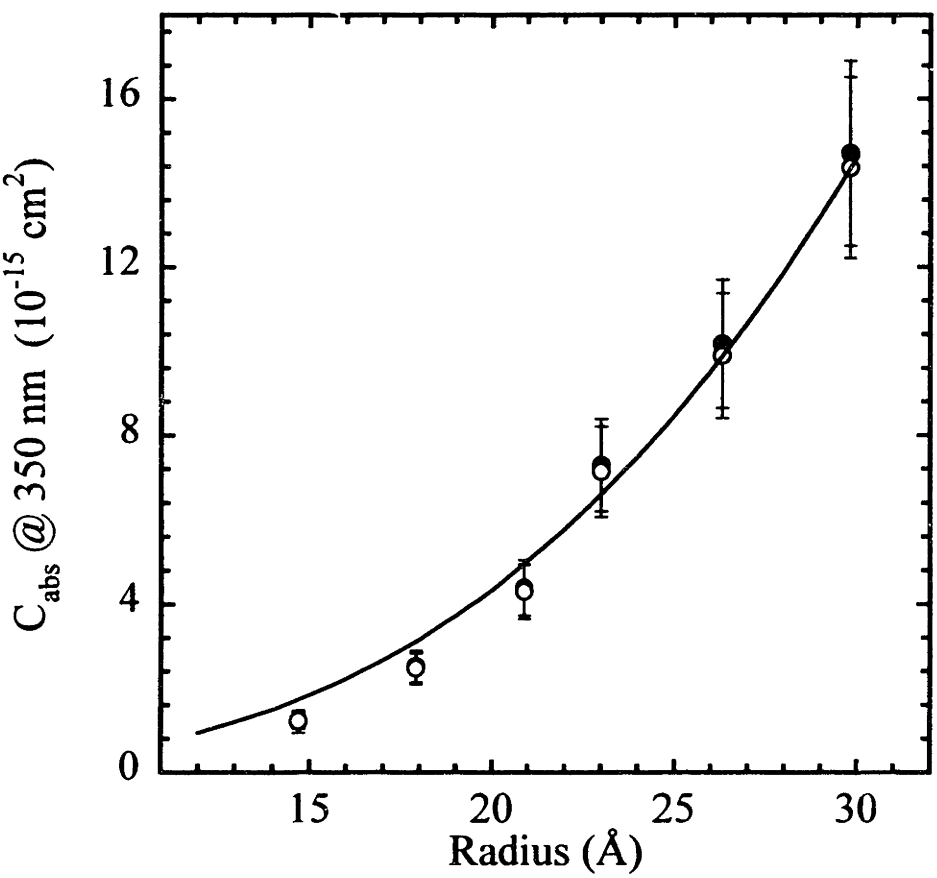

Figure 3.1 Observed and theoretical absorption cross-section as a function of size for CdSe QDs dispersed in hexane. Solid symbols indicate C_{abs} based on the integrated absorption spectra. Open symbols indicate C_{abs} determined using the absorbance of the growth and fractionated solutions at 350 nm.

Table 3.1: Estimated reaction yield based on thermal gravimetric analysis. (F.V. Mikulec, unpublished results).

Lambda $1S_e1S_{3/2h}$	Radius (Å)	% wt. Loss 25-600 C	Total yield (g)	Inorganic yield (g)	% Yield
498	13.9	23.9%	0.46	0.35	65.8%
526	16.8	18.5%	0.57	0.46	87.2%
600	25.9	12.0%	0.58	0.51	95.9%

extinction coefficient. Note that for size distributions greater than 20%, uncertainty in the radius weights the average volume towards larger sizes. Secondly, less than 100% reaction yield leads to lower than expected QD concentrations and thus under estimation of the extinction coefficient. For example, the extinction coefficient of the smallest particles ($a < 14$ Å) may be underestimated by as much as a factor of two. The volumetric measurements contribute at most 2% uncertainty to the final result.

Figure 3.2 shows linear absorption spectra for a size series of QDs. Each absorption spectrum has been divided by the extinction coefficient per particle (determined by the data in Fig 3.1) and by the QD volume to give the effective absorption cross-section *per CdSe unit*. This figure shows very clearly how the oscillator strength of the $1S_e1S_{3/2h}$ transition increases as the QD radius is decreased. In addition, the spectra for different sizes begin to converge for wavelengths less than 400 nm. In the inset of Figure 3.2 we plot the oscillator strength from 350 to 750 nm for each size per CdSe unit. Over this limited energy range, the total oscillator strength per CdSe unit is not conserved. This observation would seem to invalidate equation (3.2). Fortunately, the total oscillator

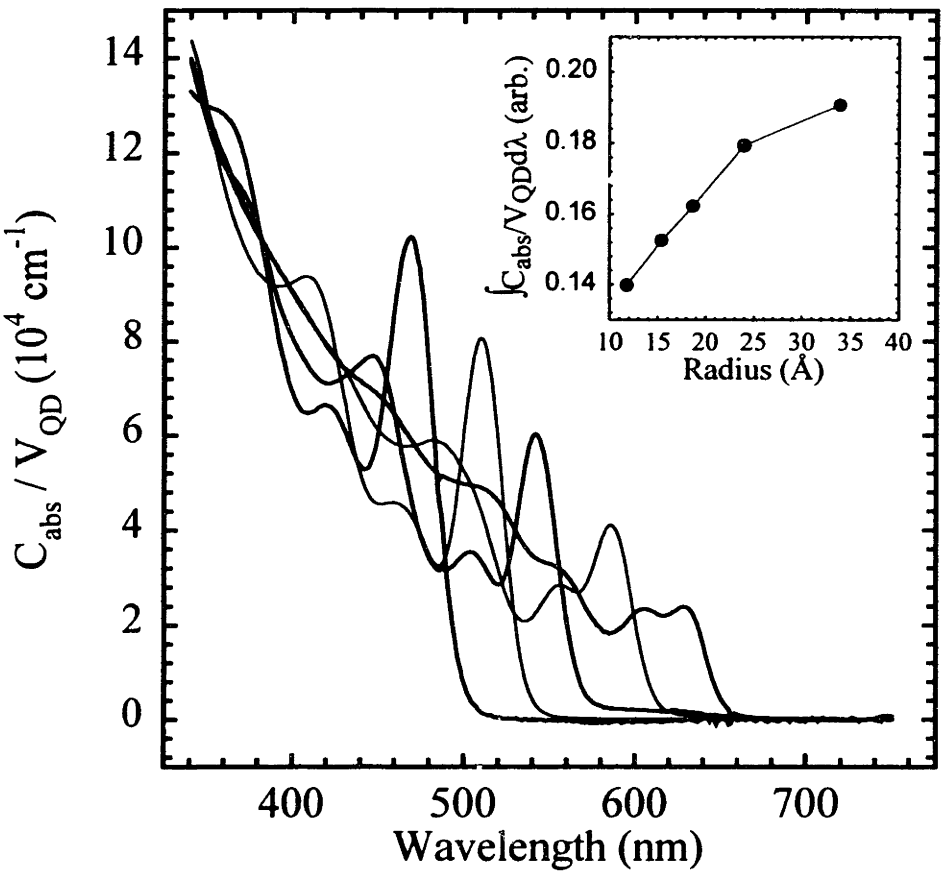

Figure 3.2 Room temperature absorption cross-section as a function of wavelength for CdSe QDs dispersed in hexane. Each spectrum is divided by the volume of the QD to give the absorption cross-section per CdSe unit. The inset shows the integrated area per unit volume as a function of the QD radius.

strength over this wavelength range varies relatively slowly with size. Thus, as long as the average QD radii in the growth and size selected fractions are not significantly different, comparison of the total area of under the absorption curve gives a good estimation of the relative concentrations.

In Figure 3.3 we examine the dependence of the absorption cross-section on the solvent refractive index for various features in the linear spectrum. First, a concentration series of QDs in a particular solvent is prepared (Fig. 3.3A). We then plot absorbance vs. concentration for the wavelengths indicated (Fig. 3.3B). The absorbance increases linearly with concentration indicating that Beer's law is valid in this concentration range. The deduced extinction coefficient relative to that of the same dispersion in hexane is plotted vs. solvent refractive index (Fig 3.3C). Within error, no difference in the extinction coefficient as a function of solvent refractive index (m_3) is observed either for transitions high in the band or for transitions near the band edge. Experiments where the absorption spectra were measured as a function of concentration of capping ligand present in the solution showed no change within the instrumental reproducibility.

3.4 Discussion

3.4.1 Dilute dispersions

For optical transitions far from any strong resonances and far from the band edge where the density of states may be approximated as a continuum, it is reasonable to model the extinction coefficient using the formalisms from light scattering of small particles.[14] Formally, the extinction cross-section is the sum of the absorption and scattering cross-sections.

$$C_{ex} = C_{abs} + C_{scat} \tag{3.4}$$

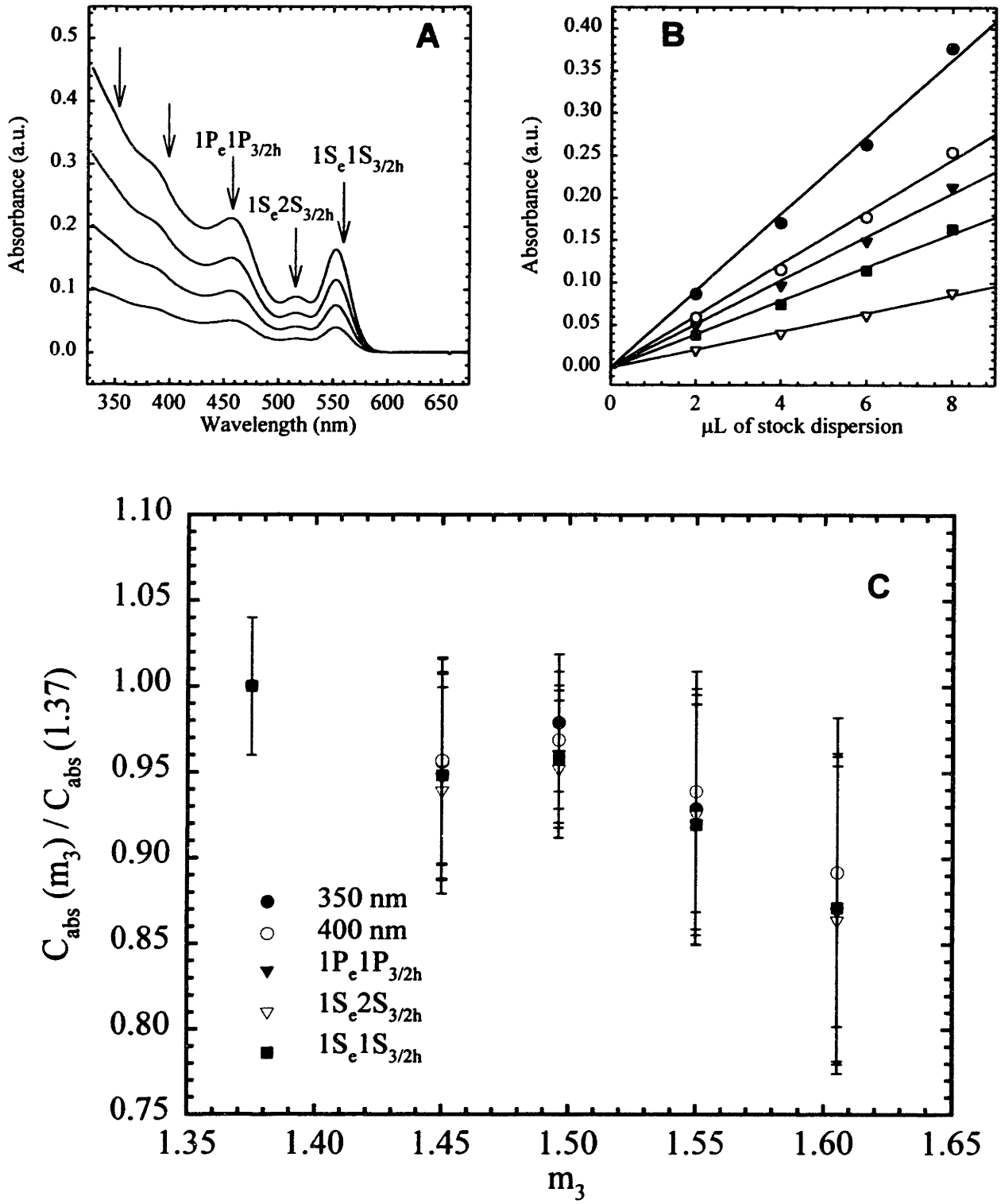

Figure 3.3: Measurement of the absorption cross-section as a function of solvent refractive index. Figure 3.3A shows representive spectra with increasing QD concentration. In Figure 3.3B, the absorbance as a function of concentration at the indicated points is plotted. In Fig. 3.3C, the slope of the Beer's law plot, relative to that of the same QDs is hexane, is plotted. Error bars indicate the uncertainty in the measurement based on multiple runs.

Light as it propagates through the medium a distance l is reduced in intensity by $e^{-C_{abs}Nl}$. For particles where the radius (a) is much less than λ/m_3, the absorption cross-section is much greater than the scattering cross-section. Dispersions of colloidal QDs are optically clear by eye and the measured scattering is less than 0.1% of the incident light. For absorbing particles with isotropic polarizability,

$$C_{abs} = 4\pi k \,\mathrm{Re}(i\alpha) = \frac{8\pi^2 m_3}{\lambda}\mathrm{Re}(i\alpha) \tag{3.5}$$

where m_3 is the refractive index of the medium, λ is the wavelength in vacuum, and α is the polarizability of the particle. The polarizability of dielectric spheres with radius a is given by,

$$\alpha = \frac{m_1^{\,2} - m_3^{\,2}}{m_1^{\,2} + 2m_3^{\,2}} a^3 \tag{3.6}$$

where $m_1=n_1-ik_1$ is the complex refractive index of the particle. An alternative expression which is useful for further calculations and identically equal to Equation (3.5-3.6) when the volume fraction of particles is much less than one was derived by Ricard *et al.*[8]

$$C_{abs} = \frac{\omega}{m_3 c}|f(\omega)|^2 2n_1 k_1\left(\frac{4}{3}\pi a^3\right)$$
$$f(\omega) = \frac{3m_3^{\,2}}{m_1^{\,2} + 2m_3^{\,2}} \tag{7a,b}$$

Written in this manner, the C_{abs} is proportional to the "bulk" absorption coefficient ($2n_1k_1$), times a local field factor. The local field factor is equal to the ratio of the applied electric field to the electric field inside the sphere, which of course is related to the polarizability of the sphere.

The theoretical curve in Figure 3.1 is the calculated C_{abs} based on equations (3.7 a,b) for CdSe QDs in hexane. Only literature values for the complex refractive index of bulk CdSe,[15,16] and the radius of the QDs, determined from previously TEM and SAXS measurements, were used in the calculation. The fit is remarkably good given that for small sizes the dielectric constant is probably significantly different from the bulk values.[17]

While the agreement between theory and experiment is excellent for QDs in hexane, equation (3.7) shows that the polarizability of the particle depends on the contrast between the refractive indices of the medium and the particle. However, in Figure 3.3 we observed that the extinction coefficient did not depend on the solvent refractive index. In chapter 2, accounting for the screening provided by the capping ligands appeared to explain the relative insensitivity of the polarization energy to the external dielectric environment. To apply the same principle to the problem of the absorption cross-section we need the polarizability of a sphere covered with a concentric shell of a different material. The solution is straightforward and no doubt has been solved by others: for a core-shell structure embedded in a dielectric medium in a uniform electric field where,

$\varepsilon = \varepsilon_1(\omega)$ for $0<r<a$

$\varepsilon = \varepsilon_2$ for $a<r<b$

$\varepsilon = \varepsilon_3$ for $r>b$

$$f(\omega) = \frac{-9\varepsilon_3\varepsilon_2 b^3}{2a^3(\varepsilon_2 - \varepsilon_1(\omega))(\varepsilon_2 - \varepsilon_3) - b^3(\varepsilon_1(\omega) + 2\varepsilon_2)(\varepsilon_2 + 2\varepsilon_3)} \qquad (3.8)$$

Equation (3.8) reduces to (3.7b) for a=b or $\varepsilon_1=\varepsilon_2$. (in each case ε is approximated by m^2)

In Figure 3.4A we plot the theoretical C_{abs} as a function of the solvent refractive index and cap thickness assuming $\varepsilon_2 = 2.1$. Even a thin 10Å shell layer with dielectric

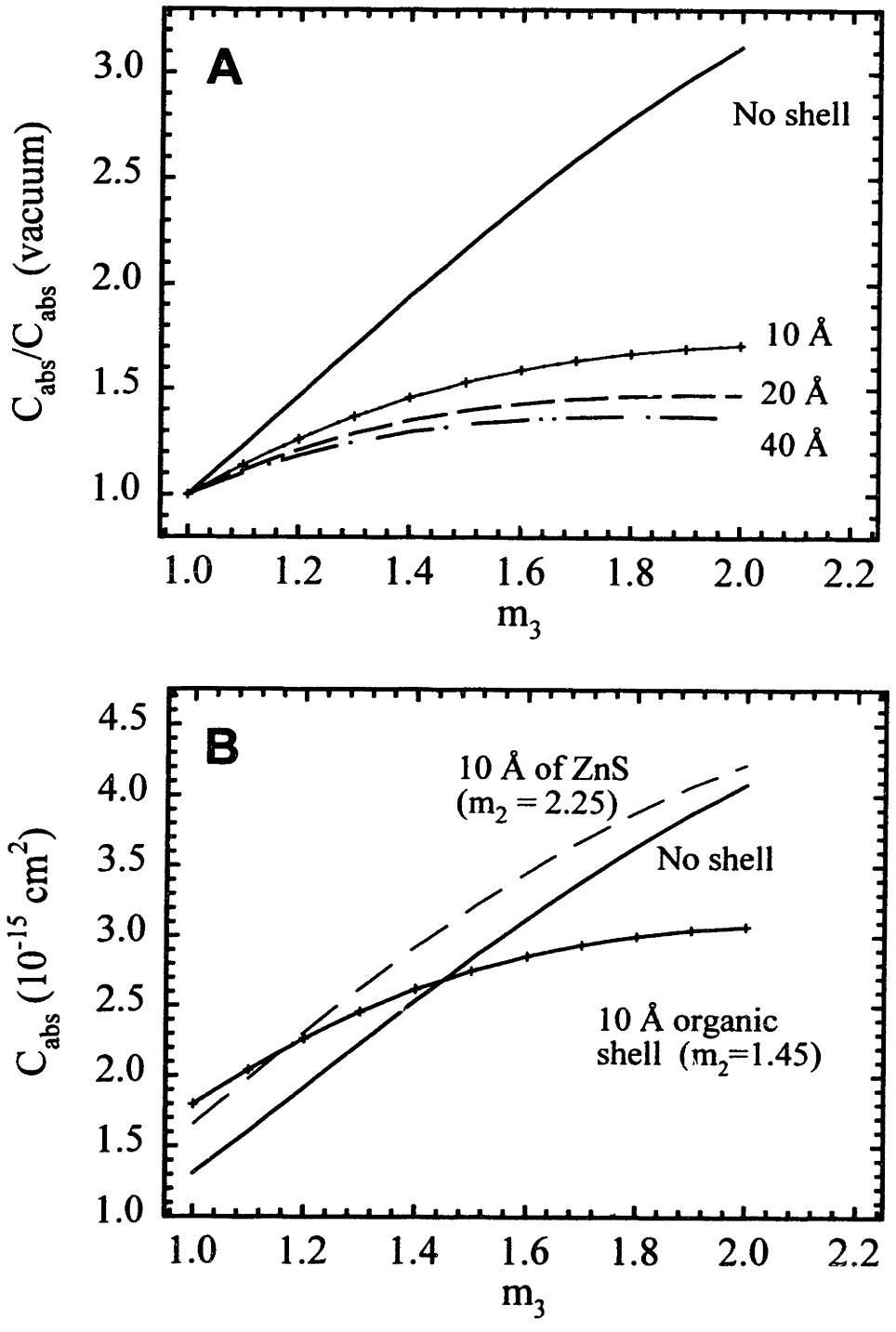

Figure 3.4: (A) Relative absorption cross-section vs. solvent refractive index for CdSe with organic shells of different thicknesses with respect to QDs in hexane. (B) Comparison of the theoretical absolute absorption cross-section for bare CdSe QDs, QDs with a 10 Å organic shell, and with a 10 Å ZnS shell.

constant close to that of the solvent, has a potent effect on C_{abs}, reducing the effect of changing the medium by almost 1/3. Further increases in the shell thickness reduce the sensitivity even further. For a given solvent, increasing the excluded volume around the QD may increase or decrease the absolute absorption cross-section depending on the dielectric constant of the shell layer compared to the dielectric constant of the medium (Figure 4B). We also show the theoretical effect of a ZnS shell. For ZnS overcoated CdSe QDs in organic media, the primary effect of the shell is to increase the effective volume of the particle. This in turn increases the polarizability and thus C_{abs} for the particle. Qualitatively, the inorganic core-organic shell model seems to explain the insensitivity of C_{abs} with regard to the solvent refractive index. However, to reduce the sensitivity over our range of accessible solvents to within the error (10%) requires a shell thickness of nearly 20 Å, much greater than we found in Chapter 2 (~ 8 Å).

It may be that we cannot quantitatively compare the theoretical fits in Fig 3.4 to the data in Fig 3.3 because of the absorption band that begins for 3-iodotoluene and 3-bromotoluene below 375 nm. Near a resonance, anomalous dispersion is generally observed and the complex value of the solvent refractive index should be used in the theoretical calculations. Only the real part of m_3 was used; this may explain why the data at 350 nm in Figure 3.3C shows the opposite trend to the theory line. However, near the QD band edge, the refractive index of the solvent is purely real and should be close to the literature value used in the calculations. QD absorption cross-section measured at the band edge shows the slight downward trend with increasing solvent refractive index as is observed in the near-UV. At the band edge, the polarizability of the QD clearly cannot be modeled using bulk CdSe parameters

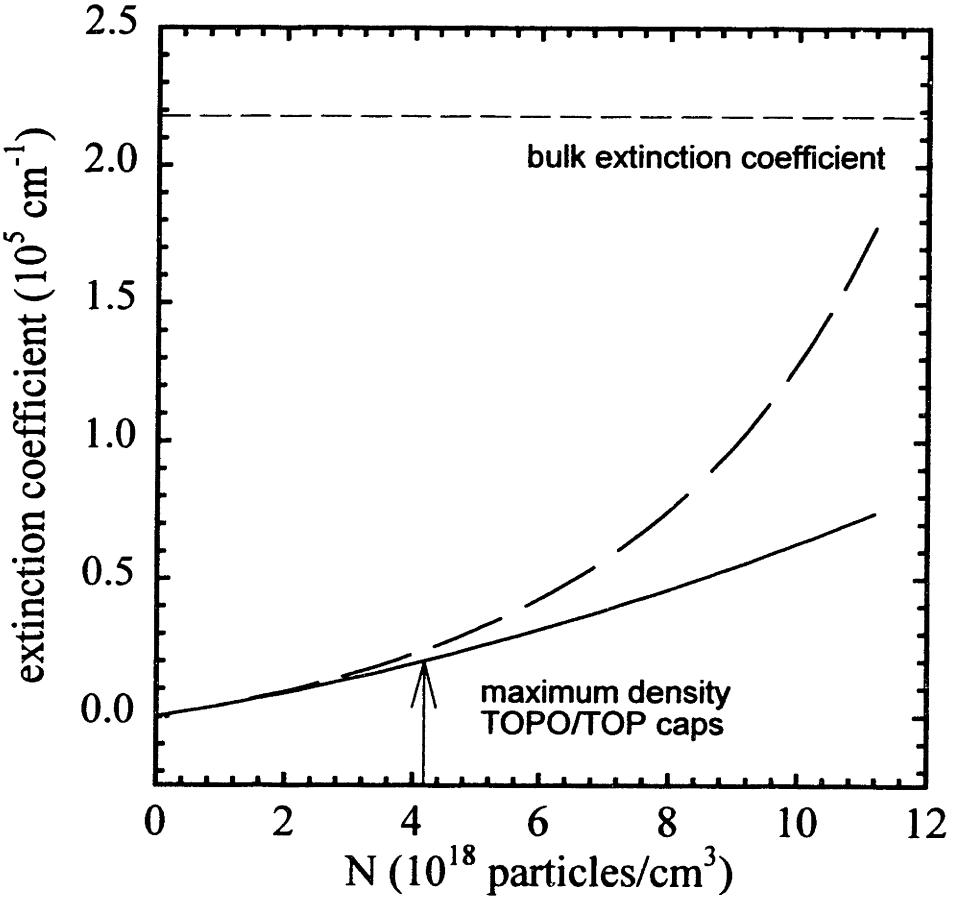

Figure 3.5 Comparison of the theoretical extinction coefficient (cm^{-1}) using the scattering formalism (solid lines) and the Lorentz-Lorenz expression (dashed lines) as a function of particle concentration. The calculations are for a dispersion of 25 Å CdSe QDs and $h\nu = 3.1$ eV. The arrow indicates the maximum packing density of QDs capped with TOPO/TOP ligands. The theoretical lines terminate at the density corresponding to closest packing of unpassivated 25 Å hard spheres (i.e. no capping ligands)

and the effect of the discrete electronic states must be taken into account. Here more detailed models of the local field should be investigated.[8]

3.4.2 Concentrated dispersions

A condition for applying the scattering formulae is that the mutual distances of the particles are large compared to the size of the particles and large compared to the wavelength of light in the medium.* When this condition is satisfied, the effective refractive index of the medium ($\tilde{m}$) is given by,

$$\tilde{m} = 1 - i2\pi N k^{-3} S(0) \qquad (3.9)$$

where N is the number of particles per unit volume, S(0) is the scattering function for the particles and k is the propagation constant of the electromagnetic wave. For homogeneous spheres with isotropic polarizability, S(0) is given by

$$S(0) = ik^3\alpha^3 + \frac{2}{3}k^6\alpha^2 \qquad (3.10)$$

and α is given by equation 3.6. On the other hand, it is also possible to treat QDs like large molecules and use the Lorentz-Lorenz formula from molecular optics:

$$\frac{\tilde{m}^2 - 1}{\tilde{m}^2 + 2} = \frac{4}{3}\pi\alpha N \qquad (3.11)$$

In this case it is assumed that the mutual distances of the particles are small compared to the wavelength of light (a still << λ) and the electric field to which a particle is exposed is due to the scattered fields of large number of other molecules on all sides.[14] For a dilute of dispersion of 20 Å QDs in hexane with concentration ~2×10^{-7} M (A = 0.2 @ 350 nm) the average distance between particles (r) is ~ 200 nm. Therefore r/λ is

* For simplicity in the discussion that follows we assume that the particles are suspended in a medium with refractive index equal to 1.

approximately ~1 and formally neither the conditions for the molecular optics regime nor the scattering regime are satisfied.

In Figure 3.5 the ratio of the extinction coefficient determined from the theoretical effective refractive index in these two different regimes is plotted versus the concentration of particles. Equations 3.9 and 3.11 yield nearly identical results through the dilute dispersion regime for small nanometer size particles. However, as the particle concentration approaches that of close-packed QDs significant deviations are observed. Equation 3.11 deviates from the linear dependence on concentration and approaches the bulk extinction coefficient.

3.5 Conclusions

Excellent agreement between the measured and theoretical absorption cross-section for interband transitions far above the band edge for QDs in hexane is observed. The absorption cross-section appears to be insensitive to the refractive index of the medium for common organic solvents. However, caution should be exercised when using these results for QDs dispersed in media with dielectric constants that differ greatly from that of the capping ligand until the issue of the screening from the ligand shell can be addressed. In addition, the simple theory suggests that significant deviations from Beer's law will be observed at particle concentrations approaching those of close-packed films. It should be possible to measure the deviation using highly concentrated dispersions in an ultra-thin quartz cell ($l < 0.5$ mm).

3.6 Acknowledgements

The data used to calculate the absorption cross-section as a function of QD size was provided by WK. Woo. The thermal gravimetric analysis data was compiled from the unpublished results of F. V. Mikulec. The author would like to thank V. Klimov for stimulating this investigation in this first place and Sasha Efros for useful discussions.

3.7 References

[1]L. Brus, "Quantum Crystallites and Nonlinear Optics," Appl. Phys. A-Mater. Sci. Process. **53** (6), 465-474 (1991).

[2]T. Vossmeyer, L. Katsikas, M. Giersig *et al.*, "CdS Nanoclusters: Synthesis, Characterization, Size Dependent Oscillator Strength, Temperature Shift of the Excitonic Transition Energy, and Reversible Absorbance Shift," J. Phys. Chem. **98** (31), 7665-7673 (1994).

[3]M. Shim and P. Guyot-Sionnest, "Permanent dipole moment and charges in colloidal semiconductor quantum dots," J. Chem. Phys. **111** (15), 6955-6964 (1999).

[4]M. Jacobsohn and U. Banin, "Size dependence of Second Harmonic Generation in CdSe Nanocrystal Quantum Dots," J. Phys. Chem. B **104** (1), 1-5 (2000).

[5]A.L. Efros and A.L. Efros, "Interband absorption of light in a semiconductor sphere," Soviet Physics of Semiconductors **16** (7), 772-775 (1982).

[6]Y. Kayanuma, "Quantum-size effects of interacting electrons and holes in semiconductor microcrystals with spherical shape," Phys. Rev. B **38** (15), 9797-9805 (1988).

[7]A.L. Efros, "Optical Properties of Semiconductor Nanocrystals with Degenerate Valence Band," Superlattices Microstruct. **11** (2), 167-169 (1992).

[8]D. Ricard, M. Ghanassi, and M.C. Schanne-Klein, "Dielectric confinement and the linear and nonlinear optical properties of semiconductor-doped glasses," Optics Communications **108**, 311-318 (1994).

[9]O. Keller and T. Garm, "Retarded electromagnetic response of a spherical quantum dot: A self-consistent field calculation," Phys. Rev. B **52** (27), 4670-4673 (1995).

[10]O. Keller, "Local fields in the electodynamics of mesoscopic media," Physics Reports-Review Section of Physics Letters **268** (2-3), 85-262 (1996).

[11]G. Todorovic, V. Milanovic, Z. Ikonic *et al.*, "Influence of the Self-Consistent Potential on Absorption Cross Section in Semiconductor Quantum Dot," Solid State Phenomena **61-62**, 235-238 (1998).

[12]M. Iwamatsu, "Image-Charge and Excitonic Effects on the Oscillator Strength of Silicon Quantum Dots," Japanese Journal of Applied Physics **37** (10), 5620-5621 (1998).

[13]C.B. Murray, D.J. Norris, and M.G. Bawendi, "Synthesis and Characterization of Nearly Monodisperse CdSe (E = S, Se, Te) Semiconductor Nanocrystallites," J. Amer. Chem. Soc. **115** (19), 8706-8715 (1993).

[14]H.C.v.d. Hulst, *Light Scattering by Small Particles*, 2nd ed. (Dover, New York, 1981).

[15]E.D. Palik, "Handbook of Optical Constants II," (Academic Press, Boston, 1991), Vol. 2.

[16]S. Ninomiya and S. Adachi, "Optical properties of cubic and hexagonal CdSe," J. Appl. Phys. **78** (7), 4681-4689 (1995).
[17]L. Wang and A. Zunger, "Pseudopotential calculations of nanoscale CdSe quantum dots," Phys. Rev. B **53** (15), 9579-9582 (1996).

Chapter 4

Steady State Photoconductivity of CdSe Quantum Dot Solids*

4.1 Introduction

Two and three dimensional arrays of quantum dots (QDs) are of interest both as model "artificial solids" with potentially tunable optical and electronic properties[1] and as materials for possible applications in memory[2] and computation.[3-5] Colloidal nanocrystals are promising "building blocks" for fabricating such materials as these "artificial atoms" readily assemble into both glassy and crystalline close-packed solids. Semiconductor QDs also have potential uses in a variety of opto-electronic devices including light emitting diodes [6-8], photodetectors [9,10], photovoltaic cells, [11,12] and possibly laser diodes.

A basic understanding of how charges are captured by and escape from a charge neutral QD, as well as the process of charge separation of a photogenerated excitation created within a QD, is essential for the rational design of these opto-electronic devices. Photoconductivity is a valuable tool to probe charge separation, charge trapping, and carrier recombination mechanisms in materials. In this chapter, we present steady state photoconductivity on close-packed glassy solids of colloidal CdSe QDs. In Sec. 4.3, the dependence of the photoconductivity on temperature, applied electric field, excitation energy, intensity, QD radius, inter-particle separation, and surface passivation is briefly presented. In Section 4.4 we discuss these results in detail and show that photoconductivity in QD solids is consistent with electric field ionization of photoexcited, quantum confined electron-hole pairs. Similar to photoconductivity in many

* Much of this chapter has appeared in print (C.A. Leatherdale *et al.* Phys. Rev. B, **62**, 2669, 2000)

other molecular-like systems, the charge generation efficiency depends on the rate of charge separation relative to the rate of geminate recombination of the photoexcited electron-hole pair. In Sec. 4.4.6, a simple resonant tunneling model is presented to describe the probability of electron-hole pair separation as a function of applied electric field. We show that the energy required for charge separation in QD solids is much greater than kT at room temperature. Thus, although most of the experiments described in this chapter are performed at 10 K, the results are applicable to room temperature operation of the photovoltaic devices and light emitting diodes currently under study.

4.2 Experiment

4.2.1 Sample Preparation

Glassy colloidal CdSe QD solids are prepared as described in Chapter 1. Tri-butylphosphine (TBP)/tri-butylphosphine oxide (TBPO), pyridine, and octanethiol capped QDs are prepared by repeated dispersion and flocculation of the QDs from a neat solution of the new capping group, followed by washing to remove the excess cap once the exchange is complete. Typically ~ 50 mg of well-washed QDs is dried to a powder on the vacuum line, approximately 0.5 mL of the new capping ligand is added, and the dispersion is then allowed to stir overnight at ~ 60 °C under inert atmosphere. Complete cap exchange is indicated by a change in the solubility of the QDs. Overcoating of bare CdSe QDs with ZnS or CdS is performed using previously described methods. [13,14]

Close-packed solids are drop cast from solution on to lithographically patterned sapphire or silicon substrates (described below). In order to minimize the exposure of the sample to air, all electrical contacts are made *prior* to film deposition. For this report, a 9:1 hexane/octane

solution is used for casting glassy films of TOPO/TOP, TBPO/TBP, and octanethiol capped dots. Pyridine capped dots are deposited from a 9:1 methanol and pyridine mixture on Si/SiO_2 substrates that are boiled in ultra-pure water and then dried at 175 °C to make the oxide surface more hydrophilic.[15] Scanning electron microscopy reveals that cracks form in the QD solid if it is not allowed to dry sufficiently before exposure to vacuum. In films deposited and allowed to dry in inert atmosphere overnight before testing, the degree of cracking is reduced but the qualitative electrical behavior and photoconductive gain is the same as that measured for films tested immediately after deposition. All samples exhibit band edge photoluminescence (typically 10% quantum yield in the growth solution at room temperature) and minimal deep trap photoluminescence (PL). QD radii and inter-particle spacing are quoted from published small angle X-ray scattering and transmission electron microscopy measurements. [16,17] QD radii in all cases include the surface layer.

Polished sapphire optical flats or degenerately doped silicon substrates with either a 600 nm or 350 nm thermally grown gate oxide, are used as substrates for photoconductivity measurements. Gold bar electrodes (200 x 800 x 0.1 μm^3) with separations varying from 1 to 20 μm are patterned on the substrates using standard photolithographic techniques. Following the patterning process, the substrates are cleaned by O_2 plasma ash to reduce organic surface contamination before deposition of the QD solid.

4.2.2 Photoconductivity Measurements

All measurements are performed under vacuum in a cold finger cryostat. Typically, DC photoconductivity of the QD solid is recorded while varying the applied field in steps of 10^4 V/cm with a 10 to 30 second delay after each step to allow the current to settle. A Keithley 6517

electrometer is used to apply a bias voltage and measure current. The excitation source for the photoconductivity experiments is an Argon ion laser with typical excitation intensity of ~ 2.5 mW/cm^2. For measurement of the spectral dependence of the photocurrent, a SPEX Fluorolog-2 spectrofluorometer with a 450W Hg-Xe arc lamp in combination with a 0.22 m double monochromator is used as the excitation source (intensity ~ 1 mW/cm^2). The energy dependence of the lamp intensity is accounted for by measuring the emission from a reference cell containing a concentrated dye solution (Rhodamine 610 or 640). The spectral response is further corrected by excitation correction factors created for each of the dyes to account for the ~10% error resulting from the difference in optical path from the positions of the reference dye cell and the sample.

Multiple electrode separations are tested (from 1 to 20 μm); the results depend only on the applied field for samples of different electrode separation, thus eliminating the contacts as a significant source of the circuit resistance. Several experiments are performed to compare the I-V curve when both the active sample area and gold electrodes are illuminated to the I-V curve when only the active sample area is illuminated. Since there are no qualitative differences in the I-V characteristics that might indicate photoinjection from the electrodes, for all subsequent experiments the entire electrode pattern is illuminated. Intensity dependent measurements are acquired in non-sequential order using a neutral density wheel to modify the laser intensity.

4.2.3 Optical Measurements

To develop a complete picture of the charge generation process, the photoconductivity results are correlated with the PL quantum yield and the PL lifetime. To measure the

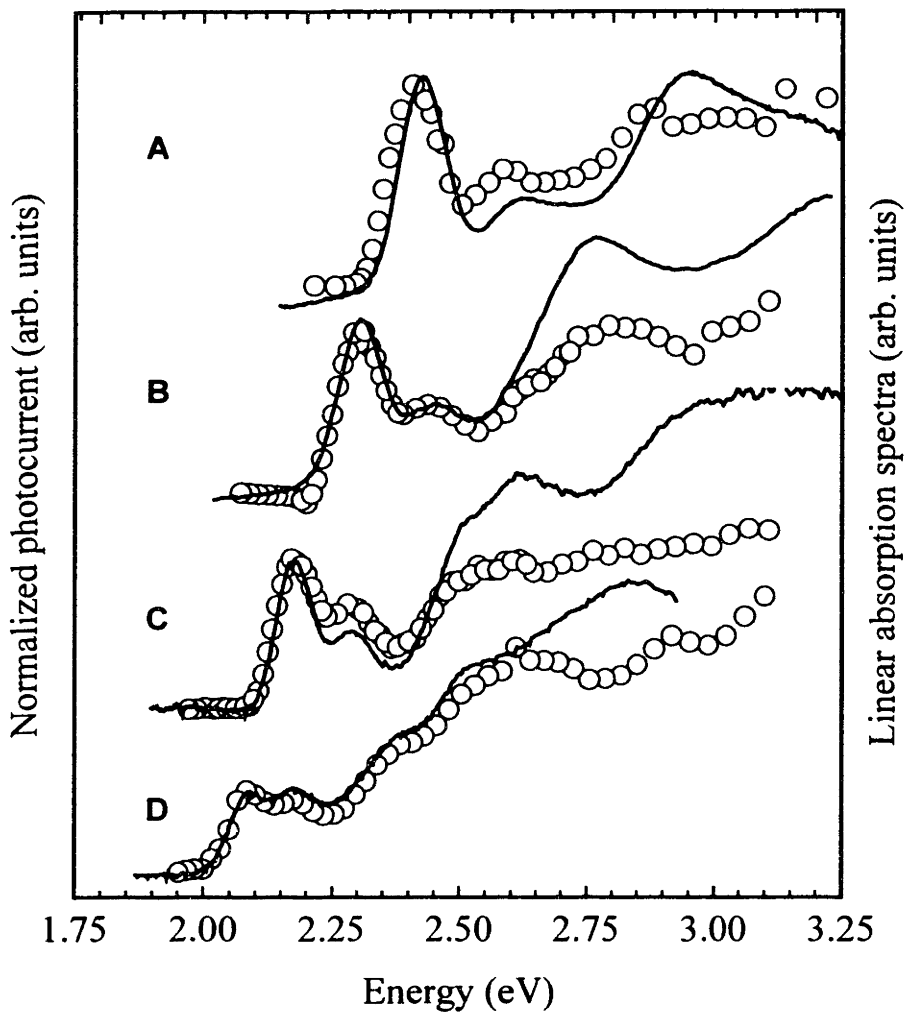

Figure 4.1 Spectral dependence of photocurrent at 10 K. The symbols indicate the photocurrent at a fixed applied electric field of 2.5 x 10^5 V/cm, normalized for excitation intensity. The solid line is the corresponding linear absorption spectrum for each sample. The photocurrent spectral response is scaled to match the first absorption feature. The QDs in each sample have the following radii: **A** – 17.5 Å, **B** – 20.6 Å, **C** - 25 Å, and **D** -30 Å.

temperature dependence of the PL quantum yield (QY), linear absorption and PL spectra for the films are measured using a 300W Hg-Xe lamp, SPEX 0.33 m monochromator, and an optical multi-channel analyzer. The PL is excited as before with a low intensity laser beam or with a Hg-Xe lamp plus monochromator combination. A mode locked Nd:YAG/dye laser system and a time correlated single photon counting apparatus with ~150 ps time resolution is used for PL lifetime measurements.

4.3 Results

Figure 4.1 shows the photocurrent spectral response for a representative series of QD sizes. For each sample, the spectral response is scaled to match the lowest energy feature in the linear absorption spectrum. The well resolved, discrete electronic transitions in the absorption spectra demonstrate the monodispersity of the QD samples. The shape of the photocurrent spectral response follows the linear absorption spectrum, independent of applied field and temperature ($T < 150$ K). No photocurrent is observed for excitation below the band edge suggesting that optical excitation of charges directly out of sub-bandgap trap states makes a negligible contribution to the photocurrent. The spectral response of the QD solid is clear evidence that free carriers originate from quantum confined electron-hole pairs created within individual QDs. [18,19]

While there is close correspondence between the absorption spectrum and the photocurrent spectral response near the band edge, the spectral response slowly deviates from the absorption spectrum as the excitation energy is increased above the band edge. A similar trend has been previously observed in photoluminescence excitation studies on dilute ensembles of CdSe QDs and is consistent with an increase in the non-radiative recombination rate of the

exciton at higher energy excitation. Since excitation with energies well above the band edge does not enhance the charge generation efficiency (number of charges/absorbed photon), charge separation must be a slower process than intra-band relaxation to the lowest excited state. This result is not surprising given the fast intra-band relaxation times (< 300 fs) reported for colloidal semiconductor QDs.[20]

Figure 4.2 shows that the photocurrent varies linearly with excitation intensity. Linear dependence is observed over two orders of magnitude in intensity, independent of electrode spacing, temperature, applied electric field and excitation energy.[18] The photoconductive gain, even at high fields, is only on the order of 10^{-4} charges/photon. The dark current is approximately two orders of magnitude smaller than the photocurrent and lies below the noise level for the measurement apparatus (< 0.1 pA). High sensitivity, dark current measurements will be discussed in a forthcoming publication.[21] In this work, the total current I is equal to the photocurrent I_{ph}.

The absolute magnitude of the photocurrent decreases with increasing temperature (Figure 4.3A). However, the shape of the I-V characteristic is nearly independent of temperature. Figure 4.3B shows the same I-V curves as in Fig. 4.3A, each multiplied by a scaling factor so that they collapse on to a single universal curve, $\mathcal{F}(F)$ where F is the applied field. Remarkably, there is virtually no change in the shape of the I-V characteristics from 10 to 300 K. Figure 4.3B is one of the best examples of a universal I-V curve that we have observed. For other samples, the shape of the I-V characteristic is weakly temperature dependent and the curvature of the I-V characteristic decreases slightly with increasing temperature (Figure 4.3C).

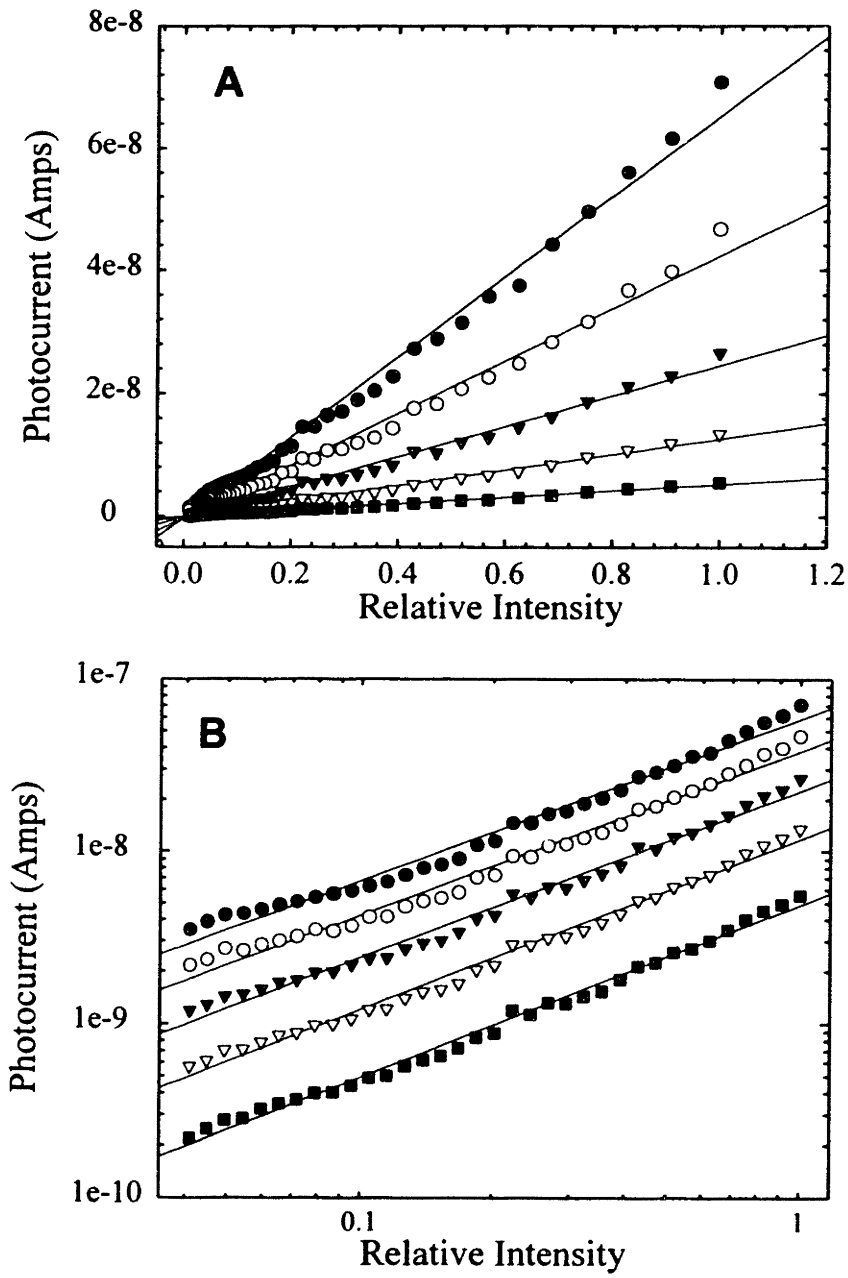

Figure 4.2: **(A)** Intensity dependence of the photocurrent at 10 K for a 21 Å radius QD solid. Symbols are the photocurrent at an applied field of (●) 250 kV/cm, (▽) 200 kV/cm, (■) 150 kV/cm, (◇) 100 kV/cm and (▲)50 kV/cm. **(B)** Same data as in A but plotted on a log-log scale.

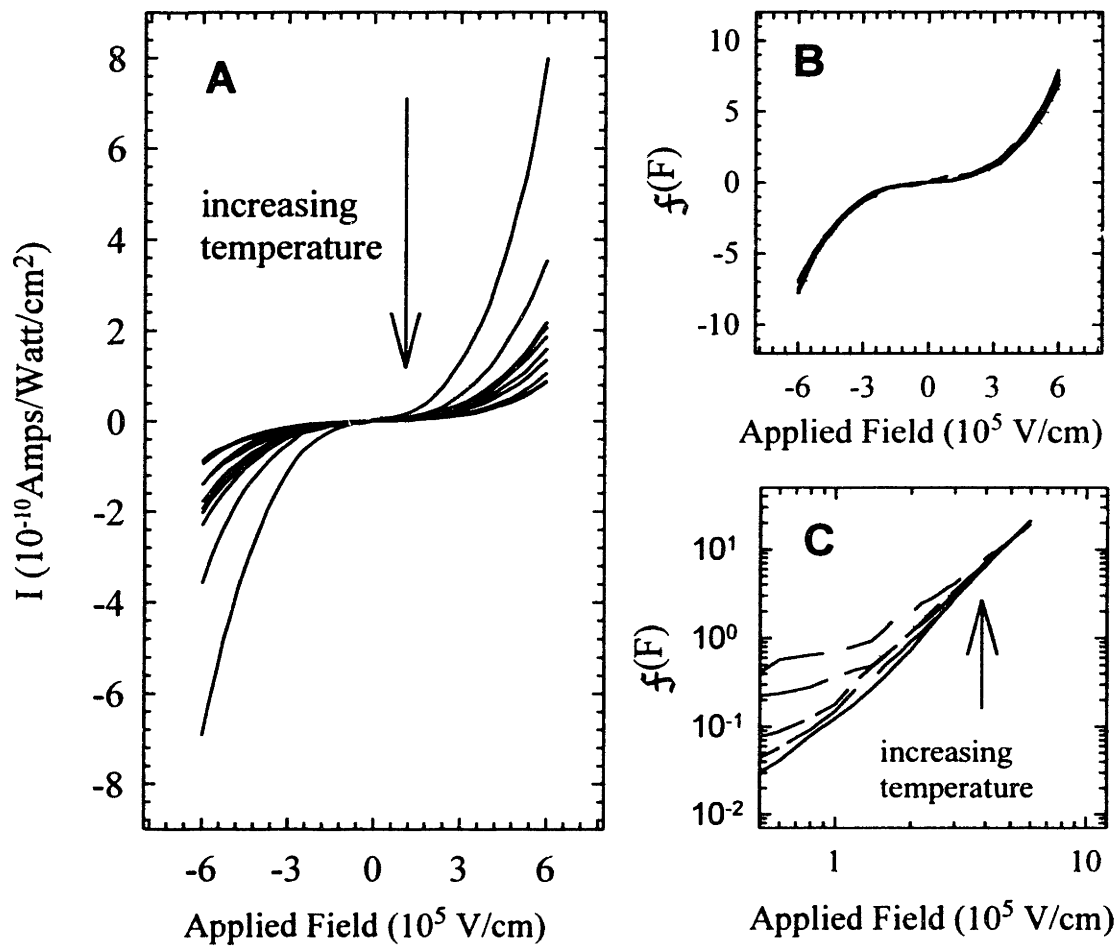

Figure 4.3 A: Temperature dependence of the photocurrent for a 19 Å TBPO/TBP capped QD solid. I-V curves are shown for 10, 25, 50, 75, 100, 150, 200, 250,and 293 Kelvin. **B:** The I-V curves from **A** are each multiplied by a scale factor, S(T), to show that they collapse on to a single universal curve, $\mathcal{F}$(F). **C:** The I-V curves for a 18.5 Å TOPO/TOP capped QD solid at 10, 50, 75, 100, 125, and 300 Kelvin (note this is a different sample than the data in **A** and **B**). Each curve has been multiplied by a scale factor to give the best fit to a single universal curve.

No systematic trends with QD size or surface ligands have been identified that determine whether the shape of the I-V characteristic is temperature dependent.

To examine the contribution of the exciton lifetime to the temperature dependence of the photocurrent, the factor 1/S(T) used to scale the I-V curves in Fig. 4.3B, the QY, and the exciton lifetime (τ) are plotted relative to their respective values at 10 K (Fig. 4.4). The exciton lifetime, $\tau = 1/(k_r+k_{nr})$ where k_r and k_{nr} are the radiative and non-radiative relaxation rates, is measured for a close-packed film of the same size QDs as used for the photocurrent measurements. Both QY(T) and τ fall sharply with increasing temperature, consistent with an increase in the non-radiative rate.

The shape of the I-V characteristic depends on QD size. Figure 4.5 shows I-V curves for a series of QD sizes and constant inter-particle spacing (TOPO/TOP ligands). As the QD radius decreases, the curvature of the I-V curve increases slightly. In order to account for small variations in optical density and excitation intensity and to better examine changes in the shape of the I-V characteristics, each I-V curve is scaled by a constant factor so that the high field photocurrent is the same for all. Within the signal to noise, the photocurrent rises smoothly with increasing applied electric field, without any inflection points that could indicate the onset of saturation or a clear onset of the photocurrent. No systematic trend in the photoconductive gain as a function of QD size is observed.

The I-V characteristics depend more strongly on inter-particle spacing than surface ligand functionality. Figure 4.6 shows I-V curves where the size of the QD is kept constant and the surface ligand is systematically varied. Exchanging the TOPO linkage (8 carbon chains) (◆) to an octanethiol linkage (O) does not affect the I-V characteristics significantly. Changing

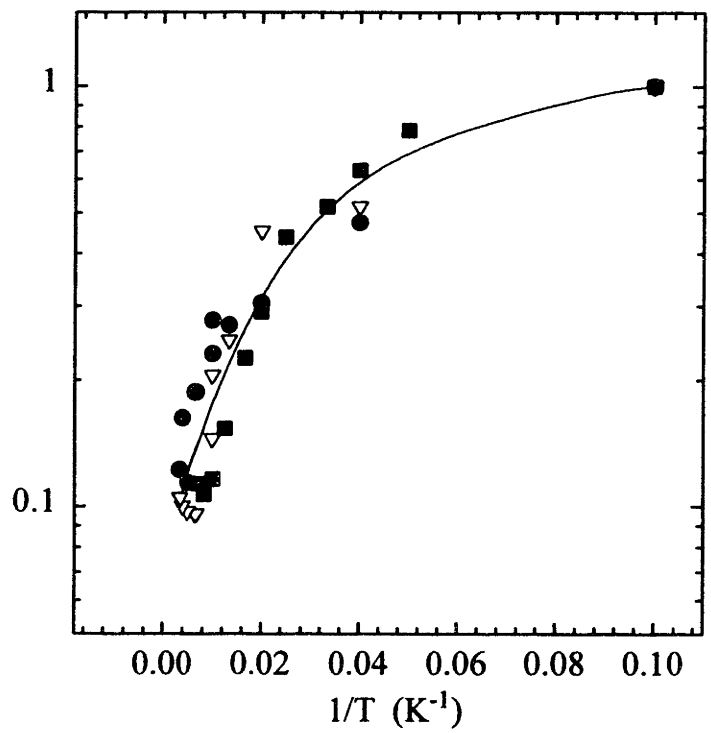

Figure 4.4: Temperature dependence of the scale factor (1/S(T)) (▽) from the data in Fig. 4.3A compared to the temperature dependence of the PL lifetime (●) and the exciton lifetime (■), relative to their values at 10 K. Lifetime and QY data is for an 18.2 Å TOPO/TOP capped QD solid.

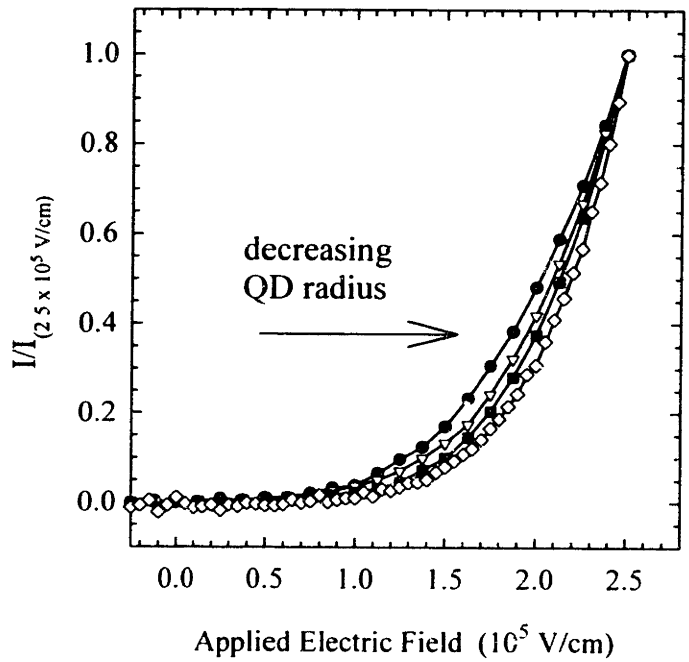

Figure 4.5 Current versus applied electric field for QDs with radii(R) as follows: (●) 25 Å (▽) 20.6 Å (■) 19 Å (◇) 17.5 Å. Samples are TOPO/TOP capped QDs with edge to edge spacing (d) ~ 11 Å. Measurements at 10 Kelvin. See text for description of the normalization.

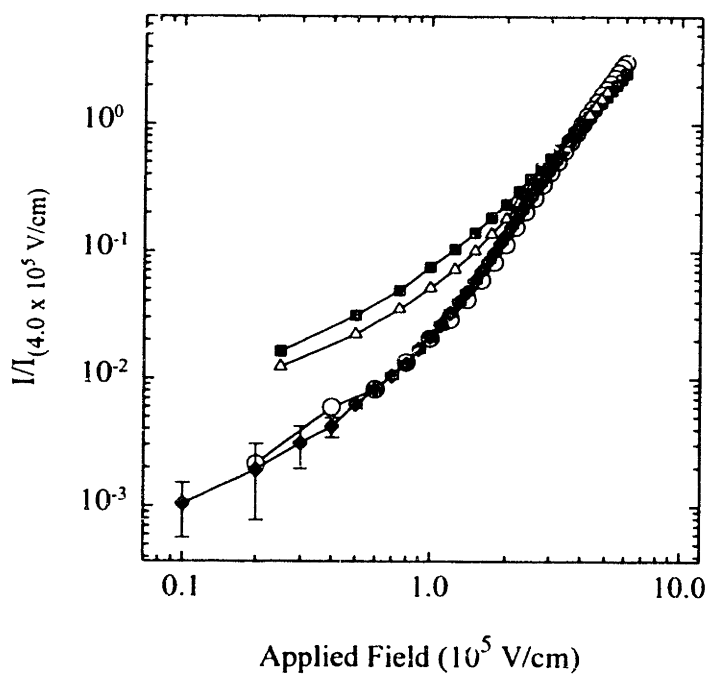

Figure 4.6 Effect of the surface ligand on I-V curve shape at 10 K for 20±1 Å QDs with (◆) TOPO/TOP (△) TBPO/TBP, (O) octanethiol, and (■) pyridine ligands. Error bars indicate the approximate variance in the relative positions of each curve based on multiple I-V sweeps and multiple samples. Note data is normalized to one at 400 kV/cm.

to a conjugated ligand while keeping the inter-particle spacing constant (pyridine (■) vs. TBPO (△)) also does not affect the I-V characteristics significantly. It is clear that QDs passivated with shorter ligands (pyridine and TBPO/TBP) have larger photoconductance at low fields than QDs passivated with longer chain ligands (TOPO and octanethiol). The results for overcoated QD solids also show the effect of increasing edge-to-edge separation of the CdSe cores. Overcoated samples consist of a CdSe core, with a shell of a second, larger band gap semiconductor. Table 4.1 shows that core-shell QDs have higher PL QY than bare QDs, but the overcoated QD solids are less photoconductive.

The trends described in this section are reproducible and have been repeated with several different sample series. The absolute magnitude of the photocurrent, however, may vary by as much as a factor of two for the same nominal sample preparation. Variations in sample thickness and degree of excess cap, as well as the macroscopic defect density in the films may contribute to this variability. The organic ligands themselves are highly insulating at cryogenic

Table 4.1: Summary of the measured external charge generation efficiencies (10 K), and PL quantum efficiencies for 20 Å QD solid of various surface passivations and inter-particle spacings. The PL quantum efficiencies are measured on dilute dispersions in hexane of the same QDs used to make the close-packed films.

Surface Passivation	CdSe edge spacing (Å)	PL QY(%)	Charges per photon @ 250 kV/cm
TOPO/TOP	11 ± 1	2	8E-5
Octanethiol	9 ± 2	0.85	5.9E-5
TBPO/TBP	7 ± 1	1	1.4E-5
Pyridine	7 ± 1	~ 0.01	8.3E-6
3 monolayers CdS +TOPO/TOP	~ 31	24	< 5E-6
3 monolayers ZnS + pyridine	~ 26	7	< 5E-8

temperatures. Near room temperature, highly thermally activated conduction ($E_a \sim 0.6$ eV) is observed for a film of pure TOPO ($\rho \sim 2 \times 10^{-3}$ Ohms cm^{-1}). The conductance of TOPO is negligible below 250 K.

4.4 Discussion

4.4.1 Theoretical Overview

The increase in conductivity ($\Delta\sigma$) of a material under steady state illumination is generally given by,

$$\Delta\sigma = e(\Delta n\mu_n + \Delta p\mu_p). \qquad (4.1)$$

where Δn and Δp are the densities of photogenerated electrons and holes respectively and μ_n and μ_p are the respective mobilities. Both the density of free carriers and the mobility may depend on the applied electric field. In insulators, conducting polymers[22], molecular solids[23] and other low mobility materials, the density of free carriers is often strongly field dependent and limited by the rate of geminate recombination of the photoexcited electron-hole pairs. In systems where the rate of intra-band relaxation is much faster than the rate of charge separation, the charge generation efficiency (number of free carriers/absorbed photon) depends on the branching ratio between the rate of geminate recombination and the rate of charge separation, as:[24]

$$\eta(F,T) = \frac{k_F(F,T)}{k_F(F,T) + k_r(T) + k_{nr}(T)} \qquad (4.2)$$

In equation (4.2), geminate recombination is expressed as the sum of k_r and k_{nr} (assumed to be weakly field dependent), k_F is the rate of charge separation under the applied electric field, and T is the sample temperature. The field dependence in η originates from the rate of charge separation.

In sections 4.4.2 through 4.4.4 we show that for QD solids, the strong field dependence of the photocurrent, the correlation between the temperature dependence of the photocurrent and the exciton lifetime, and the size and surface passivation dependence are all consistent with the model described by equation (4.2). Throughout the discussion we assume that each QD is never more than singly charged because of the large Coulomb charging energy (measured to be at least ~150 meV for 4-5 nm diameter CdSe QDs above a conducting substrate).[25] In addition, since the absorption measurements of Chapter 2 showed that the electronic states of adjacent QDs are uncoupled, we assume that charge carriers must tunnel or hop from site to site.

4.4.2 Temperature Dependence

When limited by geminate recombination, the yield of carriers is strongly affected by the exciton lifetime. If the rate of geminate recombination is much greater than the rate of charge separation, equation 4.2 can be factored so that $\eta(F, T) = \tau(T)k_F(F)$ where $\tau(T)$ is the exciton lifetime ($1/\tau = k_r + k_{nr}$). The I-V characteristics in Figure 4.3A are well described by the product of a field dependent function $\mathcal{F}(F)$ that gives the shape of the I-V characteristic (Figure 4.3B) and a temperature dependent function, S(T) that controls the amplitude of the I-V curve. Figure 4.4 shows that 1/S(T) is similar in shape to the temperature dependence of τ and the PL QY in the absence of an applied field. Similar QY (T) behavior has been observed in a number of TOPO/TOP capped samples making us confident that the similarity between 1/S(T) and the QY (T) is not merely fortunate coincidence. Both τ and the QY decrease with increasing temperature consistent with an increase in the non-radiative recombination rate within the parent QD.*

* The lowest energy exciton state in CdSe QDs is optically dark (See ref. ?). In principle, thermal population of a nearby optically bright state should increase the radiative rate with increasing temperature. However the similar behavior of the QY and τ suggests that the non-radiative rate dominates the temperature dependence.

If we tentatively assign 1/S(T) to the exciton lifetime, then the shape of the I-V characteristic must be related to the field dependent charge separation rate. In Figure 4.3B, $\mathcal{f}(F)$ is nearly temperature independent suggesting that charge separation proceeds via tunneling through the large barriers that confine the electron and hole to the QD. The binding energy of the quantum-confined exciton (~ 200 meV for a 20 Å QD) is also much greater than the available thermal energy at room temperature. Thus, one would not expect thermal assisted ionization of excitons to contribute significantly to the photocurrent.

A large number of samples show I-V characteristics that are well described by $\mathcal{f}(F)\tau(T)$ and are consistent with tunneling between QDs. In a few cases, however, the shape of the I-V characteristic is weakly temperature dependent and the photocurrent at low applied fields increases slightly with increasing temperature (see Figure 4.3C). If k_F is comparable to the exciton recombination rate ($k_r + k_{nr}$) then it is not possible to factor the expression for η, and a weakly temperature dependent I-V characteristic might be observed. However, the carrier yield should also be substantially increased compared to that for samples like the one in Figure 4.3A and 4.3B, leading to larger photocurrents. This is not observed. Similarly, if the mobility of free carriers was thermally activated, increased photocurrent would be expected. No correlation between the magnitude of the photocurrent and the temperature dependent behavior has been found for different samples, ruling out both these possibilities.

Weak temperature dependence without an increase in charge generation efficiency could be explained by thermal population of various QD surface defect states. In CdSe QDs, the deep trap PL (believed to be surface related) has been observed to increase between 10 K and ~ 80 K before rapidly decreasing again.[26] We show evidence in Chapter 5 that charge separation of

surface trapped carriers occurs at lower energy than separation of carriers confined to the core of the QD. Thermal population of surface defect states may increase the number of charges that escape from the QD via this low energy pathway. At the same time, defect states may also act as centers for non-radiative exciton recombination. Thus, the net yield of carriers may not be increased even though charge separation may be possible at lower applied fields.

4.4.3 Intensity Dependence

The intensity dependence of the photocurrent provides information about both the photocarrier generation mechanism and the recombination mechanisms for free carriers. Figure 4.2 shows that the photocurrent in the QD solid varies linearly with intensity consistent with a single photon mechanism for electron-hole pair generation and dissociation. Linear intensity further implies that either there is no recombination in the bulk of the sample, or that recombination is first order with respect to the concentration of free majority carriers (quasi-monomolecular recombination).

We eliminate the first possibility by considering the dependence of the absolute photocurrent on electrode spacing for fixed electric field and photon flux. If there is no carrier recombination in the bulk of the sample and the carrier mobility remains the same, then the total number of charge carriers between the electrodes should increase with increasing electrode spacing. Within our sample-to-sample reproducibility, we observe no dependence of the magnitude of the photocurrent on electrode spacing, for gaps between 1 and 20 μm, suggesting the photocurrent is not transit time limited.

In a trap-free insulator where the number of thermally generated carriers is much fewer than the number of photogenerated carriers, a square root dependence on intensity is expected

from bimolecular recombination of the photogenerated electrons and holes.[27] First-order recombination kinetics can predominate if there are many more recombination centers than there are *free* majority carriers.[27] Optical studies have suggested that there are deep hole traps and shallow electron traps at the surface of colloidal QDs.[26] The deep hole traps could both limit hole mobility and act as recombination centers when filled. Shallow electron traps could limit the free electron concentration such that monomolecular recombination kinetics could predominate. While the properties of the QD solid are qualitatively consistent with this model, further measurements of the photoresponse time as a function of excitation intensity and temperature are required to confirm the presence and chemical nature of traps in the QD solid.

4.4.4 Field Dependence

The maximum potential dropped across two adjacent QDs in any of the experiments is only ~ 0.25 eV—much less the potential that confines the electron and hole to the QD. Thus, we argue that the primary action of the electric field is to overcome the Coulomb attraction of the initial electron-hole pair and not to significantly lower the confinement barrier. By applying an electric field, an unoccupied state is brought into resonance with the QD containing the exciton so that one of the charges can tunnel out. Figure 4.5 shows that the curvature of the I-V characteristic increases with decreasing QD radius, consistent with an increase in the energy required to overcome the binding energy of the photogenerated electron-hole pair.

The dependence of the photocurrent on surface passivation and inter-particle spacing (shown in Figure 4.6 and Table 4.1) suggest that these parameters affect the *rate* of charge separation. For example, the probability to tunnel through alkane ligands is proportional to $e^{-\alpha d}$ where $\alpha \sim 1$ Å^{-1} [28] Thus if the density of states remains the same on changing the surface ligand

from TOPO to TBPO, one would expect approximately a 42X increase in tunneling probability ($d_{TBPO} \sim 7$ Å, $d_{TOPO} \sim 11$ Å). In Figure 4.6, we observe an approximately 10X increase in tunneling probability at low fields A distribution of tunneling distances would make the tunneling probability less sensitive to the average inter-particle spacing than expected from the simple theory.

The carrier generation efficiencies for core-shell QDs are also in qualitative agreement with carriers tunneling out of the QDs For QDs overcoated with 3 monolayers of ZnS (~ 3.1 Å per monolayer, conduction band offset ~ 0.9 eV) and then capped with pyridine ligands (d~7 Å), we observe that the charge generation efficiency is at least 1000 X smaller than for bare TOPO capped QDs. For CdS overcoated QDs, where the CdS conduction band is nearly matched to the CdSe conduction band (offset ~ 0.2 eV), we observe that the charge generation efficiency is only 16X smaller than for bare TOPO capped QDs. The observations for the core-shell QDs are consistent with findings in polymer/QD composite LEDs where improved efficiencies were observed with CdS overcoated QDs[29] in comparison to ZnS overcoated particles [30]

4.4.5 Tunneling model for charge generation

4.4.5.1 Basic outline

Geminate recombination systems have customarily been treated using the formalism developed by Onsager[31] and extended by a number of others [24,32,33] In the simple Onsager model, the probability of geminate recombination depends on the Coulomb energy of the initially thermalized electron-hole pair compared to the strength of the applied electric field While this qualitative picture is applicable to QD solids, none of these Onsager-type models account for cases where the Coulomb energy of the initial ion pair is much greater than the available thermal

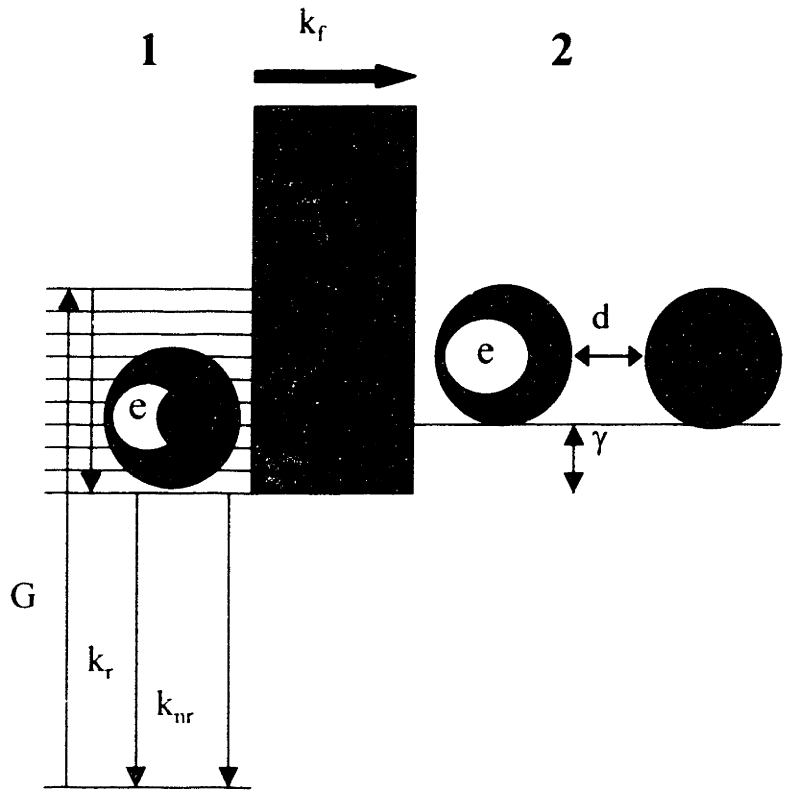

Figure 4.7: Cartoon of the energy cost required to separate the initial electron-hole pair. γ is the energy cost, "d" is the distance between adjacent QDs, and ϕ is the potential barrier which confines the electron or hole to the QD. ϕ is related to the energy difference between the lowest conduction(valence) band state for the electron(hole) and the LUMO(HOMO) for the organic capping layer. See text.

energy At 10 K, the binding energy of the confined exciton is much greater than kT; therefore within the Onsager model, the probability of charge escape is negligible except at extremely high fields To model the field response of the photocurrent, we develop a simple two-site resonant tunneling model to account for the essential physics in the initial separation of the exciton The calculations that follow provide intuition on how the shape of the I-V response should vary with changes in the experimental parameters

Figure 4 7 summarizes the tunneling model in a simple cartoon. A quantum-confined exciton is created with generation rate G by absorption of a photon with energy greater than the band gap. This exciton rapidly relaxes to the lowest excited state of the QD where it can undergo radiative recombination, non-radiative recombination, or ionization to create two adjacent, charged QDs The probability that one charge escapes depends on the height (ϕ) and width of the tunnel barrier (d) as well as the energy offset (γ) between the initial and final state. Increasing k_{nr} or k_r decreases the probability that one of the carriers escapes the parent QD. A two-site nearest neighbor tunneling model is sufficient to describe the essential physics because the inter-site spacing is almost 2 orders of magnitude larger than in molecular systems. As a result, the probability for a charge to tunnel or hop more than one site away from its initial site in a single step is negligible.

We consider two possible mechanisms for a charge escaping from the QD (Figure 4 8). In the first case that shall be referred to as "core-to-core", both the electron and hole are in spherically symmetric, "particle-in-a-sphere" states. One charge then tunnels directly into another spherically symmetric state in the adjacent QD. In the second case, referred to as "trap-to-trap", both charges are in trap states at the surface of the particle One charge then tunnels

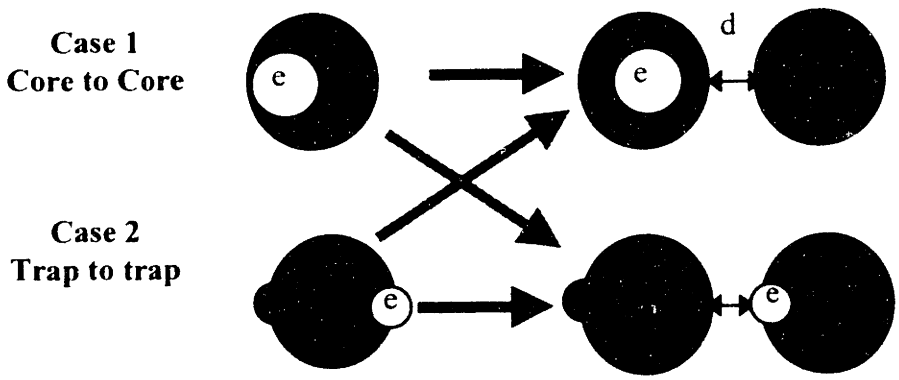

Figure 4.8: Cartoon of the possible mechanisms for charge separation in QD solids In case 1, charges tunnel directly between delocalized states. In case 2, the electron and hole are trapped on separate surface sites and one charge tunnels to the surface of an adjacent QD. Combinations of these mechanisms are also possible as indicated by the center arrows.

into a trap state at the surface of the adjacent QD. In both cases, the energy cost for charge separation arises from the energy required to overcome the Coulomb interaction of the photoexcited electron-hole pair and the interaction of each charge with its respective image charges. The details of how the net energy cost is calculated as well as calculation of the theoretical I-V curve are given in the next two sections. Readers uninterested in the theoretical details may skip ahead to section 4.4.5.3 to see how the tunneling model compares to experiment.

4.4.5.2 Calculation of the net energy cost

Generally, the energy cost for charge separation can be written as the difference between E_2 and E_1.

$$E_1 = E_c + J_{e,h}^{pol} + \Sigma_e^{pol} + \Sigma_h^{pol} \qquad (4.3a)$$

$$E_2 = E_{coul} + \Sigma_e^{pol'} + \Sigma_h^{pol'} \qquad (4.3b)$$

where E_c is the direct Coulomb interaction between the electron and hole, $J_{e,h}^{pol}$ is the polarization energy arising from the interaction between each carrier and the image charge of the other carrier, and the electron and hole self-charging energies are Σ_e^{pol} and Σ_h^{pol} respectively. E_1 is commonly known as the exciton binding energy. In E_2, the Coulomb interaction between charges in adjacent QDs (E_{coul}) is approximated by the interaction energy of two point charges in a medium of average dielectric constant ($\varepsilon_3 \sim 3\varepsilon_0$).* We neglect the interaction of each carrier with the image charge of the other carrier when the charges are in adjacent QDs.

* The average dielectric constant of the QD solid is calculated for randomly close-packed spheres (fill factor =0 64) of semiconductor with an organic shell of width (d) The interstices are filled with the same organic material $\varepsilon \sim 2\varepsilon_o$.

For the case of core-to-core tunneling, each charge is assumed to be in a spherically symmetric state and the energy cost ($\gamma=E_2-E_1$) can be derived using the results of Brus [34,35] and Babic[36]:

$$E_1 = \frac{-1.79q^2}{4\pi\varepsilon_0\varepsilon_1 a} + \frac{q^2}{4\pi\varepsilon_0 a}\left(\frac{1}{\varepsilon_1} - \frac{1}{\varepsilon_3}\right) + 2\frac{q^2}{8\pi\varepsilon_0\varepsilon_1 a}S_s \tag{4.4a}$$

$$E_2 = -\frac{-q^2}{4\pi\varepsilon_0\varepsilon_3(2a+d)} + 2\frac{q^2}{8\pi\varepsilon_0\varepsilon_1 a}S_s \tag{4.4b}$$

$$\text{where } S_s = 2\pi^2\sum_{l=0}^{\infty}\frac{(l+1)(\varepsilon_1-\varepsilon_3)}{(\varepsilon_3+l(\varepsilon_3+\varepsilon_1))}\int_0^1\left(\frac{\sin(\pi x)}{\pi x}\right)^2 x^{2l+2}dx$$

In equations (4.4), ε_1 is the bulk, high frequency dielectric constant for CdSe ($6.2\varepsilon_0$)[37] and "a" is the radius of the QD. It is assumed that the quantum confinement energy is the same in both E_1 and E_2 (valid within the strong confinement regime) as well as the self-charging energies for electron and hole. The latter approximation means that the self-charging energies will cancel in the expression for γ. The expression for E_2 is approximate and should be considered an upper bound only. A correct calculation of the interaction energy of two delocalized charge distributions at such short range requires a quantum mechanical calculation that is beyond the scope of this work.

For the case of trap-to-trap tunneling, the situation is somewhat simpler since the electron and hole can be treated as localized point charges. If trapped charges are localized on unpassivated Cd or Se atoms on opposite sides of the QD, the energy for charge separation is given using the results of Shim *et al.*[38]:

$$E_1 = \frac{-q^2}{8\pi\varepsilon_0\varepsilon_1 r} + \sum_{l=0}^{\infty}\frac{q^2}{2\pi\varepsilon_o\varepsilon_1}\frac{(\varepsilon-1)(2l+2)r^{4l+2}}{[(\varepsilon+1)(2l+1)+1]a^{4l+3}} \tag{4.5a}$$

$$E_2 = 2\sum_{l=0}^{\infty} \frac{q^2(\varepsilon-1)(l+1)}{8\pi\varepsilon_0\varepsilon_3(\varepsilon l+l+1)R}\left(\frac{r}{R}\right)^{2l} - \frac{q^2}{4\pi\varepsilon_0\varepsilon_3(2a+d)} \qquad (4.5b)$$

where is $\varepsilon = \varepsilon_1/\varepsilon_3$ and r is the radius of the semiconductor core including the surface, minus the ionic radius of the Se^{-2} ion (1.98 Å).* E_1 is the sum of the Coulomb interaction for two charges on opposite side of the QD plus the polarization energy for these two localized charges. E_2 is the self-charging energy for a singly charged dielectric sphere with a point charge near the surface[35] plus the Coulomb interaction with the point charge on the other sphere. γ in this case is a lower bound on the energy required for charge separation. If the static dielectric constants for the semiconductor and organic components are used (probably more appropriate for tunneling from localized states), the energy cost will be increased.

4.4.5.3 Calculation of escape probability

To fit the experimental I-V curves and extract an experimental value for γ, we model the transition rate between states 1 and 2 using a Golden Rule approximation. The three fitting parameters are the energy difference between the initial and final states (γ), the tunnel barrier height (ϕ) and a phenomenological parameter "w" that describes the amount of tailing of the density of states into the energy gap. Using the Golden Rule approximation, the transition rate (k) between two states can be written as the following:

$$k \propto \int_{-\infty}^{\infty} T(E)g_1(E)g_2(E)[F_1(E)-F_2(E)]dE \qquad (4.6)$$

* The charge is placed slightly inside the boundary of the dielectric sphere in order to avoid the interface where the potential is undefined. The trapped charge is assumed to be on an unpassivated Se site. r = core radius + 1.5 Å - Se^{-2} ionic radius. R = core radius + 1.5 Å

where *T(E)* is the transition probability through the barrier, *g(E)* is the density of states, and *F(E)* is the Fermi distribution function in state 1 or 2 respectively. Since all the experiments are at low temperature and low excitation intensity, equation (4.6) can be approximated by assuming that only state 1 is initially occupied and there is no thermal population of higher excited states. For simplicity, the back transition rate is assumed to be zero. The energy in the initial state is held fixed at zero for all applied biases and only the energy of the final states is allowed to vary. Equation (4.6) then simplifies to:

$$k(v) \propto T(0,V)g_2(-\gamma + qV) \tag{4.7}$$

where γ is the energy in the final state at zero applied bias, q is the elementary charge, and "v" the potential difference between the centers of adjacent QDs (the site to site potential). For plane waves incident on a barrier of width (d), the transmission probability is given by the following (WKB approximation):

$$|T(E)|^2 \approx \exp\left[-2\int_0^d \sqrt{\frac{2m}{\hbar^2}(\phi(x) - E)}dx\right] \tag{4.8}$$

We assume a square tunnel barrier of height ϕ_0. Applying a linear potential, the tunneling barrier is given by,

$$\phi(x) = \phi_0 - \frac{qV}{d}x \tag{4.9}$$

For high, narrow barriers, the transmission probability varies approximately linearly with applied voltage. For tunneling through organic ligands, we use "m" equal to the rest mass of the electron. The existence of a finite size distribution in the sample transforms the discrete density of states in the individual QDs into an effective continuum in the QD solid. We assume a continuum density of states of the form,

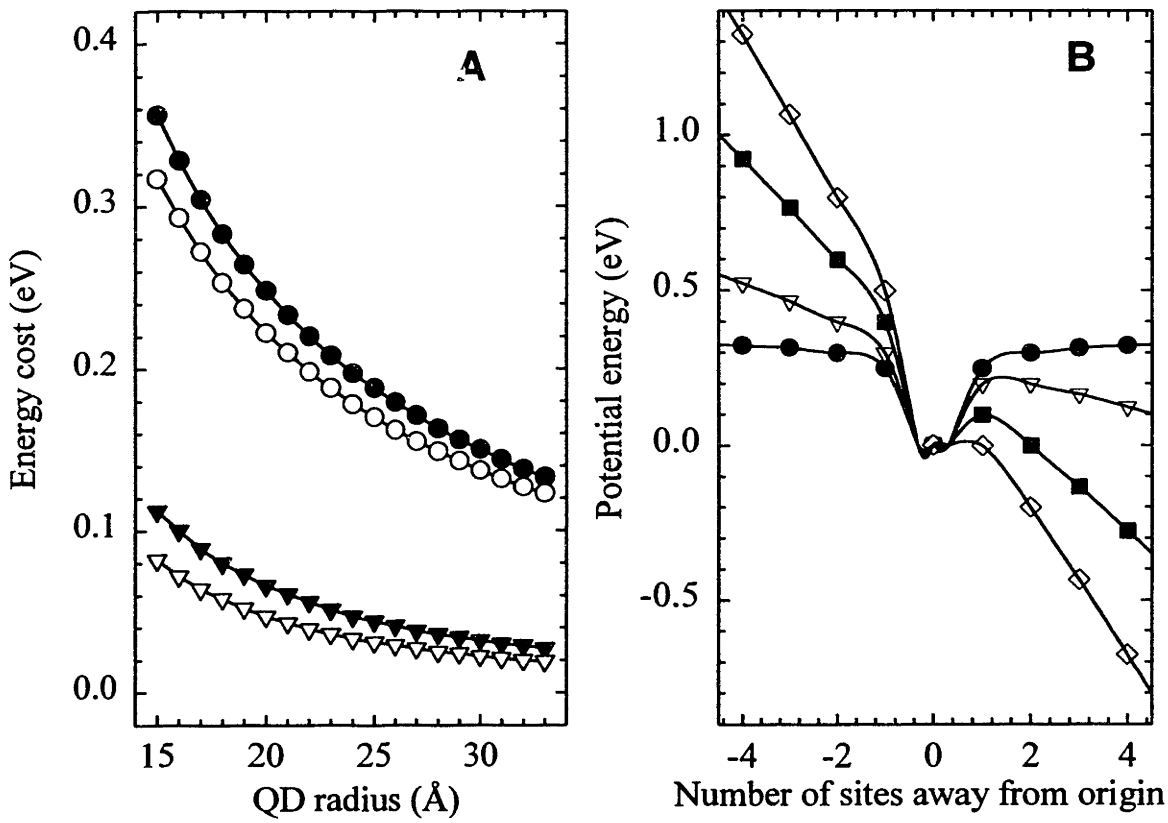

Figure 4.9: **(A)** Calculated energy cost to separate electron-hole pairs confined to the core (circles) and trapped on the surface (triangles) as a function of QD radius. Closed symbols are for 11 Å spacings and open circles are for 7 Å spacing. **(B)** Calculated potential energy, relative to the energy of the bound exciton, as a function of the number of sites between the electron and hole in a QD solid with 11 Å inter-particle spacing and 20 Å QDS. Symbols are for applied site to site potentials of 0 meV (●), 50 meV (▽), 150 meV(◇), and 250 (■) meV.

$$g_2(E) = \frac{1}{1+\exp\left(\frac{-E+\gamma}{w}\right)} \tag{4.10}$$

The parameter "w" controls the amount of "tailing" into the energy gap. Physically a large value for "w" means that there is a high density of trap states or a broad distribution of QD sizes and inter-particle spacings in the sample. This functional form for the density of states is only valid for applied fields less than γ; in the real system, the density of states should continue to increase with increasing energy. The final result used to fit the data is the following:

$$I(v) = \frac{\exp\left(\frac{-4\sqrt{2}\hbar^2 d}{3m(qv-\gamma)}\left(\left(\frac{m\phi}{\hbar^2}\right)^{3/2} - \left(\frac{m(\phi+\gamma-qv)}{\hbar^2}\right)^{3/2}\right)\right)}{1+\exp\left(-\frac{\gamma-qv}{w}\right)} \tag{4.11}$$

where v is the *site-to-site* potential.

4.4.5.4 Comparison to experiment

Figure 4.9A shows the net energy cost as a function of QD size and inter-particle spacing for core-to-core and trap-to-trap tunneling. Consistent with the data in Figures 4.5 and 4.6, the energy cost to ionize the exciton decreases with increasing QD size and decreasing inter-particle spacing. The model predicts that tunneling from traps is a much lower energy process than tunneling directly from core electronic states and that the size dependence is relatively weak. Figure 4.9B shows the potential energy as a function of applied field in terms of the number of sites away from the parent QD. Once sufficient field is applied that one charge can move one site away from the parent QD, the probability to move further away is much greater than the probability to move back and carriers are swept by the electric field through the solid. Figure

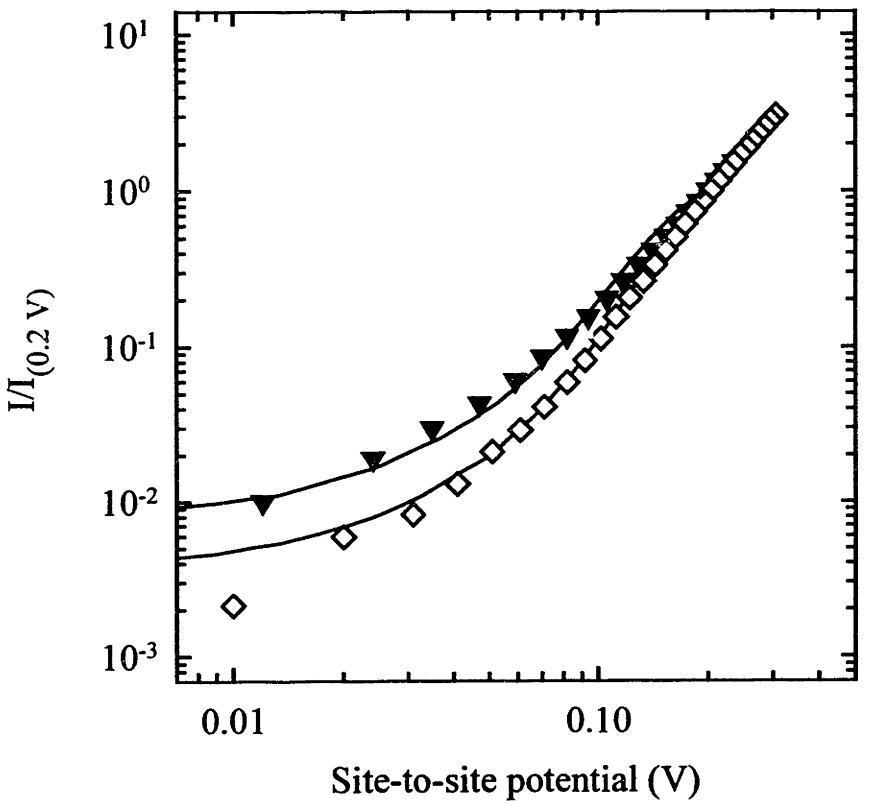

Figure 4.10 Comparison between the data (symbols) and the tunneling model (lines) at 10 K. Data is for 20 Å QDs with (◇) TOPO (d ~ 11 Å, $\gamma = 0.170$) and (▼) TBPO (d~7 Å, $\gamma = 0.150$) surface ligands. In the model, ϕ is fixed at 0.84 eV, and "*w*" is fixed at 0.060.

4.10 shows the calculated I-v curves based on this tunneling model for two different inter-particle separations. The data is scaled on to the site-to-site potential by dividing the applied voltage by the approximate number of QDs between the electrodes. This assumes that the potential is dropped uniformly across the sample. The width of the tunnel barrier is fixed at the measured edge-to-edge spacing between the QDs. The value of γ is allowed to vary but the ratio of the energy cost for TOPO vs. TBPO (1.14 to 1) is fixed at the approximate ratio calculated from equations (4.4a) and (4.4b). A single tailing parameter "*w*" and barrier height (0.84 eV) are chosen to best fit all the data. The barrier height is chosen to give the same change in transmission probability as a function of alkane chain length as has been reported for dark conductivity measurements on close-packed gold nanoparticles.[28] For the scaled data the goodness of fit is sensitive to "*w*" and γ but is relatively insensitive to the value of ϕ.

The model qualitatively reproduces the field dependence of the photocurrent. For the best fit, the values of γ are intermediate between the trap-to-trap and the core-to-core limits (~ 150 meV). The intermediate value for γ may suggest that both pathways are active in the QD solids. The slight sample-to-sample variation observed might be due to variations in the degree of surface passivation or oxidation that may shift the balance between core-to-core and trap-to-trap tunneling. Quantitatively, there are some problems with the model. For example, the escape rate (k_F) predicted from the fit parameters is much too large: If the attempt frequency for a charge to escape from the QD is approximately proportional to the orbital frequency (~10^{13} Hz)*, and the average transmission probability for a 0.84 eV barrier is ~10^{-4}, then for TOPO capped particles, this yields a value for k_F of 10^9 s^{-1}. Using equation (4.2) this implies efficiencies of

* Estimated based on the position/momentum uncertainty relation for a carrier confined to the QD. $f \geq \hbar/4ma^2$

nearly 100% (given 25 ns exciton lifetime at 10 K). This value is too high compared to what is observed. Better agreement with the observed photoconductive gain is found if the height of the tunnel barrier is increased. However, then the absolute value of the photocurrent is predicted to be much more sensitive to the inter-particle spacing (d) than is observed. Part of the difficulty may arise since the WKB model assumes a continuum of states above the barrier that is inappropriate for a molecular tunnel barrier. To compensate for the low density of states for the molecular tunnel barrier, the apparent barrier height may need to be smaller. Alternatively, the difficulty in producing a unique fit may arise from the complementary nature of the "a" and ϕ parameters. A large tunnel barrier height can be somewhat compensated for by increasing the "a" parameter to increase the density of available states at low energy.

Without an independent measure of either the density of states or the energy levels in the organic molecules with respect to the "conduction band" and "valence band" edges of the QD, more quantitative analysis is not possible. The primary utility of the model is to provide intuition on how the shape of the I-V curve should vary with changes in experimental parameters. For example, decreasing inter-particle spacing or increasing the QD size gives rise to I-V curves that are more linear and more photoconductive at low fields (see Figures 4.5 and 4.6). Reducing the number of intermediate trap states, for example by overcoating the QDs, should promote core-to-core tunneling, a pathway leading to highly nonlinear I-V curves and low photoconductivity except at high applied electric fields. Consistent with the model, Table 4.1 shows that very little photoconductivity is observed with the overcoated QDs compared to the non-overcoated samples. The model also predicts that ligands that act as shallow traps for one carrier and not the other promote initial charge separation of the exciton leading to higher

efficiency and weaker field dependence. Recent intra-band relaxation measurements suggest pyridine acts as a good hole acceptor [39,40] and would therefore promote the separation of electron-hole pairs and enhance the charge separation efficiency. Table 4.1 also shows that pyridine capped QDs have low PL efficiency but moderate photoconductivity compared to TOPO capped QDs. While pyridine may promote charge separation, the low PL QY of pyridine capped QDs suggests that this ligand also increases non-radiative recombination, thereby reducing the net carrier yield.

4.4.6 Final comments

Semiconductor QD solids present a unique opportunity to study the dynamics of charge separation in systems where the initial separation of the electron-hole pair can be well controlled. The calculations in section 4.4.5.2 show the importance of the relative dielectric constant of the QD versus the surrounding matrix for nanometer scale systems as well as the importance of interface states. The large dielectric contrast of the semiconductor core versus the organic ligands leads to a large polarization energy that increases the energy cost to separate the photoexcited electron-hole pair.

Despite the success of the simple model presented in qualitatively describing the charge separation process, it is clear that many theoretical challenges remain to develop a complete description. In particular it is not clear where the applied potential is dropped, i.e. across the QD or across the organic. The calculations of the Coulomb interaction of charges on adjacent QDs are non-trivial and may need to be addressed using numerical methods. Finally, a more complete description of the potential energy near the interface and the relative positions of the

HOMO and LUMO for the organic molecules *bound* to the surface of the QD are required for quantitative evaluation of the tunneling probability.

4.5 Conclusions

Photoconductivity in QD solids is the result of field assisted ionization of a photoexcited exciton in its lowest excited state. Charge separation competes with rapid radiative and non-radiative recombination which both act to decrease the internal charge generation efficiency. Charge separation proceeds primarily via a tunneling process and the field dependence of the photocurrent depends on the energy required to separate the electron-hole pair. A resonant tunneling model for charge separation qualitatively reproduces the QD size and surface passivation dependence of the photocurrent. Regardless of whether charges escape from trap states or from QD core electronic states, the energy required for charge separation is considerably larger than the available thermal energy, even at room temperature. It is clear that carrier access to the surface of the QD can improve the charge separation efficiency, provided the surface does not also present sites for non-radiative recombination. The intensity dependence of the photocurrent indicates there is carrier recombination in the sample that reduces the external efficiency.

4.6 References

[1]L. Esaki and R. Tsu, IBM J. Res. Dev. **14**, 61 (1970).

[2]J.J. Welser, S. Tiwari, S. Rishton *et al.*, "Room temperature operation of a quantum-dot flash memory," IEEE Electron Device Letters **18** (6), 278-280 (1997).

[3]C.S. Lent, P.D. Tougaw, W. Prod *et al.*, "quantum dot cellular automata," Nanotechnology **4**, 49 (1993).

[4]W. Porod, C.S. Lent, G.H. Bernstein *et al.*, "Quantum-dot cellular automata: computing with coupled quantum dots," International Journal of Electronics **86** (5), 549-590 (1999).

[5]A.N. Korotkov, "Single-electron logic and memory devices," International Journal of Electronics **86** (5), 511-547 (1999).

[6]V.L. Colvin, M.C. Schlamp, and A.P. Alivisatos, "Light-Emitting-Diodes Made From Cadmium Selenide Nanocrystals and a Semiconducting Polymer," Nature **370** (6488), 354-357 (1994).

[7]B.O. Dabbousi, M.G. Bawendi, O. Onitsuka *et al.*, "Electroluminescence From Cdse Quantum-Dot Polymer Composites," Appl. Phys. Lett. **66** (11), 1316-1318 (1995).

[8]M.V. Artemyev, V. Sperling, and U. Woggon, "Electroluminescence in thin solid films of closely packed CdS nanocrystals," J. Appl. Phys. **81** (10), 6975-6977 (1997).

[9]Y. Wang and N. Herron, "Photoconductivity of CdS nanocluster-doped polymers," Chem. Phys. Lett. **200** (1,2), 71-75 (1992).

[10]Y. Wang and N. Herron, "Semiconductor nanocrystals in carrier-transporting polymers. Charge generation and charge transport," J. Lumines. **70**, 48-59 (1996).

[11]N.C. Greenham, X.G. Peng, and A.P. Alivisatos, "Charge separation and transport in conjugated-polymer/semiconductor-nanocrystal composites studied by photoluminescence quenching and photoconductivity," Phys. Rev. B **54** (24), 17628-17637 (1996).

[12]D.S. Ginger and N.C. Greenham,"Charge injection and transport in films of CdSe nanocrystals," J. Appl. Phys. **87**, 1361 (2000).

[13]M.A. Hines and P. Guyot-Sionnest, "Synthesis and characterization of strongly luminescing ZnS-Capped CdSe nanocrystals," J. Phys. Chem. **100** (2), 468-471 (1996).

[14]B.O. Dabbousi, J. RodriguezViejo, F.V. Mikulec *et al.*, "(CdSe)ZnS core-shell quantum dots: Synthesis and characterization of a size series of highly luminescent nanocrystallites," J. Phys. Chem. B **101** (46), 9463-9475 (1997).

[15]R.K. Iler, *The Chemistry of Silica* (John Wiley and Sons, New York, 1979), pp. 622.

[16]C.B. Murray, D.J. Norris, and M.G. Bawendi, "Synthesis and Characterization of Nearly Monodisperse CdSe (E = S, Se, Te) Semiconductor Nanocrystallites," J. Amer. Chem. Soc. **115** (19), 8706-8715 (1993).

[17]C.B. Murray, C.R. Kagan, and M.G. Bawendi, "Self-Organization of Cdse Nanocrystallites Into 3-Dimensional Quantum-Dot Superlattices," Science **270** (5240), 1335-1338 (1995).

[18]C.R. Kagan, "The Electronic and Optical Properties of Close Packed Cadmium Selenide Quantum Dot Solids," Ph.D. Thesis, Massachusetts Institute of Technology, 1996.

[19]O.I. Micic, K.M. Jones, A. Cahill *et al.*, "Optical, Electronic, and Structural Properties of Uncoupled and Close-Packed Arrays of InP Quantum Dots," J. Phys. Chem. B **102**, 9791-9796 (1998).

[20]V. Klimov, P.H. Bolivar, and H. Kurz, "Ultrafast carrier dynamics in semiconductor quantum dots," Phys. Rev. B **53** (3), 1463-1467 (1996).

[21]N.Y. Morgan, Ph.D. Thesis, Massachusetts Institute of Technology, 2000.

[22]S. Nespurek, V. Cimrova, J. Pfleger *et al.*, "Free charge carrier formation in polymers under illumination," Polymers For Advanced Technologies **7** (5-6), 459-470 (1996).

[23]L.B. Lin, S.A. Jenekhe, and P.M. Borsenberger, "Field and temperature dependencies of free carrier photogeneration efficiencies of molecular glasses," J. Chem. Phys. **105** (19), 8490-8494 (1996).

[24]J. Noolandi and K.M. Hong, "Theory of photogeneration and fluorescence quenching," J. Chem. Phys. **70** (7), 3230-3236 (1979).

[25]B. Alperson, S. Cohen, I. Rubinstein *et al.*, "Room-temperature conductance spectroscopy of CdSe quantum dots using a modified scanning force microscope.," Phys. Rev. B **52** (24), R17017 (1995).

[26]E. Lifshitz, I. Dag, I. Litvin *et al.*, "Properties of CdSe nanoparticle films prepared by chemical deposition and sol-gel methods," Chem. Phys. Lett. **288** (2-4), 188-196 (1998).

[27]R.H. Bube, *Photoconductivity of Solids* (John Wiley & Sons, New York, 1960).

[28]R.H. Terrill, T.A. Postlethwaite, C.H. Chen *et al.*, "Monolayers in three dimensions: NMR, SAXS, thermal, and electron hopping studies of alkanethiol stabilized gold clusters," J. Amer. Chem. Soc. **117** (50), 12537-12548 (1995).

[29]M.C. Schlamp, X.G. Peng, and A.P. Alivisatos, "Improved efficiencies in light emitting diodes made with CdSe(CdS) core/shell type nanocrystals and a semiconducting polymer," J. Appl. Phys. **82** (11), 5837-5842 (1997).

[30]H. Mattoussi, L.H. Radzilowski, B.O. Dabbousi *et al.*, "Electroluminescence from heterostructures of poly(phenylene vinylene) and inorganic CdSe nanocrystals," J. Appl. Phys. **83** (12), 7965-7974 (1998).

[31]L. Onsager, "Initial recombination of ions," Physical Review **54**, 554-557 (1938).

[32]S. Rackovsky and H. Scher, "Theory of Geminate Recombination As a Molecular Process," Phys. Rev. Lett. **52** (6), 453-456 (1984).

[33]Y. Wang and A. Suna, "Fullerenes in Photoconductive Polymers. Charge Generation and Charge Transport," J. Phys. Chem. B **1997** (101), 5627-5638 (1997).

[34]L.E. Brus, "Electron-electron and electron-hole interactions in small semiconductor crystallites: The size dependence of the lowest excited state," J. Chem. Phys. **80** (9), 4001 (1984).

[35]L.E. Brus, "A simple model for the ionization potential, electron affinity and aqueous redox potentials of small semiconductor crystallites," J. Chem. Phys. **79** (11), 5566-5571 (1983).

[36]D. Babic, R. Tsu, and R.F. Greene, "Ground state energies of one-and two-electron silicon dots in an amorphous silicon dioxide matrix," Phys. Rev. B **45** (24), 14150-14155 (1992).

[37]L. Wang and A. Zunger, "Pseudopotential calculations of nanoscale CdSe quantum dots," Phys. Rev. B **53** (15), 9579-9582 (1996).

[38]M. Shim and P. Guyot-Sionnest, "Permanent dipole moment and charges in colloidal semiconductor quantum dots," J. Chem. Phys. **111** (15), 6955-6964 (1999).

[39]P. Guyot-Sionnest, M. Shim, C. Matranga *et al.*, "Intraband relaxation in CdSe quantum dots," Phys. Rev. B **60** (4), R2181-R2184 (1999).

[40]V.I. Klimov, A.A. Mikhailovsky, D.W. McBranch *et al.*, "Mechanisms for intra-band energy relaxation in semiconductor quantum dots: The role of electron-hole interactions," Phys. Rev. B **61** (20), R13349-R13352 (2000).

Chapter 5

Fluorescence Quenching and Transient Photoconductivity

5.1 Introduction

The steady-state photoconductivity measurements presented in Chapter 4 strongly suggest that separation of the photoexcited electron-hole pair is the rate-determining step in photoconductivity of CdSe quantum dot solids. In this chapter we examine this hypothesis further by measuring the photoluminescence (PL) quantum efficiency under steady state photoconductivity conditions. Charge separation decreases the PL quantum efficiency of neutral QDs by providing an additional non-radiative pathway for destruction of excitons. If the applied electric field enhances the photocurrent and decreases the fluorescence quantum efficiency proportionally, then this is strong evidence that geminate recombination is the rate limiting process.[1]

For semiconductor QD solids, analysis of PL quenching data is complicated by both field induced and photo-induced processes that can affect the intrinsic PL quantum efficiency in the absence of charge separation. First, the radiative rate may be field dependent through the quantum-confined Stark effect.[2-5] Sacra [6] found that when CdSe QDs embedded in an insulating polymer were resonantly excited into the lowest energy exciton state, an applied electric field enhanced the PL quantum efficiency but left the PL lifetime nearly unchanged, consistent with a slight increase in the radiative rate.* Second, there is a growing body of evidence[7] [8], albeit

* When the same QDs were excited more than 50 meV above the band edge, an applied electric field decreased both the PL quantum efficiency and the PL lifetime, consistent with an increase in the non-radiative rate. The mechanism was tentatively assigned to ionization.

circumstantial, that a charged QD does not fluoresce. Efficient Auger-like non-radiative recombination, where the exciton energy is transferred to the third carrier, is predicted to make charged QDs essentially "dark" in emission compared to neutral QDs.[9] The Auger model has been used to explain photodarkening in semiconductor-doped glasses[10,11] as well as fluorescence intermittency of single nanocrystal QDs.[12-14]

In this chapter, we attempt to deconvolute these different effects and determine the internal charge generation efficiency as a function of applied electric field. The PL quantum efficiency in an external applied field is examined for close-packed and isolated QDs and when charge is injected into the QD solid from the electrical contacts.

5.2 Experiment

Glassy films of colloidal CdSe QDs are prepared as described in Chapter 1 and drop cast from solution on to lithographically patterned sapphire, crystalline quartz, or silicon substrates (described in Chapter 4). All electrical contacts are made *prior* to film deposition and measurements are performed under vacuum in a cold finger cryostat. To prevent charge from being "frozen in" the QD solid, the sample is cooled to cryogenic temperatures with all the contacts grounded. Quenching of the fluorescence in an electric field is measured using a far field epi-fluorescence microscope, spectrometer and liquid nitrogen cooled CCD camera described in detail elsewhere.[15] In spectral mode, the fluorescence image of the electrodes and sample is projected on to the entrance slits of the monochromator, which are then narrowed so

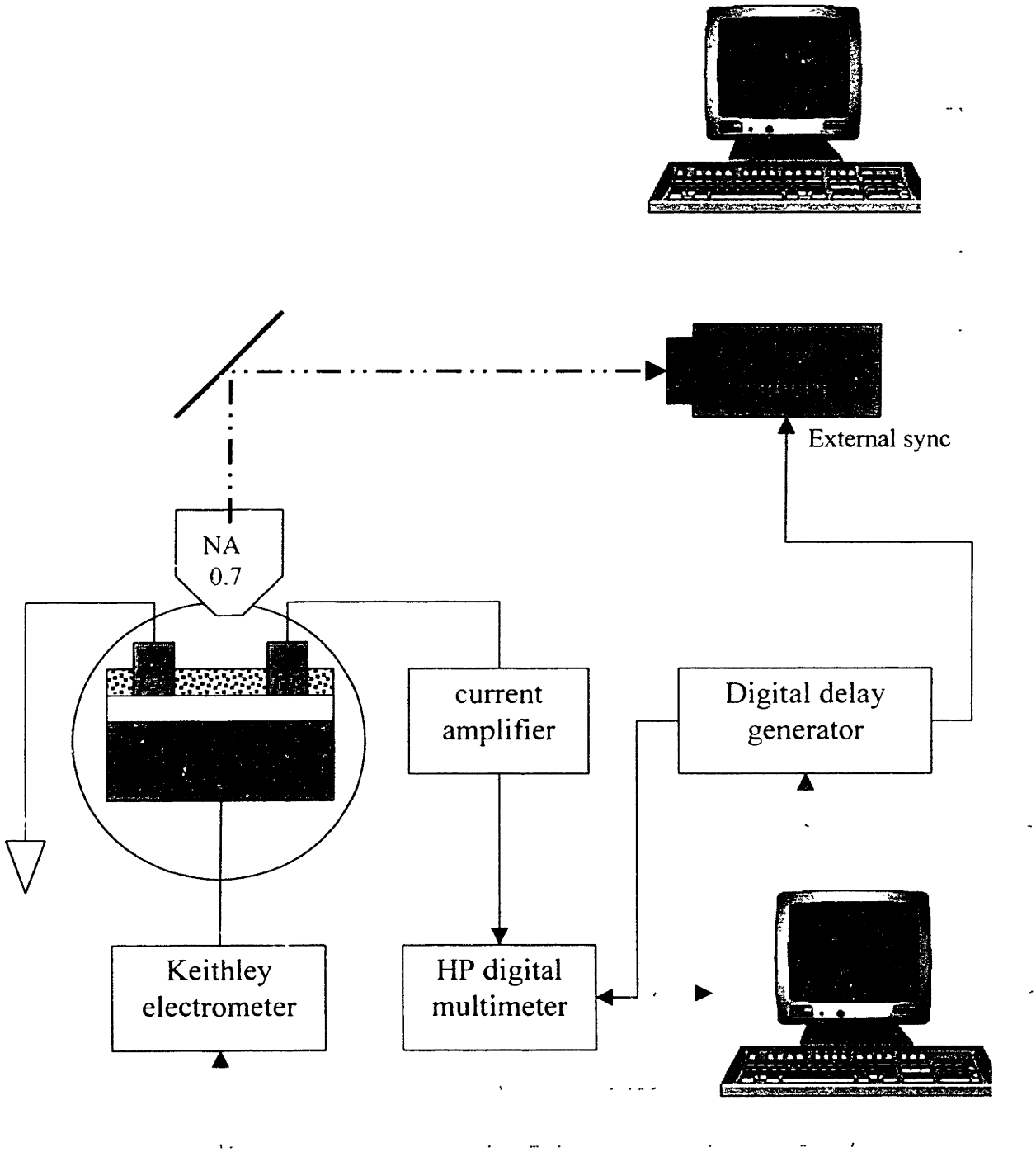

Figure 5.1: Experimental setup for fluorescence quenching experiments. The circled region is inside the cryostat. TTL pulses from the delay generator are used to trigger the HP 34401A multimeter for each transient and to trigger the CCD camera shutter. Dashed connectors indicate GPIB control.

that only the emission from the center region between the electrodes is collected. In image mode, the entrance slits of the spectrometer are left open and the grating is replaced with a mirror so that the image of the electrodes is projected onto the CCD camera. In order to average out fluctuations in the collected fluorescence intensity due to vibrations of the cold finger, long exposure times (typically 10-30 s) are used to record the PL spectra as a function of the applied field. The excitation source is the 514 line of an argon ion laser.

Concurrent with the optical measurements, the DC photoconductivity of the QD solid is recorded using a Keithley 6517 electrometer to apply a bias voltage and measure photocurrent. Except where noted the gate electrode is held at ground. Transient photoconductivity and charging measurements are acquired using the same electrometer to apply a bias voltage and a Keithley 428 current amplifier to measure the photocurrent. For fast transients (< 1s) the analog output of the current amplifier is acquired using a TDS 520 digital oscilloscope. For slow transients (> 1s), the analog output is digitized using a HP 34401A digital multimeter and acquired using a personal computer. Figure 5.1 shows a schematic of the experimental set-up for simultaneous PL quenching and charging experiments.

5.3 Results

Strongly field dependent, reversible PL quenching is observed for QD solids at 10 K. Figure 5.2 shows a series of PL spectra acquired as the electric field was stepped from 0 to 150 kV/cm in steps of 25 kV/cm. The band edge PL intensity decreases with increasing electric field with no evidence of line broadening or a shift in the emission energy. In the inset, the fractional change in the integrated PL intensity (Φ) is plotted as a function of applied field (F). The PL

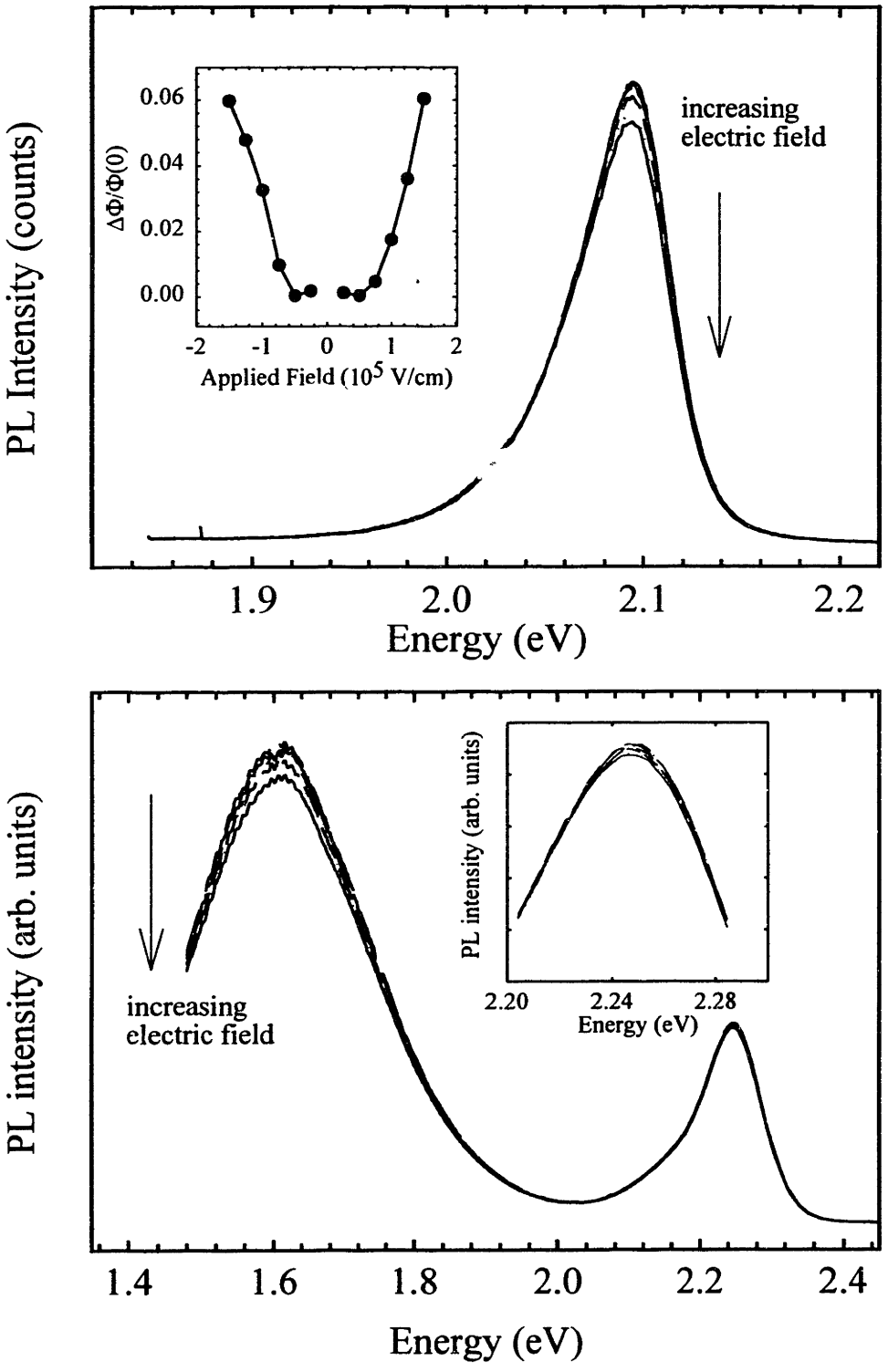

Figure 5.2 **(A)** Fluorescence quenching at 10 K for a well passivated 24 Å TOPO/TOP capped QD solid. Spectra are shown in steps of 25 kV/cm starting at 0 V/cm. In the inset, the fractional change in integrated PL intensity $-|\Delta\Phi|/\Phi(0)$ is plotted as a function of applied field. **(B)** Fluoresence quenching at 10 K for a poorly passivated 19 Å TOPO/TOP capped QD solid. The inset shows a blow-up of the band edge PL .

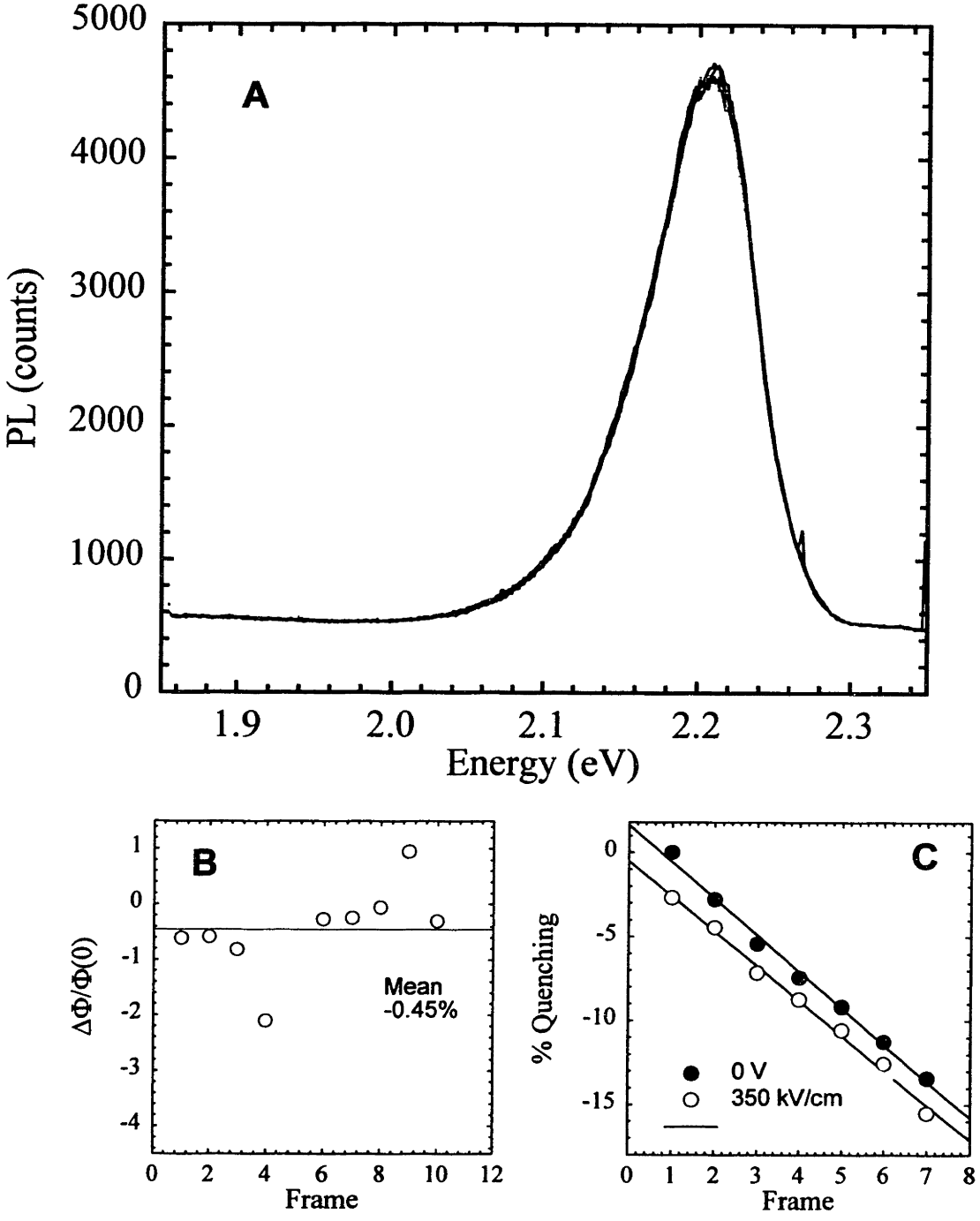

Figure 5.3 (A) Series of PL spectra acquired at 10 K with an alternating electric field of 0 and 350 kV/cm and excitation intensity of ~ 3 Watts/cm^2. **(B)** $\Delta\Phi/\Phi(0)$ as a function of time of the same data as shown in A. **(C)** Percent change in PL intensity from the start of the run under high excitation intensity (~ 120 Watts/cm^2). All data is for a 21 Å TOPO/TOP capped QD solid on a quartz substrate.

quenching is symmetric with respect to the applied electric field reaching a maximum of 6% at 150 kV/cm. For poorly passivated QDs, "deep trap" PL associated with surface defects is observed below the band edge. At 10 K, the deep trap PL is quenched more than the band edge PL (Figure 5.2B). The same qualitative behavior as is shown in Figure 5.2A was previously reported by Kagan.[16] However, quantitative measurement of the fluorescence quenching was not possible in that experiment.

To examine whether the observed PL quenching is due to charge separation or a Stark effect, the PL is measured for a sub-monolayer of QDs between interdigitated gold electrodes on quartz. Figure 5.3A shows a series of spectra under alternating electric field of 350 kV/cm and 0 V. Under this relatively low excitation intensity, the emission peak shifts to lower energy by approximately 2 meV at 350 kV/cm but the mean PL quenching is less than 0.5% (Figure 5.3B). Under high excitation intensities (> 100 Watt/cm^2) significant field induced PL quenching (up to 2%) as well as photobleaching of the PL is observed. Figure 5.3C shows the integrated PL intensity as a function of time under the same alternating electric field as before. The small field-induced PL quenching is superimposed on a much larger photo-induced effect.

Figure 5.4 compares the fractional change in PL intensity and the external charge generation efficiency (η) calculated from the photocurrent per absorbed photon. If the only process induced by the electric field is charge separation and there is no trapping or recombination within the sample, then these two quantities should be equal (see Appendix). We observe that the external charge generation efficiency is four orders of magnitude smaller than the fractional change in the PL intensity. On both sapphire and silicon substrates, a slight increase in the PL intensity is observed for low to moderate electric fields followed by quenching

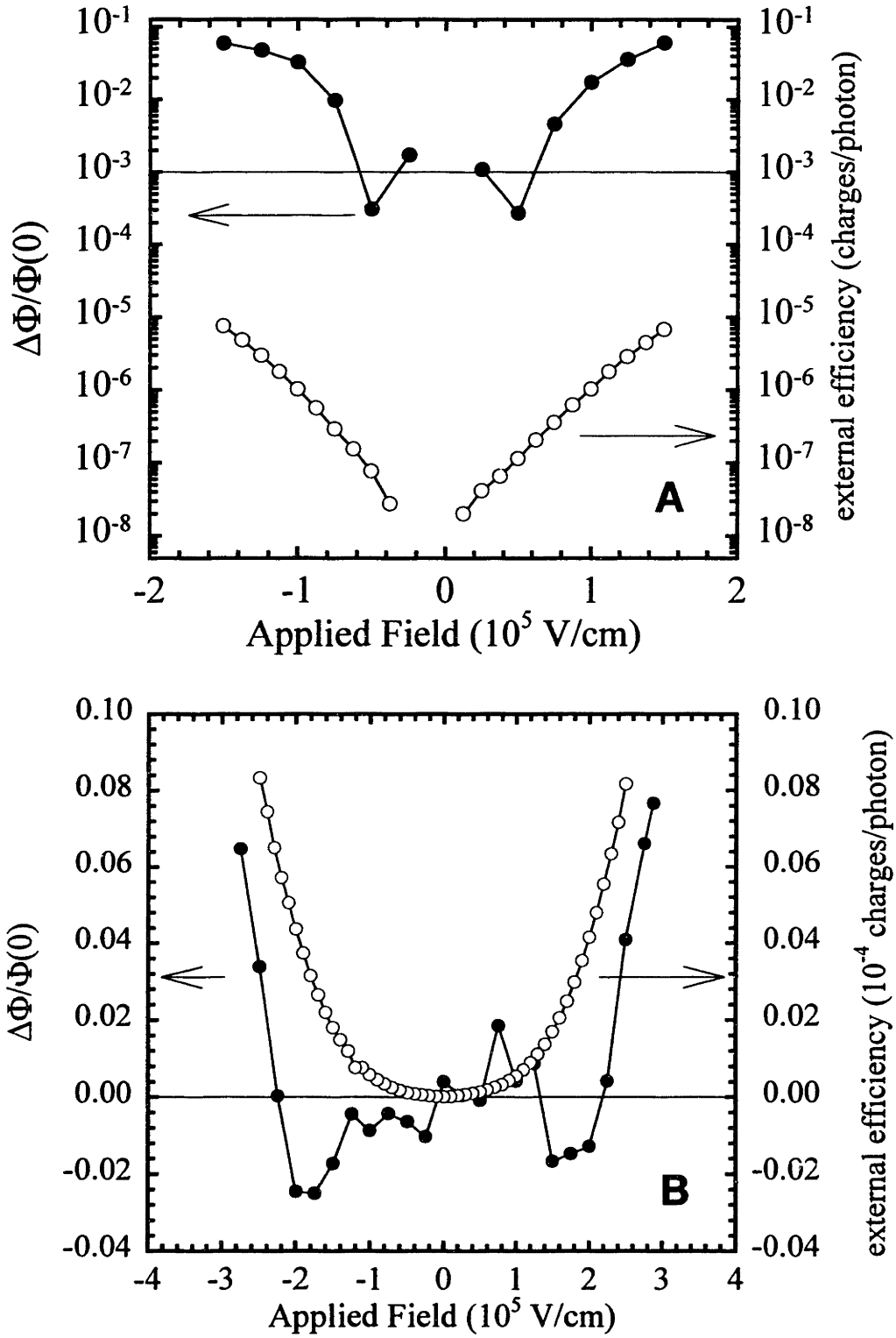

Figure 5.4 Fractional change in PL intensity, $-\Delta\Phi/\Phi(0)$ (●) and measured absolute photocurrent (○) in units of charges per absorbed photon for (A) a 24 Å TOPO/TOP capped QD solid on a silicon substrate with 600 nm gate oxide, and (B) 22 Å TOPO/TOP QD solid on sapphire. In both cases the electrode spacing is 20 μm.

at high electric fields. No electroluminescence from the QD solid is detectable in the dark that could explain the characteristic "W" shape of the field dependent PL intensity. For both kinds of substrates, the field dependence of the photocurrent and PL quenching have a similar shape at high fields.

To determine how charge density in the QD solid affects the PL quantum efficiency, a bias is applied to the gate electrode. The QD solid is effectively one plate of a parallel plate capacitor where the gate oxide is the dielectric layer. The charge flowing into the sample is measured by integrating the current detected at one of the top gold electrodes using a current amplifier (at a virtual ground). The other top electrode is kept grounded for the entire experiment. Figure 5.5 shows a typical charging cycle when the gate voltage is cycled through + 120 V, 0 V, -120 V and 0 V in 40 s steps. When the gate voltage is changed from ±120 V to 0 V, only a small fraction of the charge that was injected flows back into the contacts. The remaining charge is effectively trapped in the QD solid until the bias is reversed. Much more charge flows into the QD solid when the sample is illuminated during the charging period than when it is held in the dark.

In the example shown in Figure 5.5, the charge injected into the film under illumination is approximately equal to that expected from the applied voltage at the geometric capacitance of region between the source and drain electrodes (~ 21 pC). However since the active area is not bounded, some of the measured charge flowed into the film everywhere around the perimeter of the measurement electrode. As a result, it is not possible to directly estimate the average occupancy of the QDs in the observation region between the electrodes from the charging curves.

While the charging transients are very reproducible, the accompanying PL modulation is not. When the PL is analyzed in spectral mode, a small oscillation in the integrated intensity (up

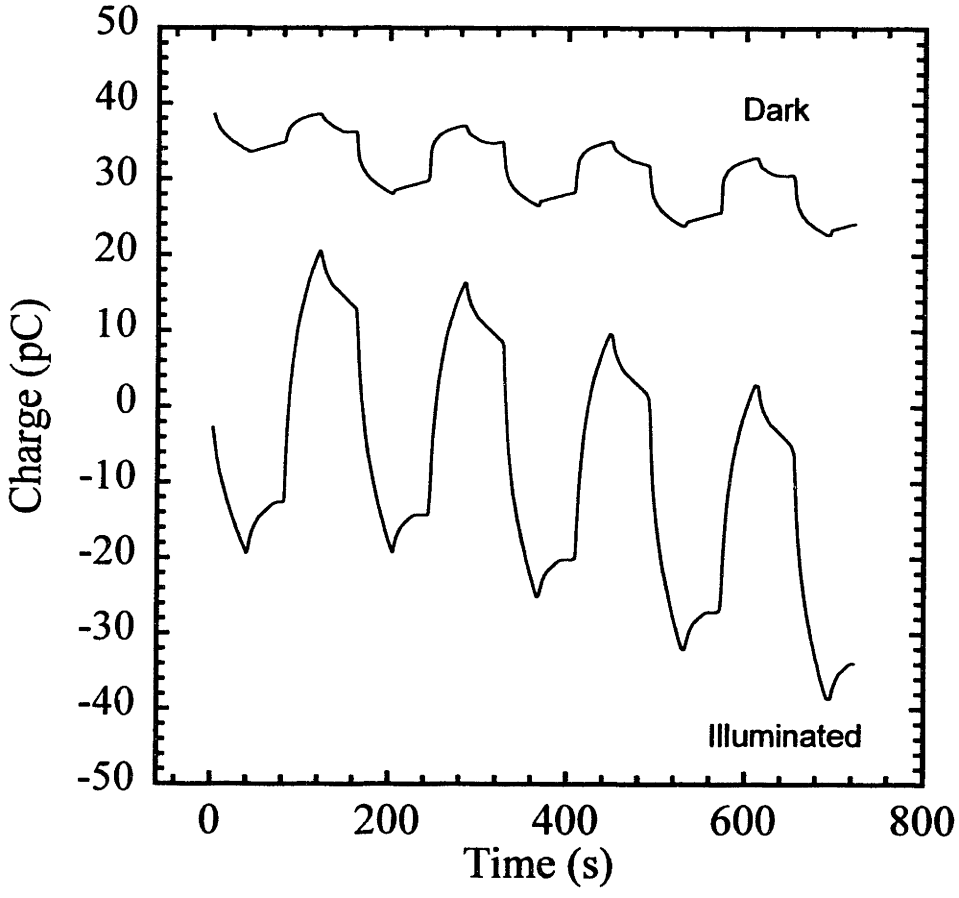

Figure 5.5 Cumulative charge injected into a 27.4 Å TOPO/TOP capped QD solid under illumination and in the dark. The dark and illuminated lines are offset for clarity. The gate voltage is cycled through +120 V, 0 V, -120 V and 0V in 40 s steps. The sample is on a silicon substrate with a 330 nm gate oxide and source-drain electrode spacing of 2 μm. T = 150 K.

to 5%) is observed that is usually positively correlated with gate voltage (i.e. positive bias yields the greatest PL intensity). In image mode however, careful analysis of the fluoresence image shows that the PL intensity oscillates with gate voltage both between, and on top of, the gold electrodes. This is quite surprising since there should be no electric field on top of the electrodes. No correlation with gate bias is observed when both the gate and the top contacts are held at the same potential.

At present we are unable to eliminate a piezoelectric or other mechanical effect as the reason for the apparent correlation between gate voltage and PL intensity. The shallow depth of focus of the microscope objective means that the measurements are quite sensitive to vibrations of the cold finger. Under the same experimental conditions, the image intensity of a non-conducting test sample varied by up to 2% (excluding systematic drifts such as photobleaching).

5.4 Discussion

The PL quenching data acquired under steady state photoconductivity conditions indicates that the applied electric field affects the non-radiative recombination rate for the ensemble of QDs.* For relatively low applied fields, PL quenching is observed for the QD solid that is not accompanied by a shift in the emission energy or line-broadening associated with the quantum-confined Stark effect (see Figure 5.1). Little PL quenching is measured when the QDs are isolated from each other (Figure 5.2). Single QDs dispersed more than 1 μm apart on quartz substrates exhibit less than 0.1% PL quenching in applied electric fields of 350 kV/cm.* From this progressive decrease in the effect of the electric field as the QDs are isolated from each

* It is important to distinguish between non-radiative processes intrinsic to a single isolated QD and non-radiative processes characteristic of the ensemble. For example if the intrinsic QY is 100% but half the QDs are charged and therefore dark, then the measured QY is 50%.

other, it is apparent that field induced PL quenching requires charge separation and transfer, either to the surrounding matrix or to another QD.

For charge transfer to be detectable as a change in the apparent PL quantum efficiency (> 1%), either the charge transfer rate is comparable to the intrinsic radiative and non-radiative recombination rate in the parent QD or charge transfer introduces new non-radiative pathways for exciton annihilation. In the first case, the fractional change in the integrated PL intensity as a function of applied electric field (F) is given by,[1]

$$\frac{\Phi(0)-\Phi(F)}{\Phi(0)} = \frac{\eta(F)-\eta(0)}{1-\eta(0)} \tag{5.1}$$

where $\eta(F)$ is given by equation (4.2). In the second case, the charge separation rate is assumed to be much slower than the intrinsic exciton recombination rate but the lifetime of carriers in the QD solid is long. If the charge carriers that are produced completely quench the PL of each QD they occupy, the rate of PL of the ensemble is given by,

$$I(F) = \frac{k_r G}{k_r + k_{nr}}\left[1 - N(F)\right] \tag{5.2}$$

where G is the generation rate (excitons/s), k_r and k_{nr} are the intrinsic radiative and non-radiative rates, and $N(F)$ is the fraction of QDs in the ensemble that is charged. In deriving equation (5.2) we assume that because of the large Coulomb charging energy, each QD is never more than singly charged until the entire array has been filled. In this scenario, the PL intensity is inversely proportional to the density of charge carriers.

The charging experiments with the gate electrode failed to produce convincing evidence that directly charging the QD solid substantially modifies the PL quantum efficiency. It is

---

[*] S.A. Empedocles. Private communication.

possible that charges were injected into trap states rather than delocalized particle-in-a-sphere states. The Auger recombination model proposed by Chepic *et al.* [9] may not apply when the extra charge occupies a localized trap state. Until the relationship between the electronic state of the injected charge and its effect on the PL is better understood, we must reject this mechanism for the PL quenching.

Returning to the implications of the pure charge separation model, the charge transfer rate (k_F) must exceed $4x10^5$ s^{-1} to yield a 1% change in PL intensity (assuming a 25 ns intrinsic exciton lifetime ($1/\tau = k_r + k_{nr}$) at 10 K). A charge separation rate of this magnitude is too large to be consistent with photoconductivity measurements reported in Chapter 4. Recall that when charge separation is the rate limiting step and k_F is much less than τ, η can be approximated as ~ $k_F\tau$. The shape and amplitude of the I-V curves are then separable into pure functions of temperature and electric field. This behavior was demonstrated in Figure 4.3A and B. This separation is not possible if k_F is comparable to the intrinsic exciton recombination rate and the shape of the I-V curve should change with temperature. It is possible that there is a correlation between the weak temperature dependence that is sometimes observed (see Figure 4.3C) and observation of PL quenching. This should be investigated further.

Quenching of the deep trap PL is observed at lower applied fields than quenching of the band edge PL (Figure 5.1B). The deep PL was recently assigned to recombination of shallow trapped electrons and deep trap holes.[17] The calculations of Chapter 4 suggest that more energy is required to separate excitons confined to the core of the QD than electron-hole pairs where one or both carriers are separately trapped at the surface of the parent QD. Low field quenching of the deep trap PL is qualitatively consistent with that result.

5.5 Conclusions

At present we cannot reconcile both the fluorescence quenching and the photoconductivity data to a simple model. It is clear that field-induced PL quenching requires charge separation but the exact mechanism linking this process to the measured PL quantum efficiency is not understood. Careful studies of the PL lifetime as a function of electric field, temperature, and charge density in the QD solid may shed some light on this mystery. In particular, the Auger ionization process should affect the fast component of the decay whereas charge separation processes are more likely to affect the slowest components in the decay. The effect of charge injection should also be studied for samples with varying degrees surface passivation.

5.6 References

[1]J. Noolandi and K.M. Hong, "Theory of photogeneration and fluorescence quenching," J. Chem. Phys. **70** (7), 3230-3236 (1979).

[2]F. Hache, D. Ricard, and C. Flytzanis, "Quantum-Confined Stark-Effect in Very Small Semiconductor Crystallites," Appl. Phys. Lett. **55** (15), 1504-1506 (1989).

[3]V.L. Colvin, K.L. Cunningham, and A.P. Alivisatos, "Electric-Field Modulation Studies of Optical-Absorption in Cdse Nanocrystals - Dipolar Character of the Excited-State," J. Chem. Phys. **101** (8), 7122-7138 (1994).

[4]A. Sacra, D.J. Norris, C.B. Murray *et al.*, "Stark Spectroscopy of Cdse Nanocrystallites - the Significance of Transition Linewidths," J. Chem. Phys. **103** (13), 5236-5245 (1995).

[5]S.A. Empedocles and M.G. Bawendi, "Quantum-confined stark effect in single CdSe nanocrystallite quantum dots," Science **278** (5346), 2114-2117 (1997).

[6]A. Sacra, "Stark Spectroscopy of Cadmium Selenide (CdSe) Nanocrystallites," Ph.D. Thesis, Massachusetts Institute of Technology, 1996.

[7]M.Y. Shen, M. Oda, and T. Goto, "Direct evidence of photoionization of CdTe nanocrystals embedded in trioctylphosphine oxide," Phys. Rev. Lett. **82** (19), 3915-3918 (1999).

[8]T.D. Krauss and L.E. Brus, "Charge, polarizability, and photoionization of single semiconductor nanocrystals," Phys. Rev. Lett. **83** (23), 4840-4843 (1999).

[9]D.I. Chepic, A.L. Efros, A.I. Ekimov *et al.*, "Auger Ionization of Semiconductor Quantum Drops in a Glass Matrix," J. Lumines. **47** (3), 113-127 (1990).

[10]V.J. Grabovskis, J.J. Dzenis, A.I. Ekimov *et al.*, "Photoionization of Semiconductor Microcrystals in Glass," Soviet Physics Solid State **31** (1), 272-275 (1989).

[11]C. Flytzanis, D. Ricard, and M.C. SchanneKlein, "The role of photodarkening and Auger recombination in the dynamics of the optical response for Cd(S,Se) nanoparticles," J. Lumines. **70**, 212-221 (1996).

[12]M. Nirmal, B.O. Dabbousi, M.G. Bawendi *et al.*, "Fluorescence intermittency in single cadmium selenide nanocrystals," Nature **383** (6603), 802-804 (1996).

[13]A.L. Efros and M. Rosen, "Random Telegraph Signal in the Photoluminescence Intensity of a Single Quantum Dot," Phys. Rev. Lett. **78** (6), 1110-1113 (1997).

[14]M. Kuno, D.P. Fromm, H.F. Hamann *et al.*, "Nonexponential "blinking" kinetics of single CdSe quantum dots: A universal power law behavior," J. Chem. Phys. **112** (7), 3117-3120 (2000).

[15]S.A. Empedocles, "Detection and Spectroscopy of Single CdSe Nanocrystallite Quantum Dots," Ph.D. Thesis, Massachusetts Institute of Technology, 1999.

[16]C.R. Kagan, "The Electronic and Optical Properties of Close Packed Cadmium Selenide Quantum Dot Solids," Ph.D. Thesis, Massachusetts Institute of Technology, 1996.

[17]E. Lifshitz, I. Dag, I. Litvin *et al.*, "Properties of CdSe nanoparticle films prepared by chemical deposition and sol-gel methods," Chem. Phys. Lett. **288** (2-4), 188-196 (1998).

Appendix

The relationship between the internal and external charge generation efficiency may easily derived starting from the continuity equation,

$$\vec{j} = qn\vec{v} \tag{5.3}$$

where j is the current density, n is electron density, and v is the velocity of the current sheet. For simplicity we consider only the electron current and assume that the charge density under illumination (Δn) is approximately equal to n. Δn is found by solving the kinetic equation for steady state conditions,

$$\frac{dn}{dt} = G\eta - \frac{1}{\tau_n}n \qquad \Delta n = G\eta\tau_n \tag{5.4}$$

In equation 5.4, G is the generation rate in units of excitons per second, per unit volume, η is the internal charge generation efficiency, and τ_n is the carrier lifetime. For optically thin samples, G is approximately equal to,

$$G = \phi N_d C_{abs} \tag{5.5}$$

where ϕ is the photon flux per unit area, N_d is the density of QDs per unit volume, and C_{abs} is the absorption cross-section. Thus the photocurrent is equal to,

$$I = G\eta\tau_n\mu_n FA \tag{5.6}$$

$\mu_{n(p)}$ and $\tau_{n(p)}$ are the mobility and lifetime of a free carrier respectively and A is the cross-sectional area of the electrodes. The external efficiency (ξ) in units of charges per absorbed photon is given by,

$$\xi(F) = \tau_n\mu_n\eta(F)F\frac{1}{L} \tag{5.7}$$

where L is the distance between the electrodes. If the lifetime of the carrier is equal to the transit time to the electrodes ($\tau = t_\eta = L/\mu F$), then ξ is exactly equal to η.*

* Except for a mysterious factor of 2!

Chapter 6

Preliminary Observations of Amplified Spontaneous Emission*

6.1 Introduction

One of the great technological advantages of colloidal semiconductor QDs is that while they have the desirable optical properties and robust nature of a semiconductor, they can be synthesized and processed inexpensively in the manner of large molecules or polymers. Many device applications that take advantage of the tunable optical properties and easy processibility have been explored already including LEDs[1,2], cathodoluminescent devices[3], photovoltaics[4,5] and photonic band gap structures[6]. Notably absent is the nanocrystal QD laser. Almost twenty years ago researchers working on semiconductor laser diodes recognized the intrinsic advantage that semiconductor QDs would have over other semiconductor structures as a gain medium.[7,8] In particular the widely separated, discrete, electronic states near the band edge would concentrate the injected carriers at the energy levels of the stimulated emission transition. In theory, this results in reduced lasing threshold, higher gain[9], and greatly reduced temperature dependence compared to quantum well semiconductor lasers.

QD lasers have been demonstrated with self-assembled Stranski-Krastanow type QDs embedded in semiconductor heterostructures[10]; room temperature, electrically pumped, laser diodes operating in the IR[9] and with red emission[11] have been recently reported. At present the QDs in these lasers are rather large with behavior consistent with weak to intermediate quantum confinement. As a result, the emission wavelength is

primarily controlled through the material composition rather than QD size. Gain has also been observed for CdS QDs in the intermediate confinement regime embedded in glass.[12,13] However despite numerous efforts,[14] stimulated emission from the more tunable, strongly confined QDs has not been observed, until now.[15]

In this chapter we demonstrate single-pass, amplified spontaneous emission (ASE) from semiconductor QD solids in the strong confinement regime. The stimulated emission is tunable with size of the QD. While much work remains to be done to fully characterize this system, the implications are already of great technological importance. We will discuss some of the device possibilities at the end of this chapter.

6.2 Experiment

CdSe QD solids are prepared using the methods described in Chapter 1. Thick films with O.D. ~ 0.2-0.3 at the $1S_e1S_{3/2h}$ absorption feature are deposited on crystalline quartz substrates and mounted in a cold finger cryostat. The film of close-packed QDs on a quartz substrate acts as an asymmetric slab waveguide with most of emitted photons being channeled out the edge (Figure 6.1). Straight forward waveguide calculations indicate that the slab supports one TE and one TM mode for 0.08 um < d < 0.6 um and typical QD emission frequencies.[16]

The samples are excited with ~ 3.1 eV, 120 fs pulses from a regeneratively amplified Ti-sapphire laser operating at 1 kHz. The excitation beam is passed through a cylindrical lens to form a ~ 0.5 cm x 0.02 cm strip on the sample. The PL is collected at right angles, dispersed with a HR 640 monochromator (0.64 m, 150 groove/mm grating, Instruments SA) and detected with a liquid nitrogen cooled CCD camera. The spectral

* The data discussed in this chaper also appears in reference [15].

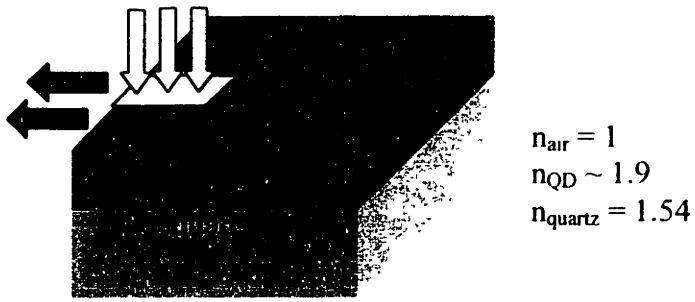

Figure 6.1: Experimental geometry for detection of photoluminescence.

resolution of the complete system is ~ 0.6 nm. A shutter is used to block the excitation beam except when acquiring spectra. For the preliminary experiments shown in Figure 1B, the PL is detected with a fiber optic integrated spectrometer from Ocean Optics (resolution ~ 5 nm).

6.3 Results

Figure 6.2 shows PL spectra as a function of excitation intensity for three different size QD solids and with various surface treatments. In all three cases, a distinct narrowing of the PL band is observed with increasing excitation intensity. Threshold type behavior is observed in the peak PL as a function of excitation power that is not observed in the off resonance parts of the PL curve (Figure 6.3) or for the integrated PL intensity. The narrow band emission is more prominent on the low energy tail of the PL for the large QDs. For the small QDs, the entire PL band appears to narrow and shift to lower energies at the same time. Development of narrow band emission does not strongly depend on the surface passivation of the QDs: ZnS overcoated QDs have typical

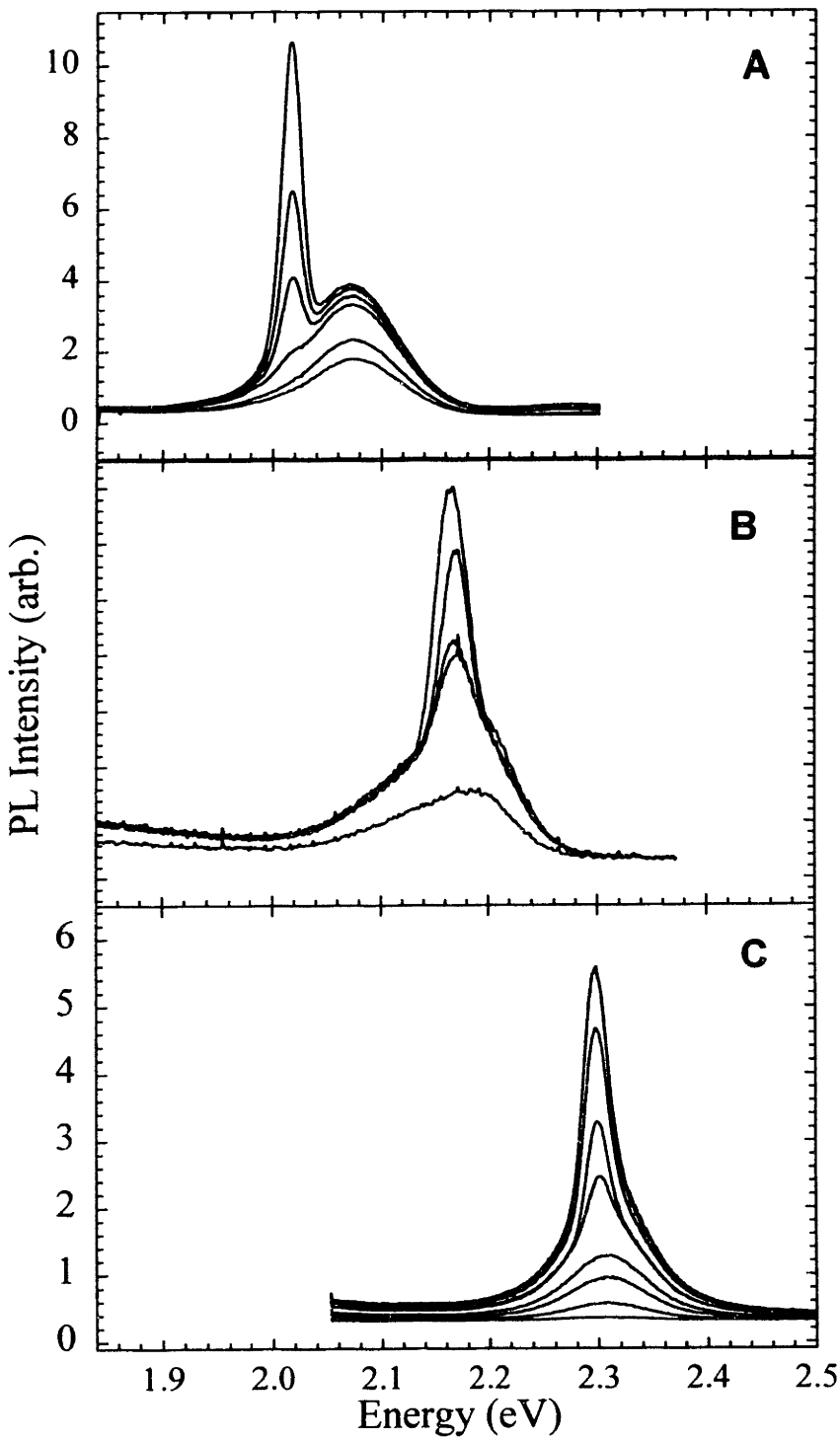

Figure 6.2 PL spectra as function of excitation intensity for **(A)** 21 Å TOPO/TOP QDs at 77 K. **(B)** 19 Å TOPO/TOP capped QDs at 10 K, and **(C)** 13.8 Å ZnS overcoated (4 m. nominal) QDs at 77 K.

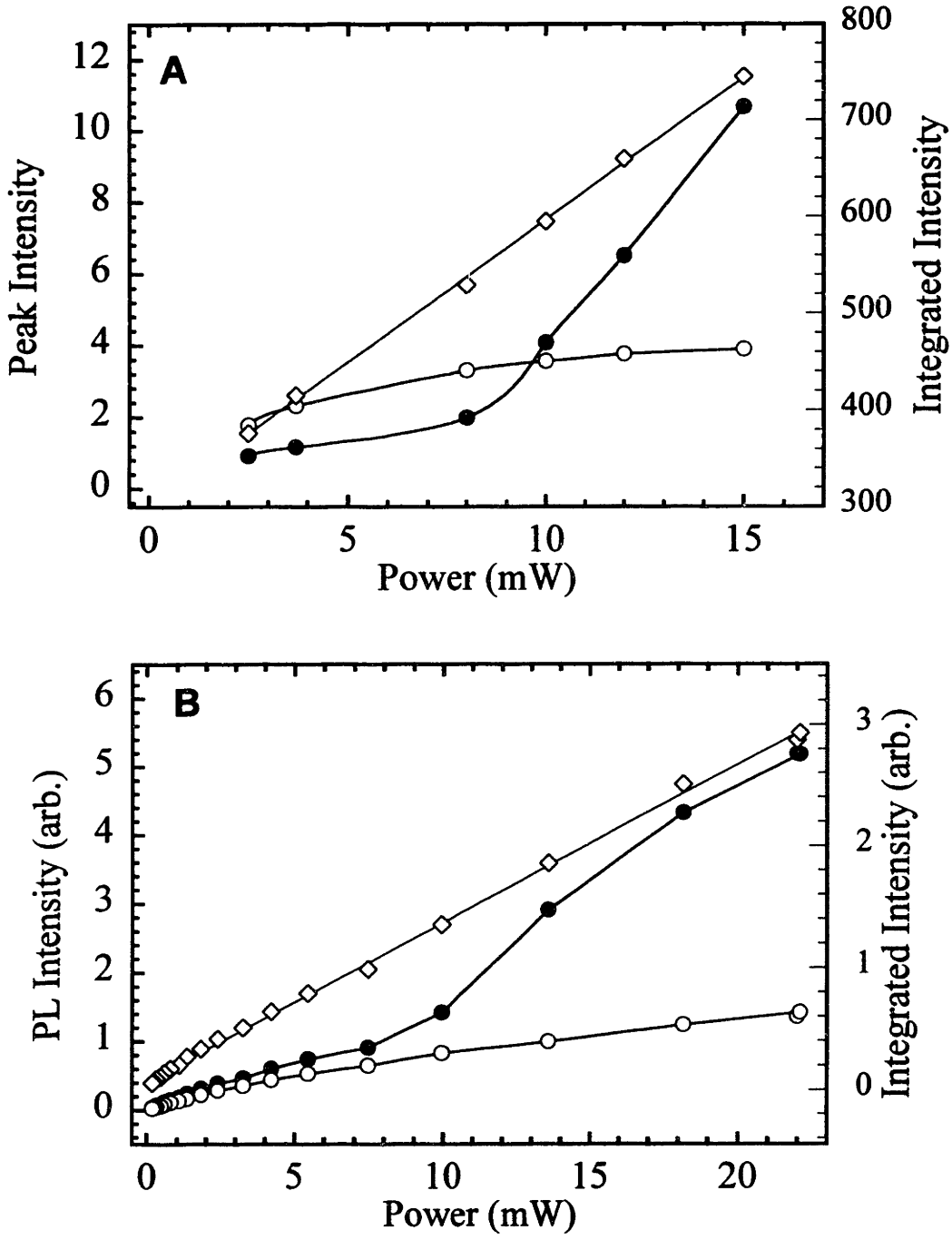

Figure 6.3 Pump power dependence of the PL at the energy of the narrowed emission(●), off resonance (○) and of the PL integrated over all wavelengths (◇). Panel **A** is for a 21 Å TOPO/TOP QD solid at 77 K. Panel **B** is for a 13.8 Å ZnS overcoated (4 m. nominal) QD solid at 77 K .

solution quantum efficiencies of ~25%. "Bare" QDs with passivated only by the organic ligands (TOPO/TOP) have typical quantum efficiencies of ~1-2% after the extensive washing required to form close-packed films free of excess cap. In Figure 6.2B, low energy "deep trap" emission associated with surface defects is observed. Despite the relatively poor surface passivation, it is still possible to develop the narrow band emission.

The data in Fig 6.2C is normalized and re-plotted in Fig 6.4 to compare the line width of the emission, above and below the threshold for spectral narrowing. For the 15 Å sample, saturation of the line width is observed above $I_0 \sim 20$ mW (Figure 6.4B). At the same time as the narrowing occurs, the spectra exhibit a slight shift to lower energies. The spectrally narrowed emission peak occurs at approximately the same energy as the room temperature solution PL under low power cw excitation (Figure 6.4A). While this is qualitatively consistent with recombination of a single quantum-confined exciton it is also somewhat surprising. We discuss this further in the next section.

Concurrent with the emission measurements, pump-probe measurements were performed on similar films in transmission mode. Figure 6.5 shows typical transient absorption spectra, acquired 1.5 ps after the pump pulse. The bleach observed on the lower energy edge of the absorption spectrum turns to gain at sufficient pump intensities. The maximum gain observed to date is ~ 500 cm^{-1}. Since the transient absorption measurements are less sensitive to lateral cracks in the film than the edge detected stimulated emission, the net gain determined by the pump-probe technique represents an upper bound for the QD solid.

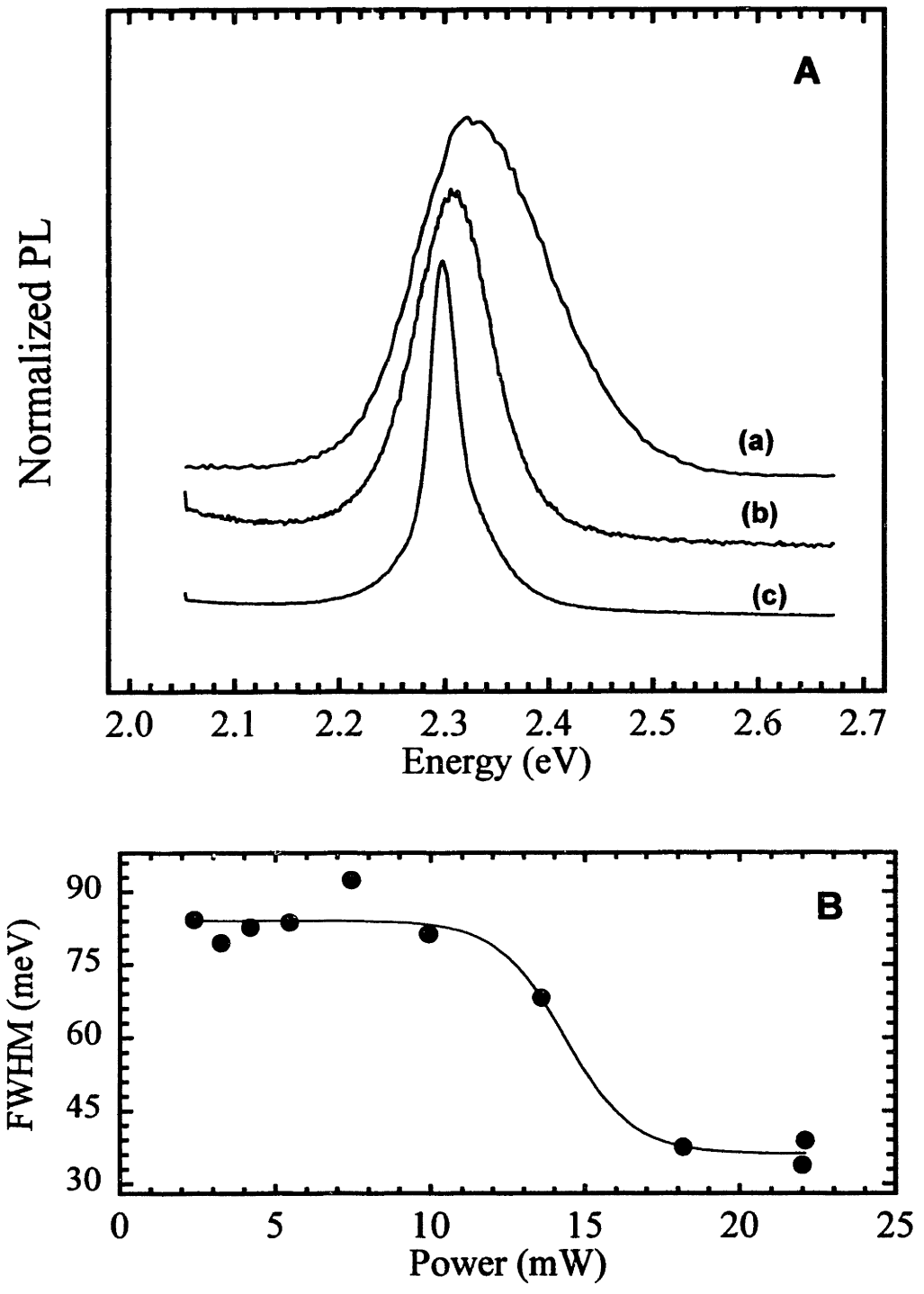

Figure 6.4 (A) Normalized PL spectra for 13.8 Å ZnS overcoated QDs (a) as a dilute dispersion at room temperature (b) as a QD solid at 77 K with low intensity pulsed excitation, and (c) QD solid, high intensity excitation.

(B) FWHM of the PL as a function of excitation power for the QD solid at 77 K.

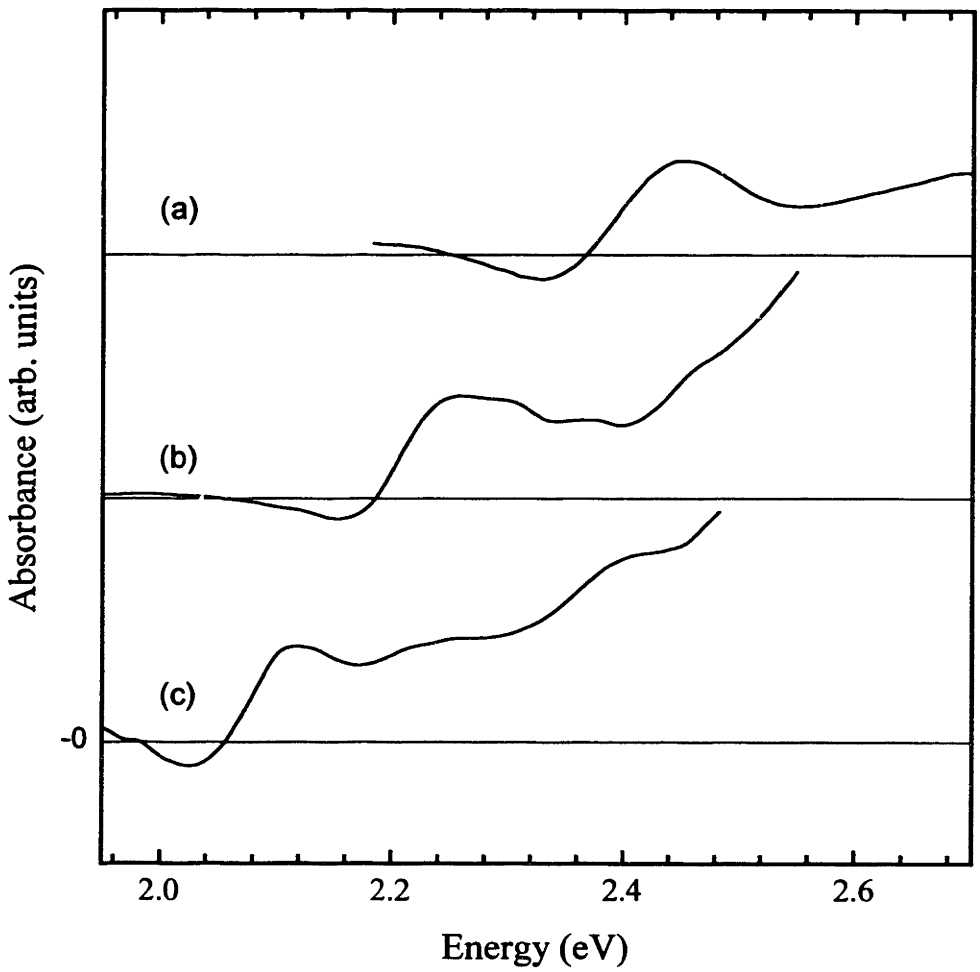

Figure 6.5 Room temperature, transient absorption spectra recorded 1.5 ps after the pump pulse. The narrow bleach observed just below the band edge turns to gain at sufficient pump intensities. The spectra are for (a) 13 Å ZnS overcoated , (b) 17 Å ZnS overcoated , and (c) 21 Å TOPO/TOP capped CdSe QDs.

We observed intensity dependent, spectral narrowing only when exciting near the edge of the sample and only in certain areas of the QD films. These spots did not always correlate with the thickness of the film suggesting that scattering losses from defects in the film and not optical confinement was responsible for the local effect. Thermal cycling of the films increased the pump power required to reach threshold suggesting that the QD film develops cracks which contribute further optical losses. Furthermore, the QD solids are not stable either at 77 K or at 10 K under sustained pulsed excitation of this intensity. After approximately 500 pulses, the narrowed emission peak disappears leaving only the sub-threshold PL line. Sustained excitation for pump powers greater than 2-3 times the threshold power results in optical damage that is visible as a burn on the sample. However, if the pump beam is blocked for as little as 5 seconds in between exposures, the stimulated emission recovers. For a duty cycle of one 100 ms exposure every 5 seconds, and for excitation powers just above the threshold for the spectral narrowing, the PL spectra are completely reproducible.

6.4 Discussion

6.4.1 Is it amplified spontaneous emission?

Spectral narrowing of the photoemission in high gain media can be the result of both cooperative and collective phenomena. Amplified spontaneous emission (ASE) is a collective effect where spontaneous emission from a system of population inverted chromophores is linearly amplified by stimulated emission. Spectral narrowing associated with ASE can be unambiguously identified from a variable strip length experiment;[17] for fixed photon flux, the PL spectrum should gradually narrow as the length of the excited strip is increased and then saturate. More complicated cooperative

effects such as superradiance[18] and superfluorescence[19] are also possible mechanisms for spectral narrowing. Both superradiance and superfluorescence are the result of cooperative spontaneous emission of an inverted system of chromophores due to the overlap of their respective radiation fields. The spectral narrowing in these processes requires a high concentration of excited dipoles within the coherence length for the excited state. However, unless the spot size on the sample is much smaller than the characteristic length to observe ASE, stimulated emission usually overwhelms these cooperative effects. Pending careful variable strip length measurements, we tentatively attribute the intensity dependent spectral narrowing to ASE. Based on the absorption cross-section determined in Chapter 3, the excitation intensity when spectral narrowing is observed corresponds to greater than 2 electron-hole pairs per QD on average.

6.4.2 Energy of the narrowed emission

For dilute dispersions of CdSe QDs, the absorption and emission spectra are inhomogenously broadened by the size distribution and partially overlap (see Figure 6.6). The non-resonant Stokes shift is size, and size distribution dependent and varies from over 100 meV at small sizes to 20 meV for 40 A QDs.[20] The red shift of the emission observed in Fig. 6.2 is qualitatively consistent with the large optical losses due to self-absorption close to the absorption edge. Comparing Figures 6.2A-C, we observe that the ASE mode is more prominent on the red edge of the PL band for larger size QDs.

What is somewhat surprising is the energy of emission below threshold. The peak of the emission occurs at approximately the same energy as the room temperature PL band for a dilute dispersion of the same QDs. For non-overcoated QDs, the absorption spectra and PL generally shift to higher energies by ~ 55 meV on cooling from room

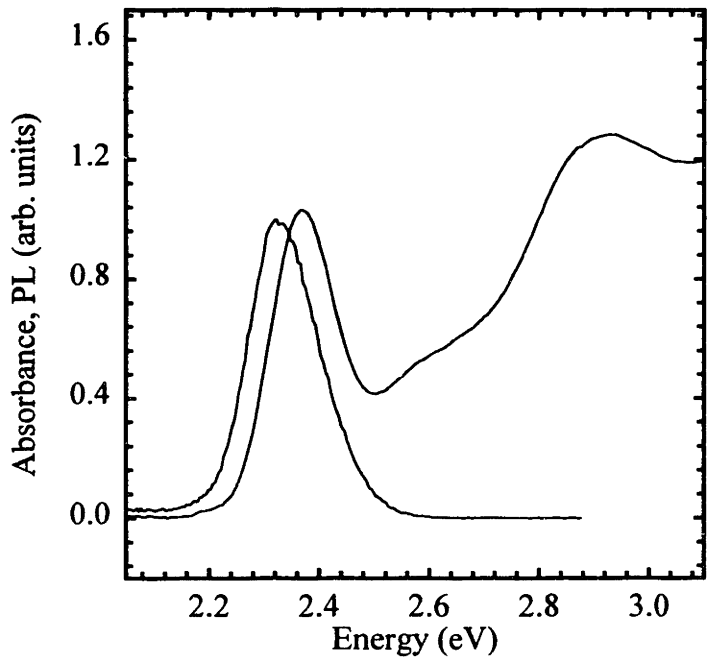

Figure 6.6: Absorption and emission spectra for a dilute dispersion of ZnS overcoated QDs showing the typical luminescence Stokes shift at room temperature.

---

temperature to 77 K. Kagan observed that the entire absorption band within the experimental energy window shifted to higher energies consistent with a lattice contraction and corresponding increase in the band gap.[21] It is reasonable to expect the same behaviour from the core-shell QDs. Re-absorption would enhance the PL of the large QDs in the distribution compared to the small QDs and cause an apparent red shift of the PL. However it should also cause an asymmetric line shape with an enhancement of the lower energy tail. This is qualitative behaviour is observed in Fig 6.2B but not 6.2 A or C.

Interpretation of the emission energy is further complicated by efficient Förster energy transfer in the QD solids. Energy transfer from the smallest QDs of the distribution to the largest QDs increases the Stokes shift, slightly narrows PL band and enhances the low energy tail.[22] This effect is temperature dependent since it depends on

the rate of energy transfer compared to the photoluminescence lifetime of isolated QDs. In principle, ASE should dramatically decrease the lifetime of the excited state thereby reducing the probability of energy transfer and decreasing the Stokes shift of the emission. Finally, it is possible that sample heating plays a role. The thermal conductivity of the QD solid is likely to be quite low and more than 1eV of energy must be dissipated per pump photon as the exciton relaxes to the emitting state.

Clearly careful measurements of the low temperature absorption spectra and spectrally resolved photoluminescence luminescence lifetime of close-packed core-shell QDs are required in order to resolve these issues and understand the position of the gain narrowed emission. Some theoretical calculations have suggested that the stimulated emission associated with a biexciton to exciton transition is possible in strongly confined QDs. [23] The calculated biexciton binding energy is positive and increases with decreasing QD size.[24] As a result, the exciton to biexciton induced absorption (or in reverse, stimulated emission) would appear below the band edge. While experimental evidence to support the biexciton model inconclusive at this time,[12,23] further investigation is warranted.

6.5 Conclusions

We have observed intensity dependent spectral narrowing in QD solids which is qualitatively consistent with amplified spontaneous emission. The narrowed emission moves to lower energies with increasing size of the QDs, consistent with recombination of quantum confined excitons. The volume fraction of semiconductor material (and thus the probability of stimulated emission) in the QD solid ($V_f \sim 0.2$) is much higher than in

solutions or glasses ($V_f \sim 0.001$) possibly explaining why ASE was not observed in these other systems.

In principle, it is now possible to design a device that shows narrow band gain at any energy. CdSe QDs allow one to span the visible region of the electromagnetic spectrum. Other materials such as CdS, CdTe or HgTe allow access to the UV and near infrared as well. All-optical devices such as single pass QD amplifiers for fiber-optic communications or optically-pumped lasers are particularly promising applications. As well, QDs could be easily incorporated into a variety of photonic band gap devices. Recent observations of laser action in optically-pumped conjugated polymers[25,26] and heterostructures with vacuum deposited small organic molecules[27] have raised the possibility of assembling inexpensive laser diodes from these materials.[28] The measurements presented in Chapters 4 suggest that assembling laser diodes from colloidal semiconductor QDs may be difficult. Significant improvements to the electrical contacts are required to make such a device feasible.

6.6 References

[1]V.L. Colvin, M.C. Schlamp, and A.P. Alivisatos, "Light-Emitting-Diodes Made From Cadmium Selenide Nanocrystals and a Semiconducting Polymer," Nature **370**, 354-357 (1994).

[2]B.O. Dabbousi, M.G. Bawendi, O. Onitsuka *et al.*, "Electroluminescence From Cdse Quantum-Dot Polymer Composites," Appl. Phys. Lett. **66**, 1316-1318 (1995).

[3]J. RodriguezViejo, K.F. Jensen, H. Mattoussi *et al.*, "Cathodoluminescence and photoluminescence of highly luminescent CdSe/ZnS quantum dot composites," Appl. Phys. Lett. **70**, 2132-2134 (1997).

[4]N.C. Greenham, X.G. Peng, and A.P. Alivisatos, "Charge separation and transport in conjugated- polymer/semiconductor-nanocrystal composites studied by photoluminescence quenching and photoconductivity," Phys. Rev. B **54**, 17628-17637 (1996).

[5]D.S. Ginger and N.C. Greenham, "Charge injection and transport in films of CdSe nanocrystals," J. Appl. Phys. **87**, 1361 (2000).

[6]Y.A. Vlasov, N. Yao, and D.J. Norris, "Synthesis of photonic crystals for optical wavelengths from semiconductor quantum dots," Advanced Materials **11**, 165-169 (1999).

[7]Y. Arakawa and H. Sakaki, "Multidimensional quantum well laser and temperature dependence of its threshold current," Appl. Phys. Lett. **40**, 939-941 (1982).

[8]M. Asada, Y. Miyamoto, and Y. Suematsu, "Gain and the Threshold of Three-Dimensional Quantum-Box Lasers," IEEE Journal of Quantum Electronics **QE-22**, 1915-1921 (1986).

[9]M.V. Maximov, Y.M. Shernyakov, A.F. Tsatsul'nikov *et al.*, J. Appl. Phys. **83**, 5561 (1998).

[10]N.N. Ledentsov, V.M. Ustinov, A.Y. Egorov *et al.*, Fiz. Tekh. Poluprovodn **28**, 1484 (1994).

[11]S. Fafard, K. Hinzer, S. Raymond *et al.*, "Red-Emitting Semiconductor Quantum Dot Lasers," Science **274**, 1350 (1996).

[12]J. Butty, Y.Z. Hu, N. Peyghambarian *et al.*, "Quasicontinuous gain in sol-gel derived CdS quantum dots," Appl. Phys. Lett. **67**, 2672-2674 (1995).

[13]H. Giessen, J. Butty, U. Woggon *et al.*, "Ultrafast nonlinear gain dynamics in semiconductor nanocrystals," Phase Transitions **68**, 59-94 Part B (1999).

[14]V.I. Klimov, C.J. Schwarz, D.W. McBranch *et al.*, "Ultrafast dynamics of inter-and intra-band transitions in semiconductor nanocrystals: Implications for quantum dot lasers," Phys. Rev. B **60**, R2177-R2180 (1999).

[15]V.I. Klimov, A.A. Mikkhailovsky, S. Xu *et al.*, "Optical gain and stimulated emission in nanocrystal quantum dot solids," submitted (2000).

[16]B.E.A. Saleh and M.C. Teich, *Fundamentals of Photonics* (John Wiley & Sons, New York, 1991).

[17]K.L. Shaklee, R.E. Nahory, and R.F. Leheny, "Optical gain in semiconductors," J. Lumines. **7**, 284-309 (1973).

[18]R.H. Dicke, "Coherence in spontanous radiation processes," Phys. Rev. **93**, 11-110 (1954).

[19]R. Bonifacio and L.A. Lugiato, "Cooperative radiation processes in two-level systems: Superfluorescence," Phys. Rev. A **11**, 1507-1522 (1975).

[20]M. Kuno, J.K. Lee, B.O. Dabbousi *et al.*, "The band edge luminescence of surface modified CdSe nanocrystallites: Probing the luminescing state," J. Chem. Phys. **106**, 9869-9882 (1997).

[21]C.R. Kagan, "The Electronic and Optical Properties of Close Packed Cadmium Selenide Quantum Dot Solids," Ph.D. Thesis, Massachusetts Institute of Technology, 1996.

[22]C.R. Kagan, C.B. Murray, and M.G. Bawendi, "Long-range resonance transfer of electronic excitations in close-packed CdSe quantum-dot solids," Phys. Rev. B **54**, 8633-8643 (1996).

[23]Y.Z. Hu, H. Giessen, N. Peyghambarian *et al.*, "Microscopic theory of optical gain in small semiconductor quantum dots," Phys. Rev. B **53**, 4814-4822 (1996).

[24]K.I. Kang, A.D. Kepner, S.V. Gaponenko *et al.*, "Confinement-enhanced biexciton binding energy in semiconductor quantum dots," Phys. Rev. B **48**, 15449 (1993).

[25]N. Tessler, G.J. Denton, and R.H. Friend, "Lasing from conjugated-polymer microcavities," Nature **382**, 695-697 (1996).

[26]M.D. McGehee, M.A. Diaz-Garcia, F. Hide *et al.*, "Semiconducting polymer distributed feedback lasers," Appl. Phys. Lett. **72**, 1536-1538 (1998).

[27]V.G. Koslov, V. Bulovic, P.E. Burrows *et al.*, "Laser action in organic semiconductor waveguide and double-heterostructure devices," Nature **389**, 362-364 (1997).

[28]J.H. Schon, C. Kloc, A. Dodabalapur *et al.*, "An organic solid state injection laser," Science **289**, 599 (2000).

List of Publications.

K. Shimizu, R. Neuhauser, C. A. Leatherdale, WK. Woo, M. G. Bawendi, "Blinking statistics of single nanocrystal quantum dots". (submitted).

V. I. Klimov, A. A. Mikhailovsky, S. Xu, A. Malko, J. Hollingsworth, C.A. Leatherdale, H.-J. Eisler, M.G. Bawendi, "Optical gain and stimulated emission in quantum dot solids," (in press).

C. A. Leatherdale and M.G. Bawendi, "Observation of solvatochromism in CdSe colloidal quantum dots," (submitted).

C. A. Leatherdale, C.R. Kagan, N.Y. Morgan, S.A. Empedocles, M. A. Kastner, and M.G. Bawendi, "Photoconductivity in CdSe quantum dot solids," Phys. Rev. B: **62** (4) 2669 (2000).

V. I. Klimov, A. A. Mikhailovsky, D.W. McBranch, C.A. Leatherdale, and M.G. Bawendi, "Quantization of Multiparticle Auger Rates in Semiconductor Quantum Dots," Science **287** (February 11), 1011-1013, (2000).

V. I. Klimov, A. A. Mikhailovsky, D.W. McBranch, C.A. Leatherdale, and M.G. Bawendi, "Mechanisms for intraband energy relaxation in semiconductor quantum dots: the role of electron-hole interactions," Phys. Rev. B **61**, R13349-R13352 (2000).

V.I. Klimov, D.W. McBranch, C.A. Leatherdale, and M. G. Bawendi. "Electron and hole relaxation pathways in semiconductor quantum dots," Phys. Rev. B **60**, 13740-13749 (1999).

V. I. Klimov, Ch. J. Schwarz, D.W. McBranch, C.A. Leatherdale, and M.G. Bawendi, "Ultrafast dynamics of inter-and intraband transitions in semiconductor nanocrystals: implications for quantum dot lasers," Phys. Rev. B **60**, R2177-R2180 (1999).

C. A. Leatherdale, N.Y. Morgan, C.R. Kagan, S.A. Empedocles, M.G. Bawendi, and M.A. Kastner, "Charge generation and transport in CdSe Semiconductor Quantum Dot Solids, " Proceedings of the Materials Research Society, San Francisco, 1999.

V. I. Klimov, Ch. Schwarz, X. Yang, D.W. McBranch, C. A. Leatherdale, and M.G. Bawendi, "Electron and hole relaxation pathways in II-VI semiconductor nanocrystals," Proceedings of the Materials Research Society, Boston, 1998.

Acknowledgement

The road to this thesis began more than 10 years ago in a high school classroom in British Columbia. There a wonderful physics teacher by the name of Mr. MacAulay was tossing a ball straight in the air and pointing out that it stopped momentarily (wonder of wonders!) before it came down again. My fascination with physics was born. Five years and many more teachers later, something lead me to attend a UBC chemistry department seminar given Dr. Louis Brus. His descriptions of a real "live" particle-in-the-box caught my imagination leading me straight to Prof. Moungi Bawendi and physical chemistry at MIT.

Always encouraging, Moungi has been a wonderful advisor and role model in many things, not the least of which is how to negotiate the world of "hot" science with dignity, humility, scientific rigor, and a never-ending vision of what could be possible.

I have been especially fortunate to have some excellent collaborators here at MIT and abroad. Cherie Kagan taught me the ways of the QD solid and then made helpful comments on the nearly endless revisions of the photoconductivity paper. Nicole Morgan, my co-conspirator in low level measurements on QD solids, traded me chips for samples and helped find ground loops and unexpected noise sources many times. Marc Kastner's enthusiasm and advice as well as his excellent editing skills on the photoconductivity work were greatly appreciated. Sasha Efros (Naval Research Laboratory) encouraged me in my quest for a quantitative description of the photoconductivity and also provided useful insights on the absorption cross-section problem. A group meeting literature talk on ultrafast pump-probe measurements several years ago turned into a fruitful collaboration with Victor Klimov and his group at Los Alamos National Laboratory. The last chapter of this thesis is the serendipitous result of having the right samples with the right people at the right time.

To my friends and colleagues over the years in the Bawendi group: Cherie, Ken K., Fred, Steve, Dima, Wing, Vik, Ken. S., Nathan, Sungjee, Robert, Hans, and Andrew: it has been a pleasure playing both in the laboratory sandbox and in the sand volleyball court with you. I have learned much about science and life from all of you. Mirna and Inhee, you are just beginning but I can see already that you will do great things. I pass to you the torch of keeping all these guys honest.

I think I've worked in nearly every CMSE laboratory over the years and I'm grateful to all the technical staff who keep these facilities running. Libby Shaw and Tim McClure, thanks for your patience as I boldly went with solvents where no one had gone before. Gale Petrich and the microfabrication laboratory made the lithography possible. Ramachandra Dasari, Gene Hanlon, and Matt Jacobson, gave much help and encouragement during a long eight months in the Harrison Spec. Lab while I made photoluminescence lifetime measurements. Special thanks as well to Scott Miller and Scott Carpenter who lent us a beam from their amplified Ti-sapphire laser for the ASE experiments.

For some reason, tall Germans seem to think it is possible to survive only on science and air. I need seem to need a bit more and I'm grateful for the wonderful MIT choral program that did much to keep me sane over the years. My good friends in the department and out, Eliot, Peter, Grace, Kim, and Stacey: thank you for being my fan club both in science and in music. Finally, this acknowledgement would be incomplete without mentioning the inhabitants of 57 Roseland Street—the best roommates a person could ask for. Edith and Bill, you have suffered through the ups and downs of this Ph.D. with me and lent a sympathetic ear many a night. Thanks to you I know that if science doesn't work out, there's always catering, publishing, presidential campaign planning...

And to my family: thank you for believing in me and always supporting me in whatever endeavour I get into my head.

THESIS PROCESSING SLIP

FIXED FIELD: ill _____ name _____

index _____ biblio _____

► COPIES: (Archives) Aero Dewey Eng Hum

Lindgren Music Rotch (Science)

TITLE VARIES: ► ☐ _____

_____

_____

NAME VARIES: ► ☑ Catherine Anne

Leatherdale

IMPRINT: (COPYRIGHT) _____

_____

► COLLATION: _____

_____

► ADD: DEGREE: _____ ► DEPT.: _____

SUPERVISORS: _____

_____

_____ _____

_____ _____

_____ _____

_____ _____

_____ _____

_____ _____

_____ _____

NOTES:

cat'r date

page

► DEPT: Hist. ▶ 355

► YEAR: _____ ► DEGREE: _____

► NAME: _____

_____